fortune Journals

Research Article

JOURNAL OF ANALYTICAL TECHNIQUES AND RESEARCH

ISSN: 2687-8038

Quantitative *In Silico* Analytical Chemistry for Drug Discovery: From Ion-Ion Interaction to Covid-19 Variants Transmissibility and the Binding Inhibitors

Toshihiko Hanai

Abstract

Since a new coronavirus (Covid-19) was found in December 2019, more than 40 variants have been identified and spread around the world and causing pandemonium. The urgent requirement for new vaccines and drugs has been demanded. Various drug candidates have been screened using computational chemistry methods. The main-flame computer can handle the auto-docking of proteins with various compounds from the data bank; however, we have to consider that amine and carboxy groups should be ionized and the phenolic hydroxy group may be in molecular form. The properties of bio-mimic ion-exchange groups are quantitatively described using simple model ion exchangers docking with analytes whose properties are easily characterized from their structure. Furthermore, the solvent and ion contributions to molecular interaction between the ion-exchange group and an analyte were quantitatively analyzed.

The fundamental *in silico* analysis of molecular interactions between small molecules was expanded to analyze protein and substrate interactions, quantitative analysis of selective enzyme reaction, such as alanine racemase, serine racemase, alcohol dehydrogenase, cinnamyl alcohol dehydrogenase, *D*-amino acid oxidase, and *D*-aspartic acid oxidase. Proteins soften their stereo structures, collect various substrates, and tighten the complex structure to metabolize the substrates. Or the substrates tighten the complex structure and freeze the enzyme activity. The ion-ion interaction site is the major substitute recognition center and the enzyme selectivity is related to the electron localization degree. Further study for protein-protein interactions is applied to analyzing Covid-19 transmissibility as the molecular interaction energy value differences. Indeed, the most contributed interaction was ion-ion interaction, and the strength was quantitatively obtained as electrostatic energy value difference. The strongest interaction energy value was obtained between Omicron BA2 S-RBD and ACE-2. In addition, The ideal binding inhibitors of S-RBD with ACE-2 were acidic compounds that should be adsorbed at the S-RBD contact site with ACE-2 but not inhibit ACE-2 activity. The most effective binding inhibitors were ionized-carboxy compounds including natural compounds.

Analytical chemistry means the analysis of chemistry. It is not limited only to measurements of amounts and involves analyses of chemical phenomena based on the chemical structures and properties like organic and biochemistry. The basic interaction mechanisms are supposed to be simple, and the selectivity is qualitatively explained as "like dissolves likes". The developed fundamental technical method is described in part in this tutorial review for targeting to understand the Covid-19 mutant's transmissibility and designing the binding inhibitors based on ion-ion interaction.

Affiliation:
Health Research Foundation, Research Institute for Production Development 4F, 15 Simogamomorimotocho, Sakyoku, Kyoto 606-0805 Japan

***Corresponding author:**
Toshihiko Hanai, Health Research Foundation, Research Institute for Production Development 4F, 15 Simogamomorimotocho, Sakyoku, Kyoto 606-0805 Japan.

Citation: Toshihiko Hanai. Quantitative In Silico Analytical Chemistry for Drug Discovery: From Ion-Ion Interaction to Covid-19 Variants Transmissibility and the Binding Inhibitors. Journal of Analytical Techniques and Research. 8 (2026): 38-109.

Received: April 27, 2026
Accepted: May 04, 2026
Published: May 27, 2026

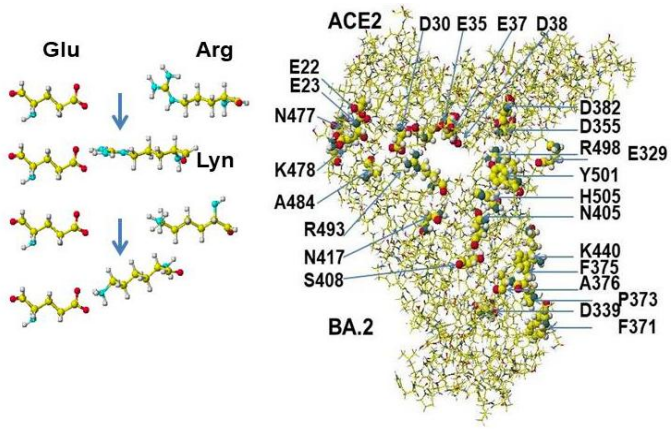

The ion-ion interaction is the strongest molecular interaction force of proteins. The simplest example was first exhibited between small molecules; then, the fundamental approach is applied for quantitative analysis of 17 enzyme selectivity. Practically, the binding strength of COVID-19 mutants with ACE-2 is analyzed as protein-protein binding strength. Increasing number of basic amino acids at the binding site of S-RBD tightened the binding strength with ACE-2. Pre-binding of acidic compounds including natural compounds on S-RBD inhibit the binding with ACE-2. Modification and additives to known drugs effectively inhibited the binding.

Keywords: Quantitative *in silico* analysis, Ion-exchange mechanism, Amino acids, Enzyme reaction, COVID-19 transmissibility

Introduction

Analytical chemistry has used various techniques without a quantitative explanation of the chemistry. Historically, the chemistry of analytical methods was described using different analytical methods. Calorimetric analysis indicated that the hydrogen bonding strength of alkyl alcohols depends on the alkyl chain length, and up to four methylene units can affect the hydrogen bonding strength. This result supported that butylalcohol is a suitable solvent for extracting relatively hydrophobic molecules from water. Color indicators have been the backbone of simple pH tests and titration analyses. The spectrophotometric determination of hydrogen ion concentrations using color indicators was demonstrated [1], and Kolthoff described the dissociation processes in detail [2]. The experimentally measured dissociation of phenolphthalein is described using four dissociation structures, where the ionization of two phenolic hydroxyl groups converts the neutral molecular form into the red quinoid form. Further dissociation from the quinoid structure to the alcoholic form eliminates the color. The dissociation mechanisms can also be described using three structures without a transition structure [3]. Furthermore, the mechanisms were quantitatively described *in silico* analysis using the chemical structures and the related predicted spectra [4].

NMR spectra of the organic polymer gels were measured in various solvents. The water content of outside and inside of resins was related to the ion-exchange capacity in which water molecules contact the ion-exchange groups [5, 6]. Furthermore, a fundamental study of molecular interactions in chromatography was performed using simple small molecules to analyze the chromatographic behavior of aromatic compounds on an anion-exchange resin with a non-aqueous eluent. The NMR spectra of a mimic anion-exchanger (trimethyl-ammonium ion exchange-resin) with aniline or nitrobenzene in a deuterium solvent (ethanol-OD) were measured to investigate chromatographic molecular interaction. The probable signal of a tri-methyl group of trimethyl benzyl-ammonium shifted toward a high field with aniline and a low field with nitrobenzene. The chemical shift by adding aniline was larger than that of nitrobenzene, which was not observed with the addition of toluene. The chemical shift is related to electronegativity. The amino group of aniline faced the chloride ion of trimethyl benzyl-ammonium. The chloride ion repulsed the nitro-group of nitrobenzene. Because nitro-group and chloride ions are electron-rich groups or atoms, these small molecules move freely in solution. Therefore, the contact conformation in the solution may not reflect the chromatographic interactions spectra measured using ion-exchange resins were broad because the instrument was not used for solid-state NMR. However, the spectra supported chromatographic behavior [7].

Citation: Toshihiko Hanai. Quantitative In Silico Analytical Chemistry for Drug Discovery: From Ion-Ion Interaction to Covid-19 Variants Transmissibility and the Binding Inhibitors. Journal of Analytical Techniques and Research. 8 (2026): 38-109.

Furthermore, electron spectroscopy for chemical analysis (ESCA) was used for measuring chemical shifts due to electron localization. The chemical signal of ^{12}CP shifted 0.27 eV by the adsorption of α-hydroxynaphthalene on the anion-exchanger (CR400 Cl form), and that of ^{12}CP shifted -0.26 eV by the adsorption of 1,8-dinitronaphthalene on the anion-exchanger. The N1S chemical signal of the anion exchanger was -0.08 eV and -0.43 eV for α-hydroxynaphthalene and 1.8-dinitronaphthalene, respectively. NMR and ESCA results indicated that the chemical shifts are caused by the interaction between the ion exchangers and the analytes. Although the shifts indicated a positive answer to the strength of molecular interactions, the spectrometric resolution was insufficient at that time [8].

These instrumental analysis results were later quantitatively described using computational chemical (*in silico)* analysis. On the other hand, The electron-donor-accepter intermolecular interaction is important in chemistry. In primary acts and transient states of numerous chemical reactions, it is the basis of many catalytic processes, determines the specific solvation in solutions, and finally leads to the formation of numerous compounds with different properties [9]. The electron-donor-accepter approach to molecular interactions provides rationalization and a unified re-interpretation of well-known phenomena in biochemistry [10]. These conclusions provide analyzing protein activities quantitatively using *in silico* analysis.

Numerous reports using ion exchangers have been published, but molecular interactions of ion-exchange mechanisms and chemistry have not been quantitatively described [11 - 13]. A quantitative explanation of these molecular interaction mechanisms was studied *in silico* model phases, proposing a cation-exchanger for basic drugs in 2004 and an anion-exchanger for acidic drugs in 2007 [14]. The hexylamino group is a cation in a solution containing using buffer components that hold molecular form acidic compounds by hydrogen bonding and ionized acidic compounds by ion-ion interactions. On the other hand, the pentylcarboxy group holds acidic compounds by hydrogen bonding and basic compounds by ion-ion interaction in acidic solutions. The ionized carboxy group holds basic ionized compounds by ion-ion interaction and folds basic molecular compounds by hydrogen bonding in neutral and basic solutions. However, the determination of chemical structures of various compounds in an eluent depends on their dissociation constant p*K*a; therefore, the difficulty of modeling their structures confuses the quantitative explanation of molecular interaction mechanisms in ion-exchange liquid chromatography.

The relative molecular interaction difference is based on the solubility factors [15], and the mechanisms were quantitatively explained using model compounds *in silico* analysis. The molecular interaction mechanisms are a combination of van der Waals (VW) force, electrostatic (ES) interaction, and hydrogen bonding (HB). Different types of chromatography demonstrate typical molecular interaction (MI) forces. If the solubility factors can be quantitatively reconstructed, the chromatographic molecular interaction mechanisms can be analyzed quantitatively. Chromatography is a tool to study molecular interaction strength quantitatively from the reproducible elution times.

Computational chemical analysis using molecular mechanics (MM) software provides the MI energy values (kcal・mol^{-1}) as the sum of mainly VW, HB, and ES energy values. The VW energy is related to molecular size. Therefore, the contact surface area between the analyte and adsorbent contributes to the MI energy. VW force is predominant in reversed-phase liquid chromatography. When HB exists between the analyte and adsorbent, HB energy also contributes to the MI energy. HB is the primary molecular interaction in normal-phase liquid chromatography and partially in hydrophilic interaction liquid chromatography (aqueous normal-phase liquid chromatography). ES includes dipole-dipole interaction, π–π interaction, contact charge transfer, charge transfer, ion-dipole, and ion-ion interactions. These interactions are used to explain the organic reactions based on electron localization. Therefore, the degree of these interactions can also be explained using electrostatic energy values. These MI energy values are the sum of the solute and model phase energy values minus a complex energy value, calculated as per the following equations.

MIFS, MIHB, MIES, and MIVW are the MI energies of the FS, HB, ES, and VW energy values, respectively. The FS is the final (optimized) structure.

MIFS = FS (molecule A) + FS (molecule B) – FS (molecule A and molecule B complex),
MIHB = HB (molecule A) + HB (molecule B) – HB (molecule A and molecule B complex),
MIES = ES (molecule A) + ES (molecule B) – ES (molecule A and molecule B complex),
and

MIVW = VW (molecule A) + VW (molecule B) – VW (molecule A and molecule B complex).

A quantitative explanation of the molecular interaction mechanisms of the alkyl-bonded phases is relatively simple. However, the molecular interaction mechanisms in non-aqueous systems and non-ionic phases are complex because both HB and ES must be considered. The inductive effect of ligands and analytes affects the quantitative explanation. Furthermore, the quantitative analysis of molecular interaction mechanisms in ion-exchange liquid chromatography is complicated, and modeling the ion-exchange phase is difficult because of the repulsion between ion-exchange groups. The fundamental phenomena were quantitatively analyzed using simple molecules [14], and a practical model is under development.

Furthermore, the guanidino group is an ion-exchange group of proteins, and protamine-coated silica gel was first used for liquid chromatography of saccharides. Thus, a guanidino-bonded phase developed from a propylamine-bonded phase for the separation and quantitative recovery of saccharides comparable to that observed with a propyl-amine bonded phase was achieved [16]. The poor recovery is because primary amines react with saccharides *in vitro* and produce glycosides. The propylamine-bonded silica gel is unstable in a buffer solution; therefore, a hexylamine-bonded silica gel with a secondary silyl reaction was synthesized and used for saccharide chromatography [17].

The MI in chromatography was analyzed using single-bonded silicon oxides with model ligands such as octyl-, hexenyl-, hexylamine-, and hexylguanidine-bonded trimethoxy-silicones. The HB, ES energy, and VW energy values calculated for MI energy indicate their specific molecular interactions with the analytes [18]. This approach was applied to study the MI mechanisms of ion-exchange liquid chromatography of acidic drugs using hexylamine and hexylguanidine-bonded silica gels [19]. The developed method for quantitative *in silico* analysis of molecular interaction using the reproducible chromatographic data was applied for quantitative analysis of various enzyme reactivity. The main interaction site was the ion-ion interaction between a residual amino acid and a counter-ionic group of the analyte. Furthermore, The quantitative analytical method was applied to protein-protein interactions, especially for COVID-19 variants' transmissibility, and designing the binding inhibitors of S-RBD with ACE-2 as an application of quantitative ion-ion interaction analysis.

The process; the properties of ion-exchange groups are described from the fundamental activity (Fundamental properties of ion-exchange groups), protein-substrate interaction (Protein-substrate interactions from enzyme reactivity), and the practical application (Protein-protein interactions from SARS COVID-19 variants transmissibility and the binding inhibitors).

1. Fundamental Properties of Ion-Exchange Groups

Analytical chemistry means the analysis of chemistry. It is not limited only to measurements of amounts and involves analyses of chemical phenomena based on atoms and their behaviors. [20, 21] One of the interesting subjects is the processes of human evolution. How enzymes have evolved to their present molecules is very mysterious. We wonder if the evolution processes are completed or still continue for their suitable molecules. A part of such questions can be analyzed from enzyme selectivity. Human enzymes are less flexible than animals at present. In the past, giant dinosaurs could not adapt to climate change, but small ones adapted and lived like birds. Comparing final product enzymes of a variety of species may give us basic information about the environmental adaptability of creatures.

Direct study of enzyme affinity requires a comprehensive knowledge of evolution and biochemistry; however, the basic enzyme-substitute interaction mechanisms are supposed to be simple, like solubility. Solutes dissolve in solvents. The selectivity is qualitatively explained as "like dissolves like". Therefore, quantitative analysis of simple molecular interactions must be understood before analyzing enzyme selectivity.

On the other hand, developing a computer improves data processing and controlling analytical instruments in analytical science [22]. The quantitative study of chemistry was described by mathematical calculations using reference properties. [23]. However, the development of computational chemistry has not been well used to study analytical chemistry, even though analytical science is based on chemistry, physics, electronics, biology, and technology. We need molecular properties quantitatively to understand chemistry.

"Like dissolves like" is the fundamental explanation for solubility. "Like dissolves like" can be precisely explained using fundamental molecular properties. Polar compounds solve in water, and fatty (non-polar) compounds solve in hexane (non-polar solvent). However, the details are not explained in general chemistry. The typical properties can be measured using chromatography; therefore, a variety of chromatographic names were proposed, such as reversed-phase (hydrophobic), ion-exchange (including ion), charge-transfer (including contact charge transfer), normal-phase (including hydrophilic), and salting-out chromatographies. Size exclusion (including gel-permeation and molecular sieving) chromatography is directly not related to solubility. Affinity (including enantiomer) chromatography is a combination of solubility properties and steric hindrance. The typical solubility properties are van der Waals forces, hydrogen bonding, and electrostatic force [24].

Proteins collect various compounds and distribute and metabolite them. Acidic and basic amino acids contribute to the important play in the process. Ion-exchange groups work extensively in biological organisms; however, the quantitative explanation of their contribution is not simple. For example, acidic compounds are molecular forms in acidic conditions and ionized forms in basic conditions. In acidic conditions, the actual interaction mechanisms should be similar to Lewis acid-base interactions, and hydrogen bonding may be predominant. Electron localization produces Lewis-acid and base structures even when the analytes are neutral molecules. The molecular form in physiological conditions depends on the chemical structures. Even all acidic drugs are not ionized. The fundamental activity of ion-exchange groups is quantitatively described using simple molecules.

4

1.1. Fundamental molecular interactions

Hydrogen Bonding

The hydrogen bonding of alkyl alcohols depends on the alkyl chain length, and up to four methylene units can affect the hydrogen bonding. Alkyl alcohols from methanol to nonylalcohol have been constructed, and individual and identical pair energy values were calculated after optimizing the structures using MM2 calculations. The calculated values are summarized in Table 1, and examples of complexes are shown in Figures 1 and 2.

Table 1. Complex conformation and MI energy change

	Monomer			Dimer			Molecular interaction		
Compound	hb	es	vw	HB	ES	VW	MIHB	MIES	MIVW
Methylalcohol	0.000	0.000	-0.077	-2.898	-1.216	0.138	2.898	1.216	-0.292
Ethylalcohol	0.000	0.000	0.583	-1.660	-1.268	-0.012	1.660	1.268	1.178
Propylalcohol	0.000	0.000	1.085	-0.102	-0.069	-0.400	0.102	0.069	2.570
Butylalcohol	0.000	0.000	1.565	-0.080	-0.051	-0.439	0.080	0.051	3.569
Pentylalcohol	0.000	0.000	2.034	-0.076	-0.065	-0.479	0.076	0.065	4.547
Hexylalcohol	0.000	0.000	2.580	-0.079	-0.055	-0.565	0.079	0.055	5.725
Heptylalcohol	0.000	0.000	2.961	-0.082	-0.063	-0.632	0.082	0.063	6.554
Octylalcohol	0.000	0.000	3.421	-0.079	-0.057	-0.720	0.079	0.057	7.562

Unit: kcal·mol^{-1}

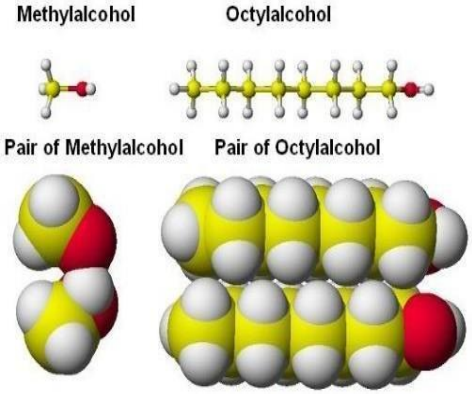

Figure 1. Interaction of a pair of methylalcohol and the octylalcohol. Black, gray, and white balls: oxygen, carbon, and hydrogen.

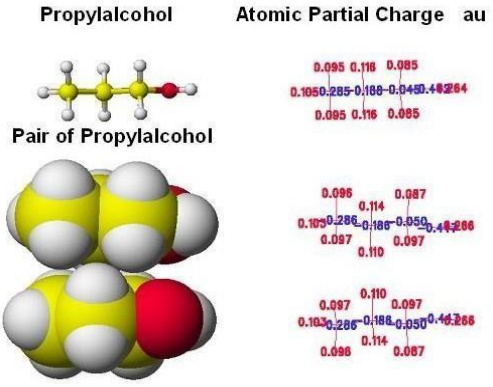

Figure 2. interaction of a pair of propylalcohol and atomic partial charge, Black, gray, and white balls: oxygen, carbon, and hydrogen, apc unit: au

These calculated values depend on the program version [25], but the physical properties are the same. The complex conformation of two propylalcohol provided MIVW 2.570 and MIHB 0.102 kcal·mol^{-1}. Apc of hydroxy-oxygen was reduced from -0.442 to -0.447 au, and the apc of hydrogen increased from 0.264 to 0.266 au. The contact-charge-transfer complex formation changed a little hydrogen bonding capability. This model analysis is essential to explain hydrogen bonding.

The molecular interaction energy values are plotted against the carbon number of the alkyl alcohol chain, along with the results for alkanes. The energy values of a pair of identical alcohols were smaller than twice the energy of one alcohol. This result indicates that the energy values calculated using the MM2 program can explain the degree of molecular interaction. Increasing the alkyl-chain length decreased hydrogen bonding energy values along with electrostatic energy values by butylalcohol. Their van der Waals energy values indicated their complex formation. Their MIVW energy values increased dramatically with increasing alkyl chain length; then, the value leveled off to a constant. There was a linear increase in the hydrogen bonding energy values up to three carbons. This means hydrogen bonding contributes to molecular interactions for alcohols up to and including three carbon atoms, and van der Waals energy is the main energy for alkyl alcohols with longer chains. However, the corrected energies did not bear a linear relationship to their calculated hydrogen-bonding energies given in Table 1.

Coulombic Forces (Ion–Ion Interactions)

The possibility of computational chemical analysis of molecular interactions can be understood from the analysis of simple model compounds. Ion–ion interactions were studied for the combination of an ammonium ion (cation) with an acetate ion (anion) by MM2 calculations. The calculated ion-pair formation energy values are as follows. The balance (the MI energy value) after complex (ion-pair) formation indicates the energy contribution of the ion-pair formation. The electrostatic energy mainly contributes to the ion-pair formation between ammonium and acetate ions. The ammonium ion, acetate ion, and the ion-pair structures are shown in Figure 3, where the atomic distance of the ammonium hydrogens has been expanded from 1.0 to 1.3 Å. Their apc calculated using the MOPAC PM5 program is also indicated, where the apc of the ammonium hydrogens has been doubled.

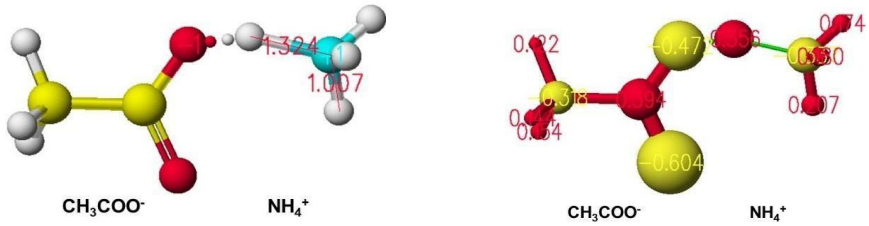

Figure 3. Ion-ion interaction between acetate and ammonium ions, unit: bond length A, partial atomic charge au

In proteins, the aspartic and glutamic acid carboxy groups work as a cation-exchange group, the lysine ε-amino group works as a hydrogen-bonding group and an anion-exchanger, and the arginine guanidino group works as an anion-exchanger. Their activity depends on their dissociation, and the dissociation constants of aspartic and glutamic acid carboxy groups are 3.65 and 4.25. The lysine ε-amino and arginine guanidino groups are 10.53 and 12.48, respectively. In general, these amino acids are ionized in physiological conditions. However, the fundamental activity of the carboxy, amino, and guanidino groups was analyzed using simple model compounds with solvent (water) and ion (sodium and chlorine) effects for their molecular interactions with simple model compounds to study ion-ion interaction, hydrogen bonding, and van der Waals interaction.

1.2 Study the fundamental interaction mechanisms of ion-exchange groups

The fundamental activities of carboxy-, amino-, and guanidino groups of various compounds like drugs are easily described using simple model compounds to understand their interaction mechanisms. These groups were attached with hexyl-group, and analytes are toluene, benzene, phenol, benzoic acid, aniline, and their ionized forms. In the following Figures 4 & 5, gray (yellow), black (red), dark gray (blue), and small white balls are carbon, oxygen, nitrogen, and hydrogen atoms. Green (light gray) is chlorine, and large white is sodium atoms. The calculated molecular properties are given in Table 2.

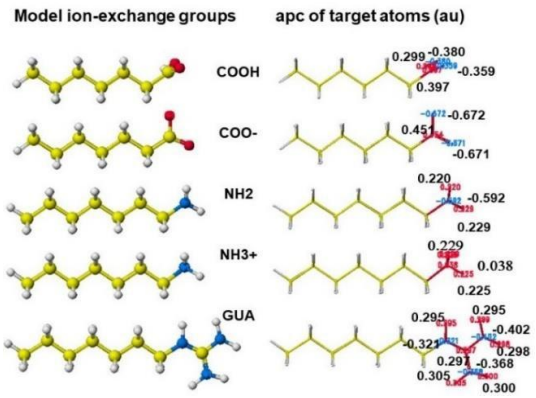

Figure 4. Properties of model phase ligands with atomic partial charge

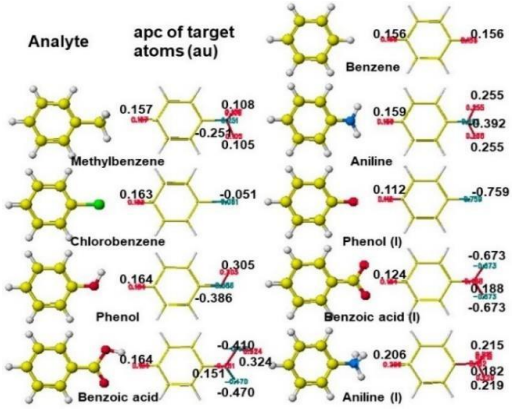

Figure 5. Properties of model analytes with atomic partial charge

Table 2. Molecular properties of hexyl-carboxyl, heptyl-amino, guanidine compounds, and analytes

Molecule	HB	ES	VW
Model phase			
Heptanoic acid (M)	-0.606	-4.332	3.864
Heptanoic acid (I)	0.000	0.000	2.952
Heptylamine (M)	0.000	0.000	2.785
Heptylamine (I)	0.000	0.000	3.162
Heptylguanidine	0.000	-21.981	4.994
Model analyte			
Benzene	0.000	0.000	3.005
Methylbenzene	0.000	0.000	3.035
Chlorobenzene	0.000	0.000	3.214
Phenol	-1.462	0.000	2.957
Benzoic acid	-3.458	-6.671	4.875
Aniline	-1.334	0.000	3.416
Phenol (I)	0.000	0.000	2.986
Benzoic acid (I)	0.000	0.000	4.743
Aniline (I)	0.000	0.000	3.496

Unit: kcal mol^{-1}

A carboxy group consists of hydroxy and carboxyl groups, demonstrating hydrogen bonding and electrostatic energy values. However, the carboxy group is ionized in physiological conditions. An amino group did not show hydrogen bonding energy value due to no bonding. A guanidino group has weak hydrogen bonding, but electrostatic energy was predominant. In the initial position, benzene was located about 3.07Å apart from the carboxy group and optimized the structure. Benzene contacted the carboxy group and formed a contact charge transfer complex, and the atomic partial change indicated the contact site.

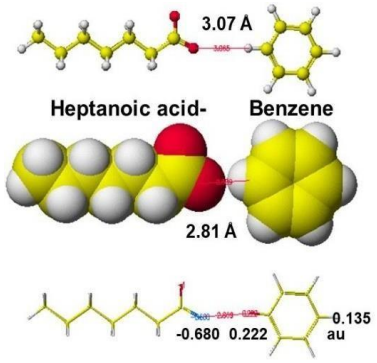

Figure 6. Molecular interaction between ionized heptanoic acid and benzene

The electron localization was studied by the addition of methyl and chlorine groups. The methyl +I effect can be analyzed by docking the carboxy group and either phenyl or methyl groups of methylbenzene. At the initial position, the methyl group faced toward the carboxy group, then optimized the conformation. The complex structures are shown in Figures 7a and b. In Figure 7a, these compounds contacted weak van der Waals force (2.131 kcal.mol^{-1}). In Figure 7b, the interaction energy values were high, and these molecules were contacted with hydrogen bonding (MIHB 6.811 kcal.mol^{-1}). Carboxy oxygen apc was changed from -0.671 to-0.679 and -0.680 au, respectively, and the phenyl *p*-hydrogen apc was changed from 0.157 to 0.220 au (Figure 7a). The methyl carbon apc was changed from -0.251 to -0.261 au (Figure 7b) due to their electron localization by their contact. Figure 7b should be the possible conformation even if the MI energy value was small.

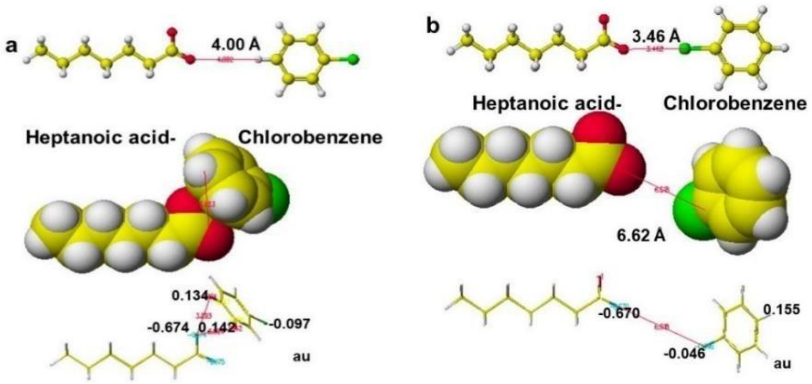

Figures 7a and b. Docking of ionized heptanoic acid with methylbenzene and apc

Chlorobenzene having -I effect of chlorine was also docked via hydrogen bonding between the carboxy group and the phenyl group via hydrogen bonding (MIHB 6.955 kcal.mol^{-1}). The apc values of carboxy oxygen were not changed significantly (-0.674 and -0.670 au) (Figure 8a), but chlorine apc values were clearly changed from -0.051 to -0.097 (Figure 9) and -0.046 au (Figure 10). These differences indicate their contact or repulsion. In Figure 8b, these two molecules were contacted, and the phenyl *p*-hydrogen apc value was changed from 0.163 to 0.134 au (Figure 8a). The primary interaction was van der force (MIVW 1.660), higher than MIES 1.137 kcal·mol^{-1} value. The repulsion expanded their atomic distance to 6.62A, and the apc values of key atoms were not changed significantly (Figure 8b). The actual conformation should be in Figure 8a.

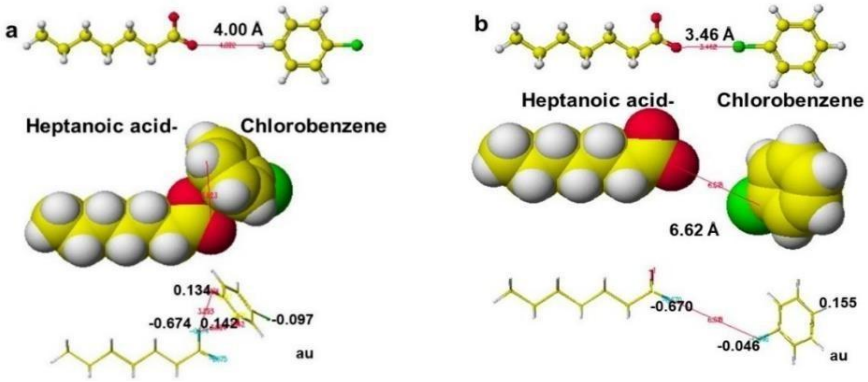

Figures 8a and b. Docking of ionized heptanoic acid with chlorobenzene and the atomic partial charge

In the case of phenol, the phenolic hydroxy group is tightly docked with the carboxy group via electrostatic interaction (MIES 2.217 kcal.mol^{-1}). However, hydrogen and oxygen apc values were changed like in the case of benzene, and hydrogen and oxygen apc were from 0.305 and -0.386 to 0.376 and -0.120 au, respectively (Figure 9b). The phenyl group docked with the carboxy group, but the oxygen apc value did not change significantly, but phenyl *p*-hydrogen apc was changed from 0.163 to 0.228 kcal.mol^{-1} indicated their contact (Figure 9a). Figure 9b should be the actual conformation.

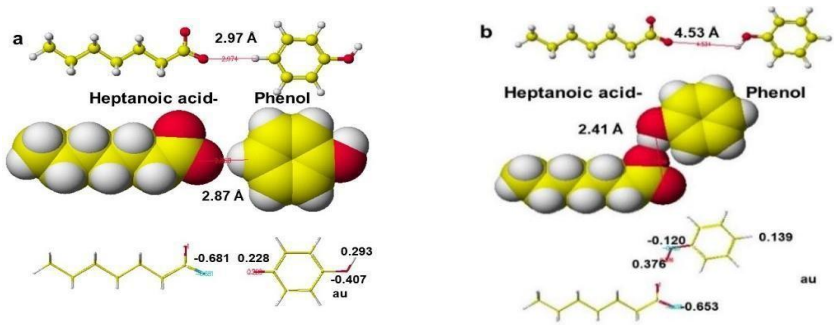

Figures 9a and b. Docking of ionized heptanoic acid with phenol and the apc values

Benzoic acid demonstrated similar behavior to phenol. The benzoic acid located 3.54Å from the heptanoic acid carboxyl group formed a tight complex via MIES (2.150 kcal·mol^{-1}). Even the phenyl group faced the carboxy group (Figure 10a); they formed a complex via MIVW, and the smooth complex formation between carboxy groups did not demonstrate clear apc change, but the conformation of Figure 10b demonstrated clear apc value changes. The apc values of hydrogen and oxygen in Figure 10a were 0.228 from 0.164 and -0.687 from -0.671, respectively. That in Figure 10b were 0.374 and -0.363 au, respectively. Figure 10b should be the actual conformation.

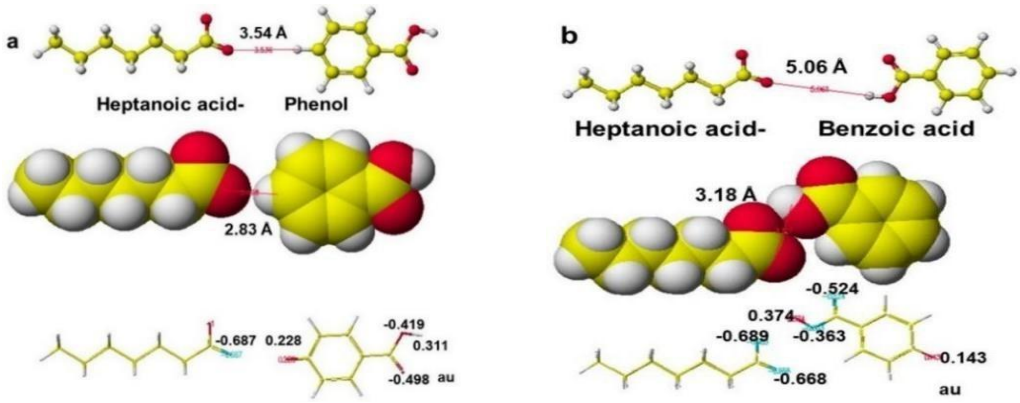

Figures 10a and b. Docking of ionized heptanoic acid with benzoic acid and the apc values

In the case of aniline, acid-base interaction was expected, and amino and carboxy groups interaction was observed via electrostatic interaction (MIES 0.424 kcal·mol^{-1}). However, the MIVW value was 0.807 kcal·mol^{-1}. The hydrophobic interaction was stronger than the electrostatic interaction. The apc values of hydrogen and oxygen in Figure 11a and Figure 11b were 0.226 and -0.677 and 0.317 from 0.220 and -0.691 from -0.672 au, respectively. The molecular form amine should not contact tightly with ionized carboxy groups.

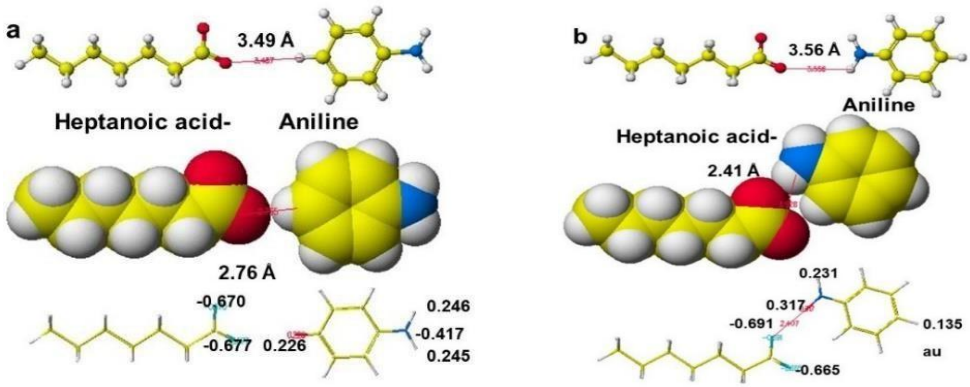

Figures 11a and b. Docking of ionized heptanoic acid with aniline and the apc values

The molecular interactions between heptanoic acid and ionized phenol are shown in Figures 12a and b. Especially, benzoic acid was bound with the carboxy group *via* hydrogen bonding, and the apc values of carboxy oxygen changed from 0.112 to 0.176 au. The apc values the carbonyl oxygen did from -0.671 to -0.646 au (Figure 12a). The initial atomic distance expanded from 2.68 to 2.81Å; the MIES was negative (-1.310 kcal·mol^{-1}). The ionized phenol was repulsed from the carboxy group, and this phenomenon should occur in a very high pH location. These same negative ions repulsed each other and expanded their molecular distance to 13.04 Å in Figure 12b.

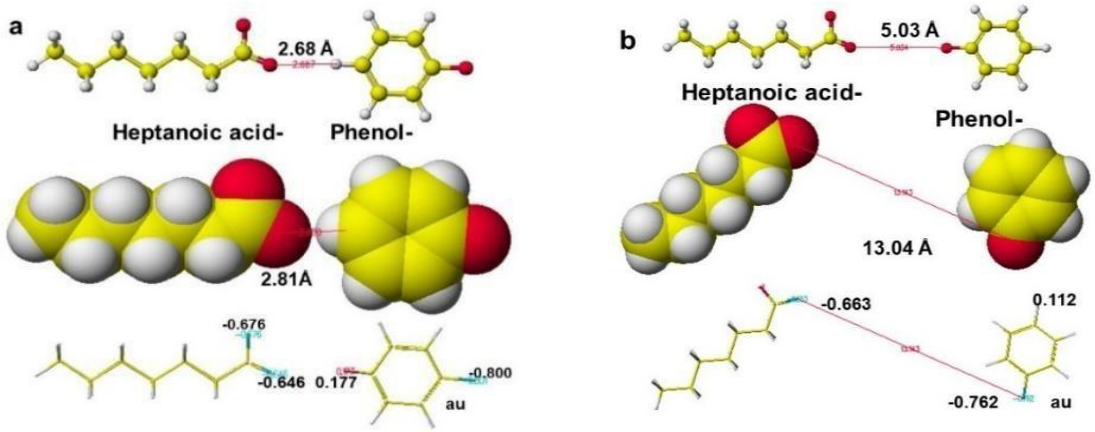

Figures 12a and b. Docking of ionized heptanoic acid with ionized phenol and the apc values

Ionized benzoic acid was repulsed from the carboxy ion; however, the hydrophobic site may contact *via* weak MIVW (0.693 kcal·mol^{-1}). Fundamentally, the ionized carboxy compound was repulsed from the carboxy group, and the negative MIES values and longer atomic distances clearly indicated the evidence in Figures 13a and b.

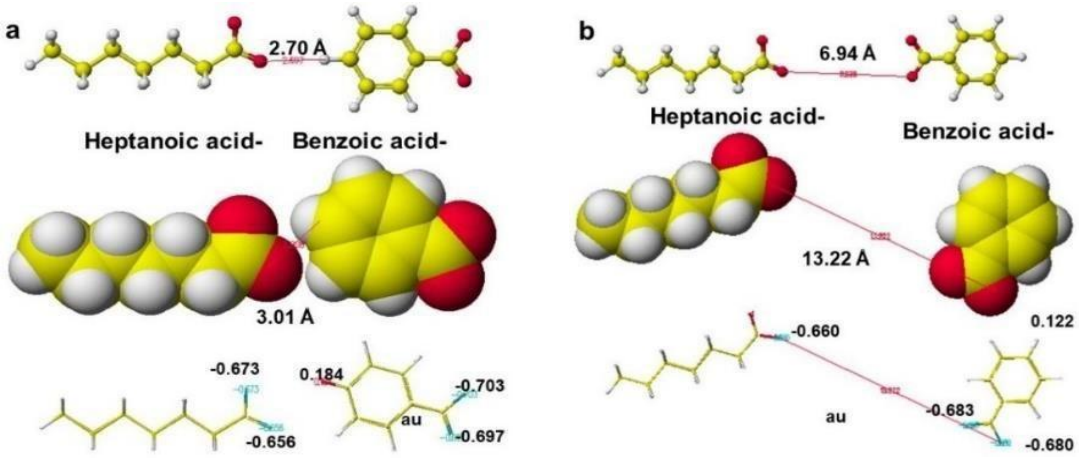

Figures 13a and b. Docking of ionized heptanoic acid with ionized benzoic acid and the apc values

The ionized amino group tightly contacted the carboxy group ever the amino group was located on the opposite side of the carboxy group (Figure 14a). These conformations demonstrated high MIES values (over 7 kcal·mol^{-1}), and the carboxy oxygen apc values were -0.720 and -0.698 from -0.671 au. The amino hydrogen apc were 0.209 and 0.269 from 0.219. A strong ion-ion interaction was observed for their opposite ions (Figure 14b). The molecular interaction energy values are summarized in Table 3, and the conformations are indicated as their Figure numbers.

JAnalTechRes2026; 8 (2): 00-00. DOI:10.26502/jatr.55

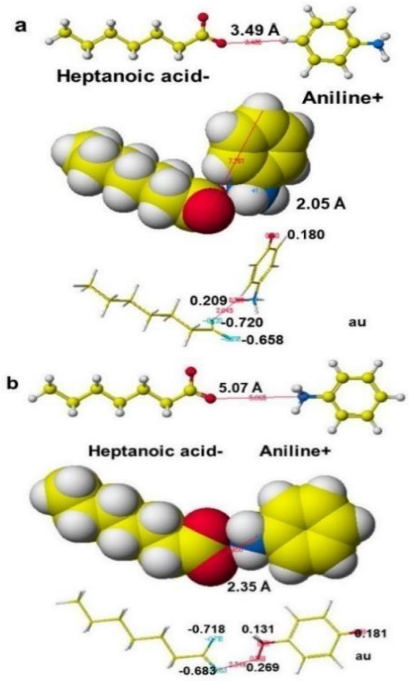

Figures 14a and b. Docking of ionized heptanoic acid with ionized aniline and the apc values

Table 3 Molecular interaction energy values after ionized heptanoic acid docking with analytes

Molecule	MIHB	MIES	MIVW	Figure
Benzene	0.000	0.000	0.368	6
Methylbenzene R	0.000	-0.063	0.382	7a
Methylbenzene L	0.000	0.244	0.538	7b
Chlorobenzene R	0.000	1.137	1.660	8a
Chlorobenzene L	0.000	0.048	0.080	8b
Phenol R	0.003	-0.040	0.371	9a
Phenol L	0.003	2.217	0.480	9b
Benzoic acid (M) R	0.007	0.222	0.385	10a
Benzoic acid (M) L	-0.199	2.150	0.424	10b
Aniline (M) R	0.001	0.030	0.374	11a
Aniline (M) L	-0.002	0.424	0.807	11b
Phenol (I) R	0.000	-1.310	0.347	12a
Phenol (I) L	0.000	-0.638	0.000	12b
Benzoic acid (I) R	0.000	-0.696	0.693	13a
Benzoic acid (I) L	0.000	-0.680	-0.007	13b
Aniline (I) R	0.000	7.904	0.322	14a
Aniline (I) L	0.000	7.261	0.923	14b

R & L: Substitutes faced toward carboxyl group and phenyl group faced toward carboxyl group. M & I: molecular & ionized form analytes; MIHB, MIES, MIVW: molecular interaction energy values of hydrogen bonding, electrostatic interaction, and van der Waals force, unit: kcal·mol^{-1}

1.2.2 The fundamental activity of amino-group

Molecular form amino group exits in over pH 12 solution due to water being a mixture of OH ion and H_3O ion. However, amino group behavior was analyzed in ionized form to make clear the hydrogen bonding and ionic capabilities. Therefore, the binding of ionized hexylamine with the same analytes used for studying the carboxyl group activities was performed for this study.

Benzene aromatic ring is capable of hydrogen bonding. However, when benzene was located at a 3Å distance, benzene docked with the amino group after optimizing the conformation with MIVW 0.621 kcal·mol^{-1}. The amino hydrogen apc changed from 0.225 to 0.232 au. The benzene hydrogen apc changed from 0.156 to 0.093 au. This result also supported the contact site (Figure 15).

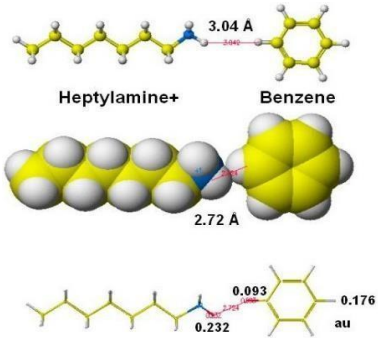

Figure 15. Docking of ionized heptylamine with benzene and the apc.

Due to the weak molecular interaction, methylbenzene was also bound with the amino group when it was initially located in 3Å. The MIVW energy values were 0.983 and 0.760 kcal·mol^{-1}, respectively, shown in Figures 16a and b. Initially, the amino group faced the phenyl group produced higher apc change than that faced the methyl group.

The apc value of amino-hydrogen was 0.230 au (Figure 16a) and 0.228 au (Figure 16b), respectively. Their contact also indicated the electron localization of other atoms.

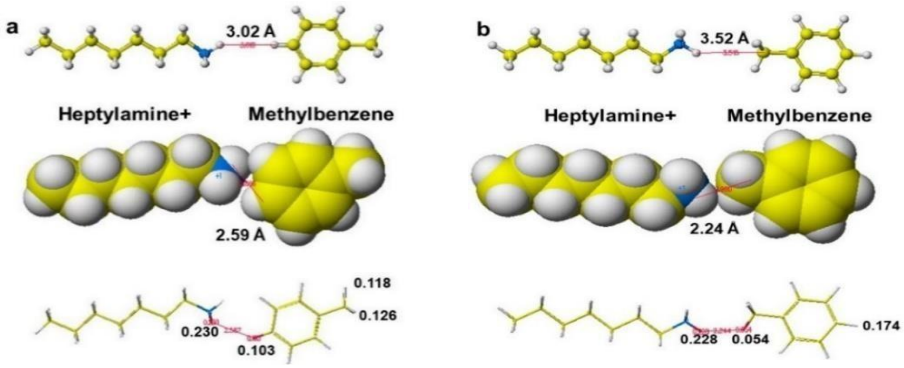

Figures 16a and b. Docking of heptylamine with methylbenzene and the apc values

When the chlorine of chlorobenzene faced the amino group at a 5Å distance, they docked together with MIVW 1.156 kcal·mol^{-1} (Figure 17b). The MIES was 0.651, but MIHB was zero kcal·mol$^{-1,}$ and the electron localization was induced by the contact. The chlorine apc changed from -0.051 to -0.113 au. The contact between the amino group and the phenyl group induced the electron localization (Figure 17a); however, the actual docking should occur between the amino group and the chlorine.

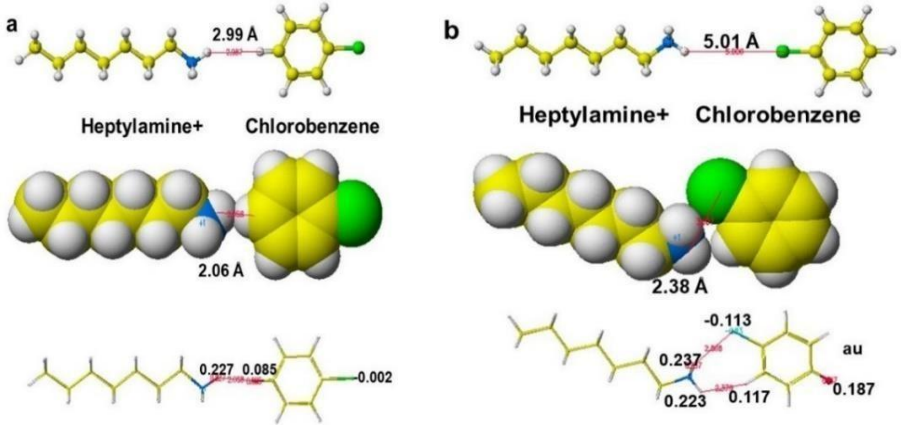

Figures 17a and b. Docking of heptylamine with chlorobenzene and the apc values

The docking with phenol was based on the van der Waals force (MIVW) 0.955 and 0.943 kcal.mol^{-1}, respectively, in Figures 16a and b). The amino group contacted with the acidic hydroxy group produced MIES 0.547 kcal.mol-1(Figure 18b). The contact strength can be read from apc changes. The amino hydrogen apc of Figures 18a and b were 0.228 and 0.246 from 0.225 au. The phenolic oxygen apc changed from -0.386 to -0.436 kcal.mol^{-1}.

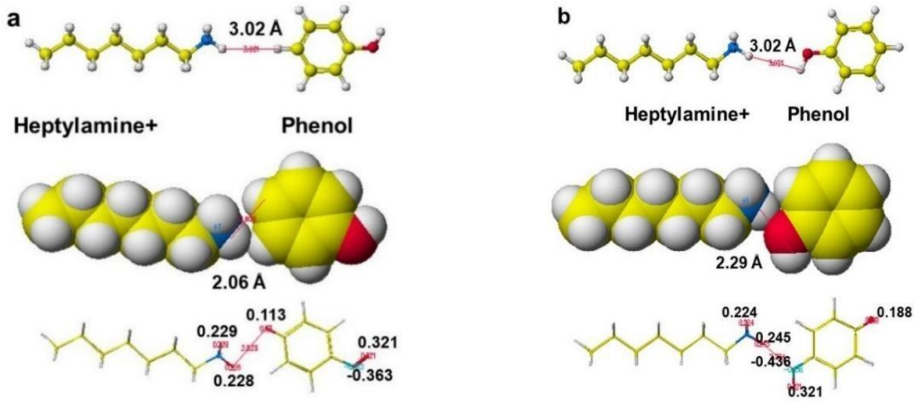

Figures 18a and b. Docking of heptylamine with phenol and the apc values

The actual docking occurred between the amino group and the hydroxy group, as shown in Figure 18b. The benzoic acid docking was similar to that of phenol. The docking of the amino group with the benzoic acid carbonyl group produced a high MIES value (2.575 kcal·mol^{-1}). The carbonyl oxygen apc changed from 0.470 to -0.573 au, as shown in Figure 19a. The change was little when the amino group contacted the phenyl group (Figure 19a), and the van der Waals force contributed to the contact (MIVW 0.938 kcal·mol^{-1}). The actual docking should occur like Figure 19b.

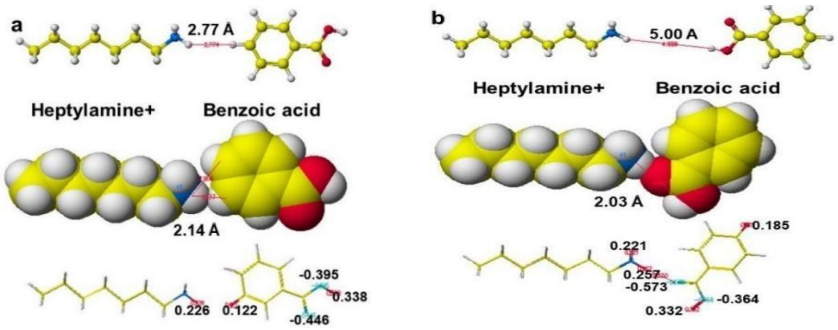

Figures 19a and b. Docking of heptylamine with benzoic acid and the apc values

The docking of the amino group with aniline was weak, and the main interaction was van der Waals force. The MIVW values were 0.626 and 0.686 kcal·mol^{-1}, respectively (Figures 20a and b). The aniline nitrogen apc changed from 0.182 to -0.447 au. The Figure 20b form should be the actual conformation.

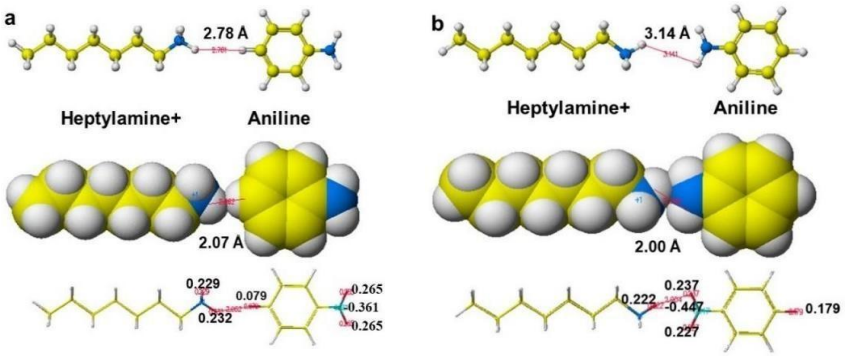

Figures 20a and b. Docking of heptylamine with aniline and the apc values

The docking of ionized phenol produced the electrostatic force. Their MIES values were 1.288 and 4.010 kcal·mol^{-1}, respectively (Figures 21a and b). Even though these molecules were separated 6Å apart, the oxygen apc changed from -0.759 to -0.813 au. The *p*-hydrogen apc changed from 0.112 to 0.141 au. The higher apc value change compared to the above molecules indicated the binding strength.

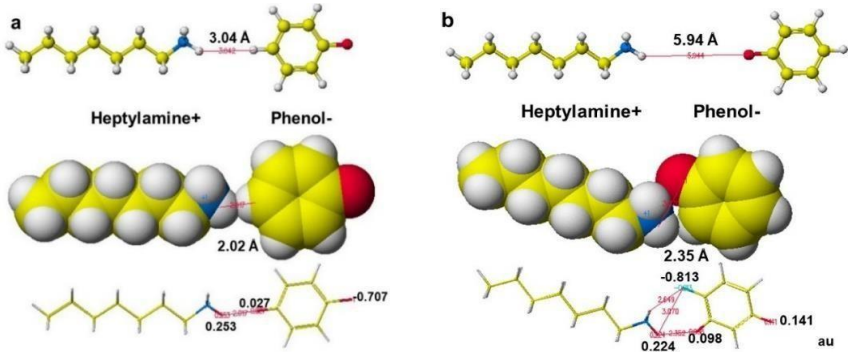

Figures 21a and b. Docking of heptylamine with ionized phenol and the apc values

The docking of further acidic benzoic acid ionized produced a strong electrostatic force. Their MIES values were 6.972 kcal·mol^{-1}, (Figures 22b). Even these molecules were separated to 5Å; the strong interaction bound together.

The oxygen apc changed from -0.759 to -0.695 au. The *p*-hydrogen apc changed from 0.112 to 0.146 au. The docking between the amino group with the phenyl group (Figure 22a) was possible due to the van der Waals force (MIVW 0.839 kcal·mol^{-1}). MIES (0.838 kcal·mol^{-1}) indicated the contribution of electrostatic interaction.

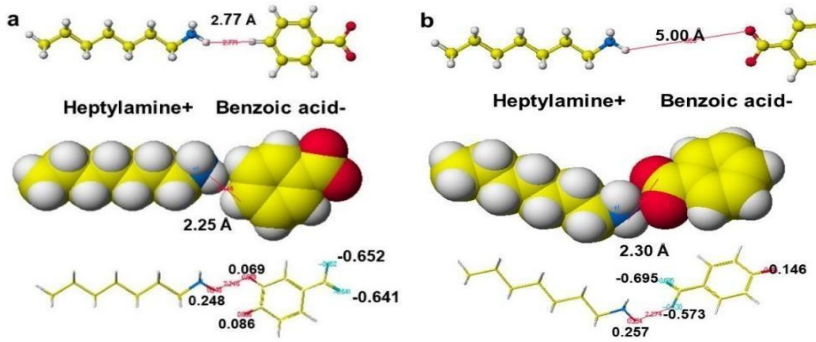

Figures 22a and b. Docking of heptylamine with ionized benzoic acid and the apc values

The same charge ionized aniline contact was rejected from the amino group (Figure 23b). The phenyl group contacted the amino group with van der Waals force (Figure 23a). The amino group hydrogen apc changed from 0.225 to 0.205 au, and phenyl *p*-hydrogen apc changed from 0.206 to 0.153 au. The latter result indicated a possible contact of ionized amino compounds. The molecular interaction energy values docking with the heptyl amines are summarized in Table 4.

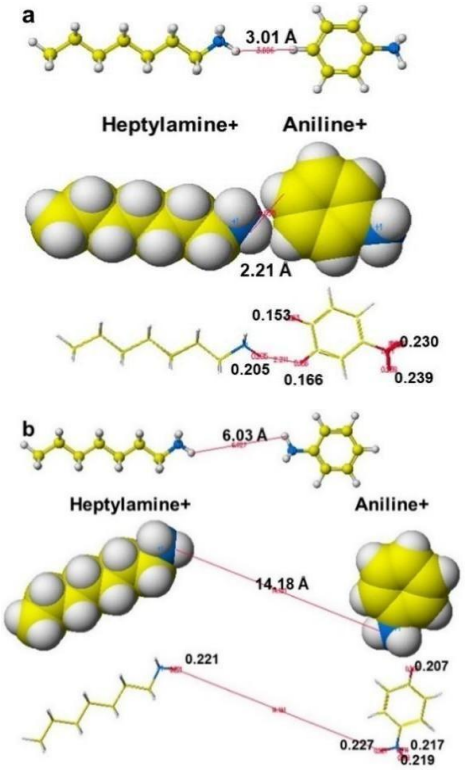

Figures 23a and b. Docking of heptylamine with ionized aniline and the apc values

Table 4. Molecular interaction energy values after ionized heptylamine docking with analytes

Molecule	MIHB	MIES	MIVW	Figure
Benzene	0.000	0.000	0.621	15
Methylbenzene R	0.000	0.071	0.983	16a
Methylbenzene L	0.000	-0.193	0.760	16b
Chlorobenzene R	0.000	-0.305	0.611	17a
Chlorobenzene L	0.000	0.651	1.156	17b
Phenol R	-0.002	0.095	0.955	18a
Phenol L	0.005	0.547	0.943	18b
Benzoic acid (M) R	-0.009	-0.060	0.938	19a
Benzoic acid (M) L	-0.038	2.575	0.650	19b
Aniline (M) R	0.000	-0.026	0.626	20a
Aniline (M) L	0.306	0.072	0.686	20b
Phenol (I) R	0.000	1.288	0.637	21a
Phenol (I) L	0.000	4.010	0.886	21b
Benzoic acid (I) R	0.000	0.838	0.839	22a
Benzoic acid (I) L	0.000	6.972	0.421	22b
Aniline (I) R	0.000	-1.110	0.936	23a
Aniline (I) L	0.000	-0.595	-0.003	23b

R & L: Substitutes faced toward the amino group and phenyl group faced toward the amino group. M & I: molecular & ionized form analytes; MIHB, MIES, MIVW: molecular interaction energy values of hydrogen bonding, electrostatic interaction, and van der Waals force. unit: kcal·mol^{-1}.

1.2.2 The fundamental activity of guanidino-group

The following demonstration indicated hydrogen bonding capability as observed for a guanidino-phase was used saccharide recognition. A guanidino group consisted of amino and ionized amino groups as a computational model and not as a resonance structure; therefore, it demonstrates hydrogen bonding and ion-ion interaction capability. Benzene ring directly contacted the guanidino group with hydrogen bonding (MIHB 3.255 kcal·mol^{-1}). The contact site nitrogen and hydrogen apc values changed from -0.368 and 0.305 to -0.377 and 0.324 au. The MIVW was 2.364 kcal·mol^{-1} and the van der Waals force contributed to the interaction.

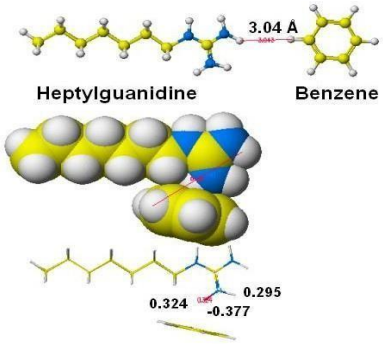

Figure 24. Docking of heptylguanidine with benzene and the apc values

When the guanidino group faced the phenyl group (Figure 25a), hydrogen bonding was the primary interaction (MIHB 4.487 kcal·mol^{-1}), and van der Waals force contributed to the interaction (MIVW 1.784 kcal·mol^{-1}). The contacted guanidino hydrogen apc values changed to 0.311 and 0.323 from 0.298 and 0.300 au. The nitrogen apc changed from -0.402 and -0.368 to -0.414 and -0.386 au. The guanidino group contact with the methyl group (Figure 25b)was weak, and the MI energy values were small. The guanidino hydrogen apc was 0.300 from 0.298 au. The methyl hydrogen apcs were 0.087 and 0.088 from 0.105 and 0.108. Therefore, the contact conformation should be like Figure 25a.

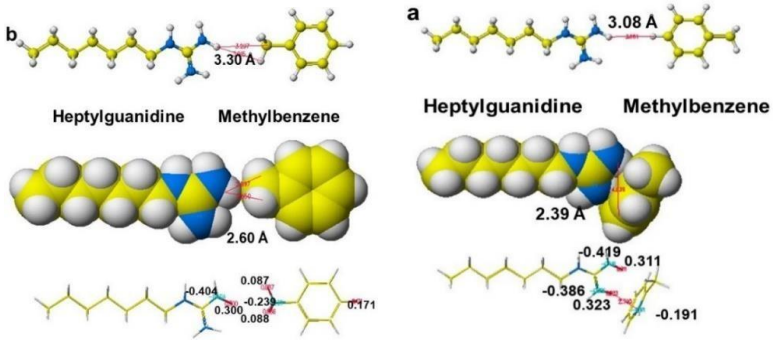

Figures 25a and b. Docking of heptylguanidine with methylbenzene and the apc values

The initial position did not affect the MI energy values, but the guanidino group and chlorine interaction were strong even though both separated 5Å. The electrostatic interaction was the main force, and MIES values were 4.564 and 4.723 kcal·mol^{-1}. Van der Waals interaction also contributed; the MIVW values were 1.559 and 1.477 kcal·mol^{-1}. The contact guanidino hydrogen apc changed from 0.298 to 0.316 or 0.315 au.

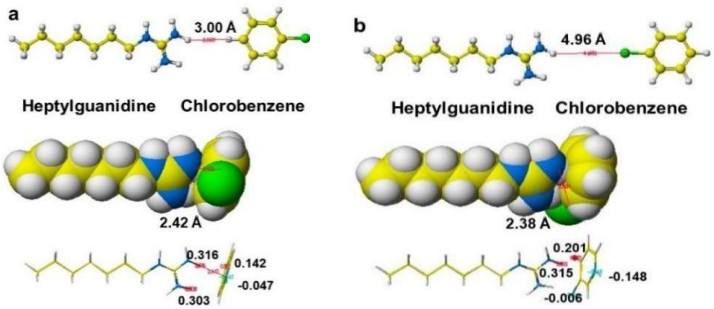

Figures 26a and b. Docking of heptylguanidine with chlorobenzene and the apc values

The complex conformation with phenol was similar to that of chlorobenzene. The primary interaction force is electrostatic interaction. The MIES values of Figures 27a and b were 4.829 and 4.832 kcal·mol^{-1}, and MIVW values indicated the contribution of van der Waals force. It seemed the guanidino group directly interacted with the phenyl group.

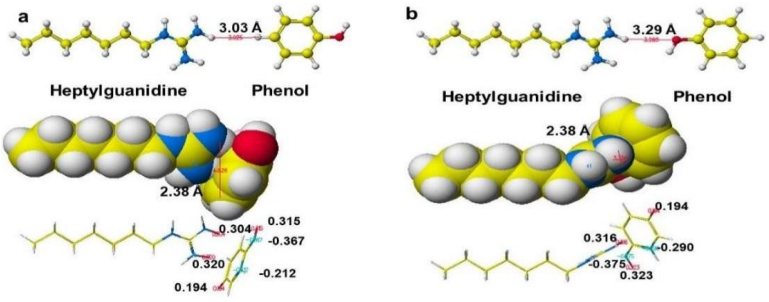

Figures 27a and b. Docking of heptylguanidine with phenol and the apc values

The conformation of the guanidino group complexes with the benzoic acid was similar to others. The guanidino group contacted the phenyl group and produced MIES values. The guanidino hydrogen apc change indicated the contact center, and the value changed from 0.305 to 0.316 au. The benzoic acid-hydroxy oxygen apc changed from -0.410 to -0.399 au.

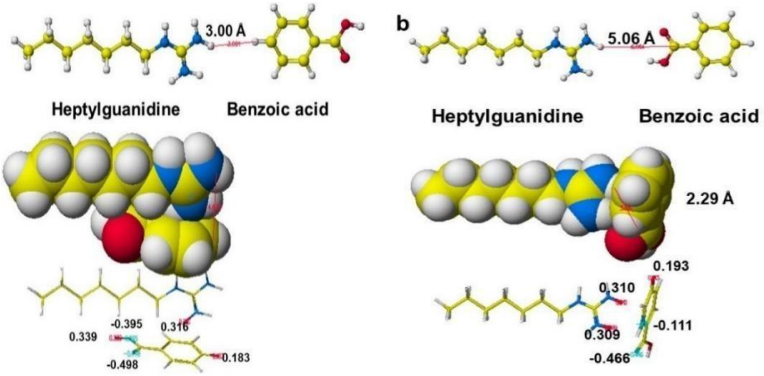

Figures 28a and b. Docking of heptylguanidine with benzoic acid and the apc values

The conformation of the complex with aniline was a little different from acidic compounds. The guanidino group contacted the phenyl group (Figure 29a) and produced MIES energy (4.522 kcal·mol^{-1}). However, the guanidino group contact with the amino group was weak, and MIES and MIVW values were small (MIES and MIVW, 0.236 and 0.552 kcal·mol^{-1}.

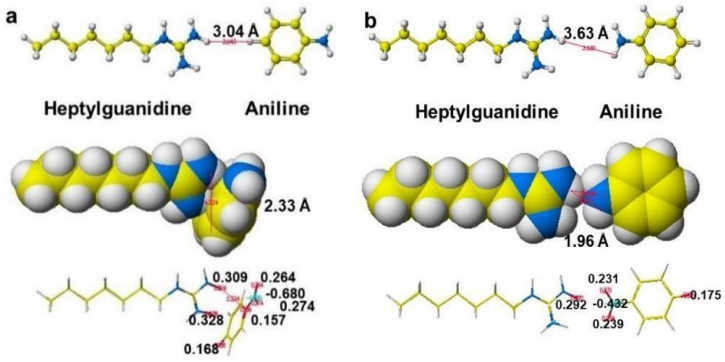

Figures 29a and b. Docking of heptylguanidine with aniline and the apc values

The contribution of MIES played an important role in the complex formation of the guanidino group with ionized phenol; even this phenomenon occurs in very high pH solutions due to the high pKa values of phenol. The MIES values of Figures 30a and b were 2.868 and 3.434 kcal·mol^{-1}. The phenolic oxygen apc changed from -0.759 to -0.721 and -0.717, and the guanidino hydrogen apc values were 0.342 and 0.356 from 0.305 and 0.295 in Figures 30a and b.

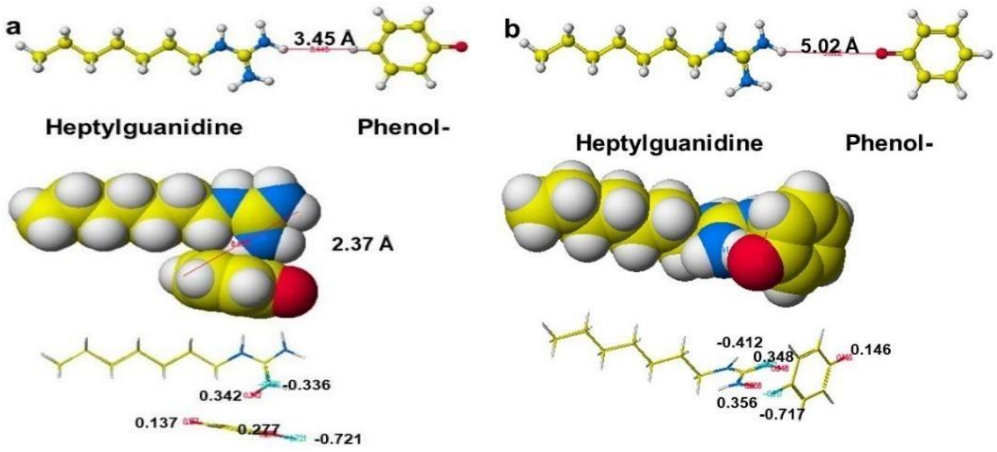

Figures 30a and b. Docking of heptylguanidine with ionized phenol and the apc values

The ionized benzoic acid conformation was not the same as acidic phenol. The ion-ion interaction (electrostatic interaction) was essential in Figure 31b. The MIES energy (5.346 kcal·mol^{-1}) supported the conclusion. The oxygen apc values changed from -0.673 to -0.689 and -0.724 au (Figure 31b), and the guanidino hydrogen apc was 0.360 from 0.3 au. The apc changed a little in Figure 31a conformation. The results indicate the actual conformation should be Figure 31b.

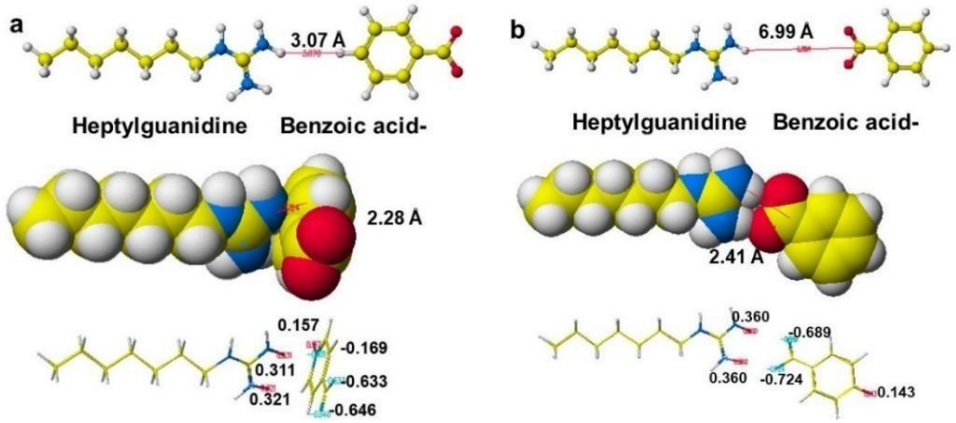

Figures 31a and b. Docking of heptylguanidine with ionized benzoic acid and the apc values

The binding with the same charge ionized aniline was different from that of acidic compounds. The ionized amino group was repulsed from the guanidino group (Figure 32b). The possible interaction was with the phenyl group as done with acidic compounds via hydrogen bonding (Figure 32a). The calculated molecular interaction energy values for heptylguanidine docking are summarized in Table 5 with Figure numbers.

The direct molecular interaction of ion-exchange groups was investigated using simple molecules. The quantitative analysis should make clear the qualitative speculation of molecular interactions of various compounds with proteins. Even actual compounds combine various groups; the simple experience can estimate the fundamental mechanisms.

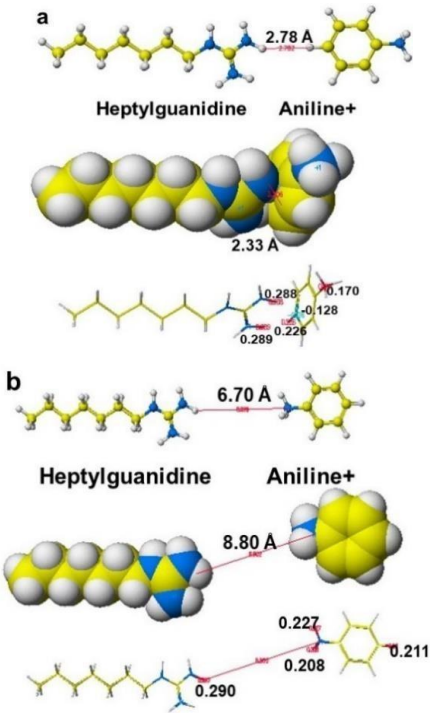

Figures 32a and b. Docking of heptylguanidine with ionized aniline and the apc values

Table 5. Molecular interaction energy values after heptylguanidine docking with analytes

Molecule	MIHB	MIES	MIVW	Figure
Benzene	3.258	-0.017	2.364	24
Methylbenzene R	4.487	0.178	1.784	25a
Methylbenzene L	0.074	-0.105	0.705	25b
Chlorobenzene R	4.561	-0.557	1.559	26a
Chlorobenzene L	4.723	-0.335	1.477	26b
Phenol R	4.829	0.203	1.379	27a
Phenol L	4.832	0.385	1.858	27b
Benzoic acid (M) R	3.375	-0.388	3.397	28a
Benzoic acid (M) L	4.634	0.565	1.616	28b
Aniline (M) R	4.522	0.015	1.559	29a
Aniline (M) L	0.236	0.019	0.562	29b
Phenol (I) R	3.356	2.868	2.242	30a
Phenol (I) L	4.734	3.434	1.733	30b
Benzoic acid (I) R	4.496	0.851	1.610	31a
Benzoic acid (I) L	0.096	5.364	0.563	31b
Aniline (I) R	4.519	-1.188	1.420	32a
Aniline (I) L	0.001	-0.931	-0.023	32b

R & L: Substitutes faced toward guanidino group and phenyl group faced toward guanidino group. M & I: molecular & ionized form analytes; MIHB, MIES, MIVW: molecular interaction energy values of hydrogen bonding, electrostatic interaction, and van der Waals force, unit: kcal·mol^{-1}.

17

1.3. Solvent (water) effect

1.3.1 Solvent effect for the binding with ionized carboxy-group

Molecular interactions usually occur in aqueous physiological conditions. The solvent is water containing buffer components. Water molecules contribute both solubility and binding molecules with proteins critically. Hydrophobic analytes are repulsed from water molecules and attached with proteins, and hydrophilic analytes are solvated with water molecules. The following experiments are the simplest experience. The contribution of water can be analyzed by a competitive interaction between an ionized group and a water molecule.

An analyte was located at the center of an ion-exchange group, and a water molecule was located 15Å distance, as shown in the following Figures. Then, the initial conformations were optimized to determine whether the analyte should contact either the ion-exchange group or the water molecule. The strong contact or repulsion depends on the molecular properties of analytes, as studied in previous chapters. The optimized conformations are summarized in Figures 33.1-17. Analytes who have weak interaction with the carboxy group did not show clear moving like benzene and methylbenzene. However, high electron density chlorine was repulsed from the carboxy group (Figure 33.5), and the chlorine and *p*-hydrogen apc values were changed a little from -0.051 and 0.163 to -0.043 and 0.157. But they did not form a complex, and the chlorine contacted the water molecule high MIHB (14.947 kcal·mol^{-1}). The atomic distance expanded to 16.19 Å. In Figure 33.7, the phenol moved toward the carboxyl group and was contacted by hydrogen bonding (MIHB 1.396 kcal·mol^{-1}). The phenol hydroxy group hydrogen apc changed to 0.375 from 0.305 au, and the carboxy oxygen apc was -0.704 from -0.671 au. The phenol was in favor of contacting the carboxyl group.

Benzoic acid formed hydrogen bonding with a near water molecule (MIHB 10.322 kcal·mol^{-1}), and the hydroxy hydrogen and carbonyl oxygen apc values changed to 0.330 and -0.515 from 0.324 and -0.470 au (Figure 33.8). The phenol contacted the carboxy group by MIES (2.081 kcal·mol^{-1}) and MIVW (2.740 kcal·mol^{-1}). The contact center was between the carboxy ionized oxygen and the benzoic acid carboxyl group (Figure 33.9). No

significant MI values were obtained for the behavior of aniline. Ionized phenol moved dynamically to form hydrogen bonding with the water molecule. MIHB energy values were 12 kcal·mol^{-1}. The water hydrogen apc values changed from 0.250 au to either 0.275 or 0.293 au (Figures 33.12 and 13). The ionized benzoic acid was repulsed by the carboxy group and trapped by the water molecule (MIHB 11.446 kcal·mol^{-1}) in Figure 33.15. However, the ionized benzoic acid contacted the water molecule by electrostatic force (MIES 2.588 kcal·mol^{-1}). The benzoic acid carbonyl oxygen apc and the water molecule hydrogen apc were changed to -0.681 and 0.261 from -0.673 and 0.250 (Figure 33.14). The ionized aniline demonstrated solid electrostatic interaction with the carboxy group (MIES 7.954 kcal·mol^{-1}), and the amino nitrogen apc was 0.151 from 0.182 au. The ion-ion interaction is the contact center (Figure 33.17). The electron localization within aniline was observed from *p*-hydrogen apc change from 0.260 to 0.182 au. The MI energy values are summarized in Table 6 with Figure numbers.

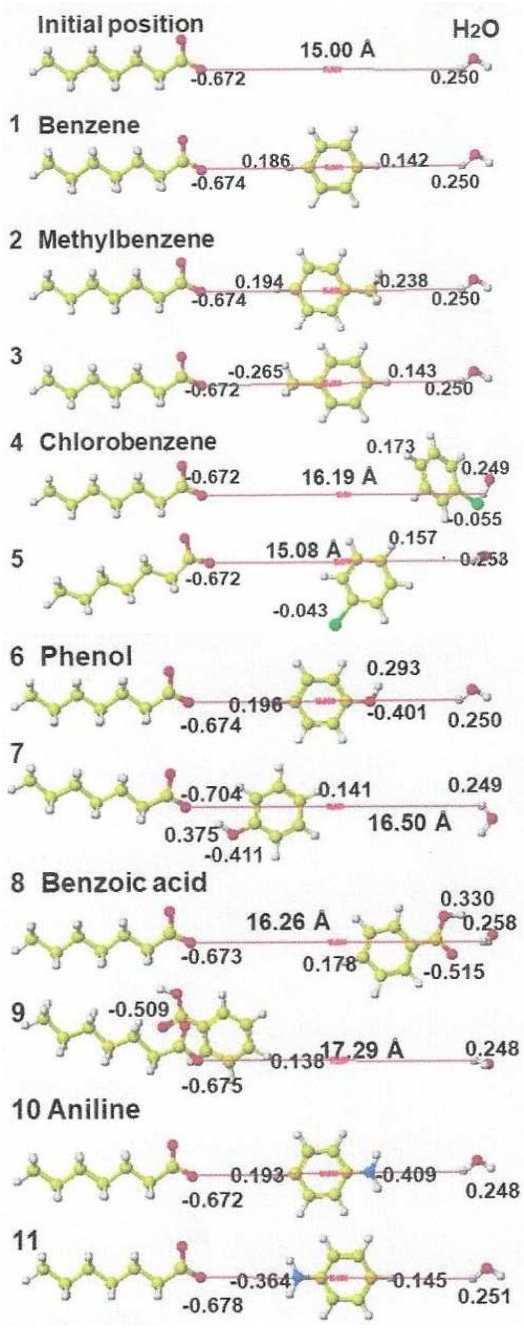

Figure 33.1-17. Contribution of a water molecule in the ionized carboxy group and analyte binding

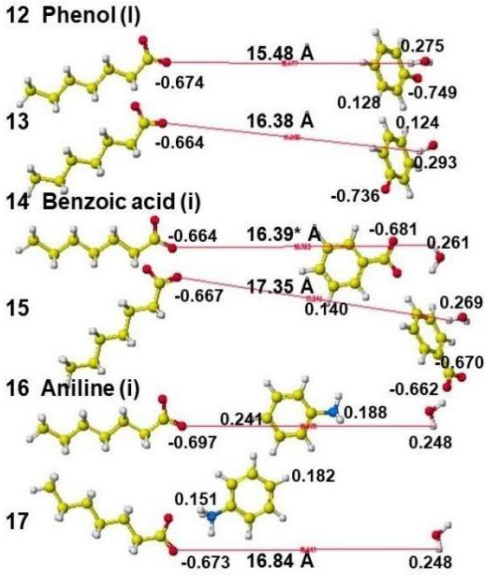

Table 6. Compete for molecular interaction between ionized heptanoic acid and water

Molecule	MIHB	MIES	MIVW	Figure
Benzene	0.026	-0.007	0.067	33.1
Methylbenzene R	0.015	-0.057	0.134	33.2
Methylbenzene L	0.045	0.092	0.127	33.3
Chlorobenzene R	0.090	-0.012	0.078	33.4
Chlorobenzene L	14.947	0.059	-1.218	33.5
Phenol R	0.057	0.009	0.083	33.6
Phenol L	0.011	1.396	0.459	33.7
Benzoic acid (M) R	10.322	2.427	-0.802	33.8
Benzoic acid (M) L	-0.018	2.081	2.740	33.9
Aniline (M) R	0.022	0.010	0.094	33.10
Aniline (M) L	0.036	-0.009	0.094	33.11
Phenol (I) R	11.964	0.452	-0.588	33.12
Phenol (I) L	11.674	-0.050	-0.454	33.13
Benzoic acid (I) R	0.220	2.588	0.144	33.14
Benzoic acid (I) L	11.446	-0.683	-0.288	33.15
Aniline (I) R	0.009	1.280	0.136	33.16
Aniline (I) L	0.001	7.954	0.207	33.17

R & L: Substitutes faced toward carboxyl group and phenyl group faced toward carboxyl group. M & I: molecular & ionized form analytes; MIHB, MIES, MIVW: molecular interaction energy values of hydrogen bonding, electrostatic interaction, and van der Waals force, unit: kcal·mol^{-1}.

1.3.2 Solvent effect for the binding with ionized amino-group

The ionized amino group lacks hydrogen bonding capability. No clear evidence was observed for benzene and methylbenzene. Chlorobenzene was contacted with water via hydrogen bonding (MIHB 14.681 kcal·mol^{-1}), shown in Figure 33.21. The chlorine apc changed from -0.051 to -0.039 au. However, the chlorine contact with the amino group via electrostatic interaction (MIES 1.174 kcal·mol^{-1}). The chlorine apc was changed from -0.051 to -0.178 au, and the electron localization induced the *p*-hydroxy hydrogen apc from 0.163 to 0.184 au. The amino group hydrogen indicated the contact, and the apc changed from 0.225 to 0.234 au. The electron localization in phenol occurred, but it did not move for their contact. Benzoic acid carbonyl contacted the amino group *via* electrostatic interaction (2.578 kcal·mol^{-1}) shown in Figure 33.26. The carbonyl oxygen aps changed from -0.470 to -0.571 au. The amino group hydrogen apc changed from 0.225 to 0.257 au. The contact site was clear, and ionized amino groups should trap molecular form carboxy compounds. Electron localization of aniline was observed, but the contact did not occur.

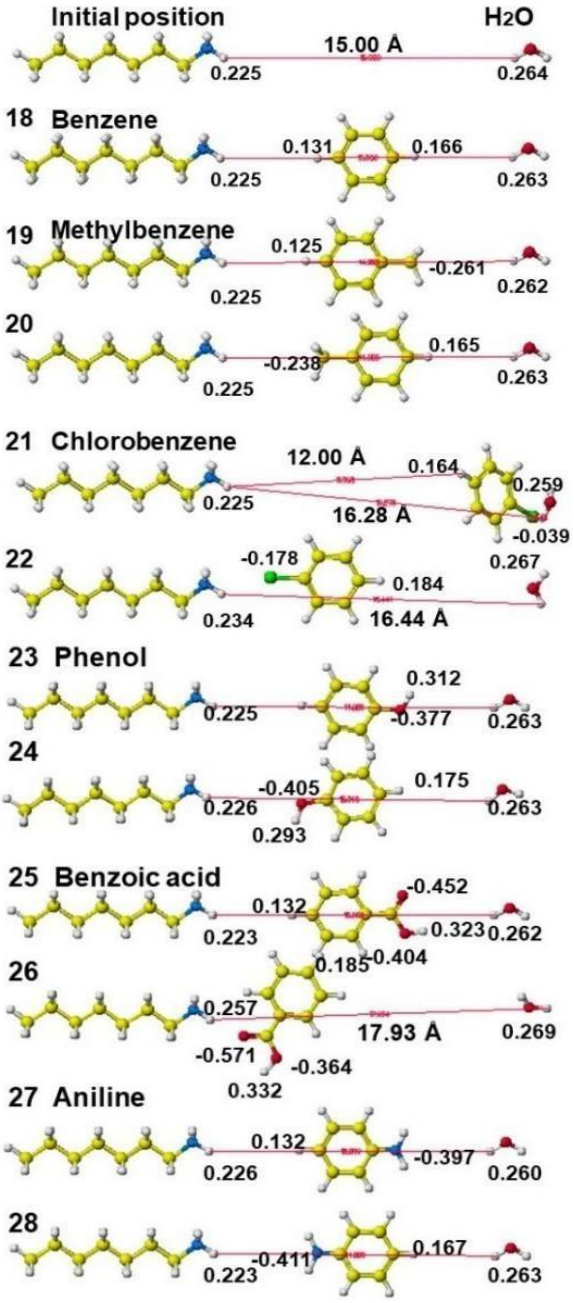

Figure 33.18-34. Contribution of a water molecule in the ionized amino group and analyte binding

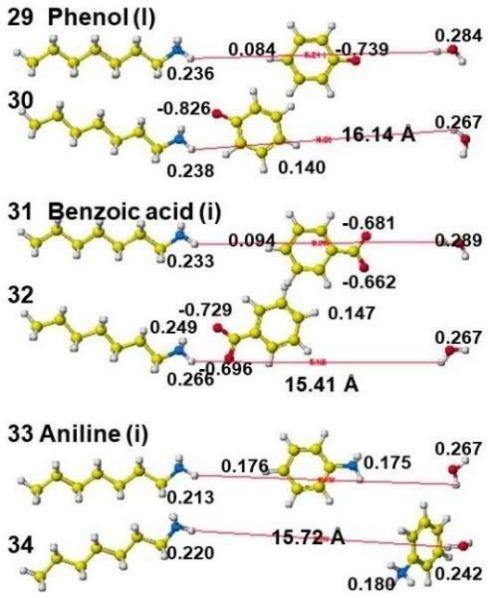

Table 7. Compete for molecular interaction between heptylguanidine and water

Molecule	MIHB	MIES	MIVW	Figure
Benzene	0.023	0.000	0.059	33.18
Methylbenzene R	0.013	0.027	0.114	33.19
Methylbenzene L	0.041	-0.072	0.101	33.20
Chlorobenzene R	14.681	-0.053	-1.710	33.21
Chlorobenzene L	0.004	1.173	0.515	33.22
Phenol R	0.050	0.053	0.077	33.23
Phenol L	0.037	-0.013	0.068	33.24
Benzoic acid (M) R	0.119	-0.217	0.123	33.25
Benzoic acid (M) L	-0.038	2.578	0.679	33.26
Aniline (M) R	0.024	-0.009	0.071	33.27
Aniline (M) L	0.044	0.005	0.066	33.28
Phenol (I) R	0.028	1.108	0.082	33.29
Phenol (I) L	0.002	4.040	0.755	33.30
Benzoic acid (I) R	0.014	1.016	0.115	33.31
Benzoic acid (I) L	0.003	6.953	0.457	33.32
Aniline (I) R	0.008	-0.438	0.088	33.33
Aniline (I) L	11.294	-0.710	-0.745	33.34

R & L: Substitutes faced the guanidyl group, and the phenyl group faced the guanidyl group. M & I: molecular & ionized form analytes; MIHB, MIES, MIVW: molecular interaction energy values of hydrogen bonding, electrostatic interaction, and van der Waals force, unit: kcal·mol^{-1}.

Ionized phenol produced electron localization of the amino group and the water molecule but did not contact the amino group and water molecule (Figure 33.29). However, the ionized oxygen contacted the amino group via electrostatic interaction (MIES 4.040 kcal.mol^{-1}) shown in Figure 33.30, and the phenolic oxygen apc changed from -0.739 to -0.826 au. The ionized benzoic acid demonstrated similar phenomena as ionized phenol. Figure 33.31 exhibits their electron localization without their docking. However, the ionized carboxy group contacted the amino group via electrostatic interaction (MIES 6.953 kcal·mol^{-1}). The oxygen apc changed from -0.673 to -0.729, and the amino group hydrogen apc changed from 0.225 to 0.226 au. The result indicates the strength of the acid-base interaction.

The ionized aniline was repulsed by the amino group and trapped by the water molecule (Figure 33.34). The hydrogen bonding between the water and the phenyl groups was observed (MIHB 11.294 kcal·mol^{-1}). The ionized amino group nitrogen and *p*-hydrogen apc values were not changed significantly. These experiences indicated the strong repulsion and interaction moved the partly locked amino group and the water molecule as observed at the longer atomic distances. Once the water molecule was not locked, both the water molecule and the analyte disappeared from the monitor screen. Therefore, docking a part of these molecules is necessary to study molecular interactions. The optimized conformations are summarized in Figures 33.2-17. The calculated molecular interaction energy values for a water molecule effect of the ionized heptyl amine recognition analytes are summarized in Table 7.

1.3.3 Solvent effect for the binding with guanidino-group

The arginine ion-exchange group is capable of hydrogen bonding and ion-ion interaction as the computational chemical model. The difference from the lysine amino group is an exciting subject. The existence of benzene and methylbenzene caused a little electron localization, but their contact was not observed. Chlorobenzene chlorine was a key element and contacted the water molecule via hydrogen bonding (MIHB 15.940 kcal·mol^{-1}) and contacted the guanidino group via hydrogen bonding (MIHB 1.073 kcal·mol^{-1}) and electrostatic interaction (MIES 1.029 kcal·mol^{-1}). The contact site was clear in Figure 33.38, the water molecule hydrogen and the chlorobenzene chlorine and *p*-hydrogen apc values indicated. In Figure 33.39, the chlorine and the guanidino hydrogen apc values changed from -0.051 and 0.298 to -0.122 and 0.311 au. The behavior of phenol was different from the results obtained with heptylcarboxyl. There was no contact; even the electron localization was observed. Benzoic acid contacted the guanidino group via hydrogen bonding (MIHB 1.196 kcal·mol^{-1}) and electrostatic interaction (MIES kcal·mol^{-1}) shown in Figure 33.43. The carboxy group oxygen and hydrogen apc indicated the contact site. The carbonyl oxygen and hydroxy hydrogen apc values changed from -0.410 and 0.324 to -0.574 and 0.309 au. The changes in Figure 33.42 conformation were small, and their changed apc values were -0.453 and 0.328 au. The electron localization occurred a little in the aniline but contacted neither the guanidino group nor the water molecule (Figures 33.44 and 45).

The electron localization occurred in the ionized phenol (Figure 46) and affected the electron localization of the water molecule and the guanidino group, but their binding did not occur. The contact of the phenolic oxygen with the guanidino group produced hydrogen bonding (MIHB 4.738 kcal·mol^{-}1) and electrostatic interaction (MIES 3.447 kcal·mol^{-1}). The oxygen and hydrogen apc values changed from -0.663 and 0.288 to -0.686 and 0.360. The water molecule hydrogen apc was also changed by the dynamic moving of ionized benzoic acid from 0.284 to 0.248 au. The ionized aniline amino group repulsed the water molecule and was repulsed from the guanidino group. The water molecule hydrogen apc was changed from 0.289 to 0.250 au (Figure 33.50). Figure 33.51 shows that the repulsed and trapped by the water molecule ionized aniline indicated the bonding with the water molecule was between the water hydrogen and the phenyl group via hydrogen bonding (MIHB 11.625 kcal·mol^{-1}). The calculated MI energy values are summarized in Table 8.

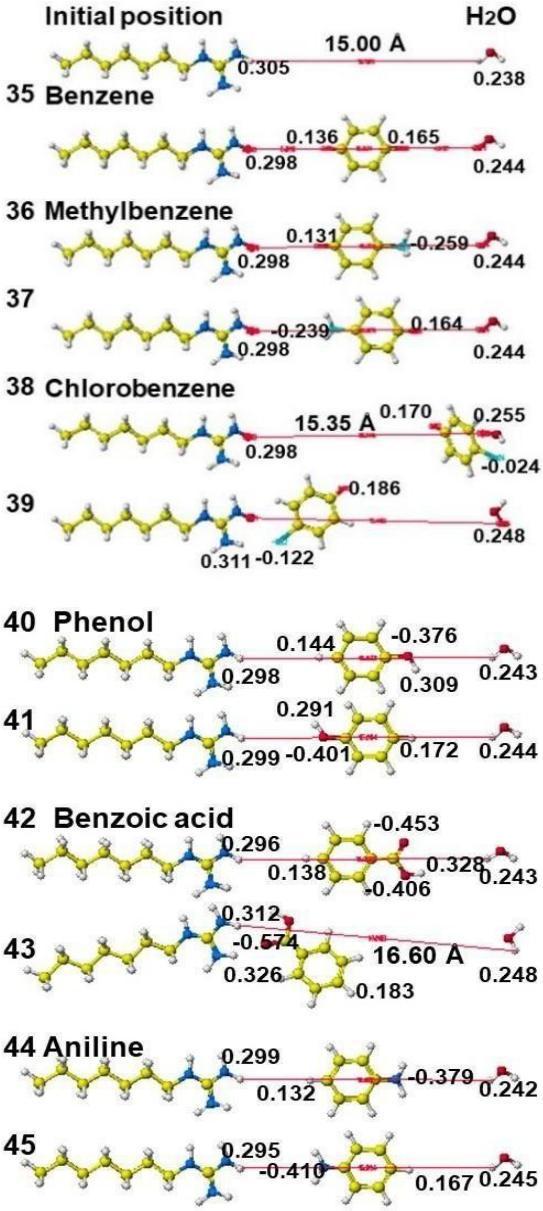

Figure 33.35-51. Contribution of a water molecule in the guanidino group and analyte binding

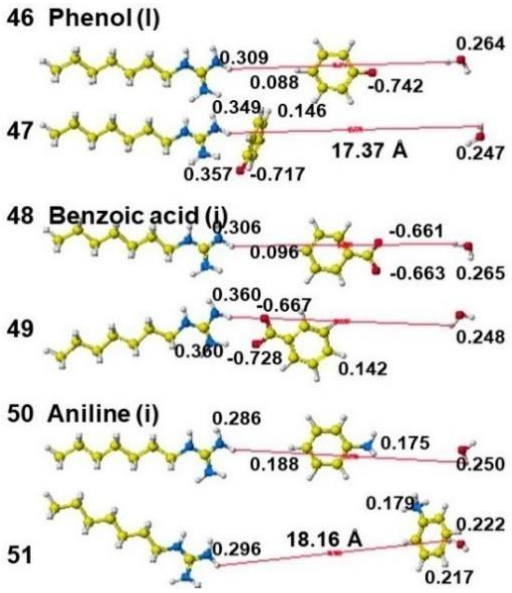

Table 8. Compete for molecular interaction between heptylguanidine and water

Molecule	MIHB	MIES	MIVW	Figure
Benzene	0.014	0.000	0.117	33.35
Methylbenzene R	0.025	0.105	0.223	33.36
Methylbenzene L	0.009	-0.084	0.230	33.37
Chlorobenzene R	0.018	-0.626	0.280	33.38
Chlorobenzene L	4.694	-0.290	1.545	33.39
Phenol R	0.028	0.143	0.139	33.40
Phenol L	0.029	-0.056	0.144	33.41
Benzoic acid (M) R	0.372	0.917	0.196	33.42
Benzoic acid (M) L	0.004	0.543	0.487	33.43
Aniline (M) R	0.032	-0.014	0.138	33.44
Aniline (M) L	0.012	0.015	0.189	33.45
Phenol (I) R	4.780	1.808	1.331	33.46
Phenol (I) L	4.737	2.746	1.159	33.47
Benzoic acid (I) R	4.463	0.381	1.643	33.48
Benzoic acid (I) L	0.142	4.919	0.307	33.49
Aniline (I) R	0.005	3.160	0.278	33.50
Aniline (I) L	0.001	2.481	0.592	33.51

R & L: Substitutes faced the guanidino group, and the phenyl group faced the amino group. M & I: molecular & ionized form analytes; MIHB, MIES, MIVW: molecular interaction energy values of hydrogen bonding, electrostatic interaction, and van der Waals force, unit: kcal·mol^{-1}.

Water molecules affect the molecular interaction of analytes with ion-exchange groups. However, it did not work as an initiative molecule; rather, it worked as a supporter. Furthermore, ions should affect the interaction. Therefore, the existence ion effect was studied using simple sodium and chlorine ions.

1.4. Competition with ions

1.4.1 Competition with Na+ for binding with ionized carboxy-group

Here, a sodium ion was placed instead of a water molecule and studied the positive charged ion effect for the competitive binding. The sodium ion was locked. The carboxy group and sodium-ion induced the electron localization of analytes, but these neutral compounds (benzene and methylbenzene) did not bind with either the carboxy group or sodium ion. Chlorobenzene chlorine a little shifted toward sodium ion via electrostatic Interaction (MIES 0.790 kcal·mol^{-1}). The chlorine apc changed from -0.051 to -0.163 au, and the p-hydrogen apc

also changed from 0.163 to 0.208 au (Figure 34.4). The carboxy group repulsed the chlorine toward the sodium ion (Figure 34.6), and the phenol oxygen contacted the sodium ion-like Lewis acid-base interaction.

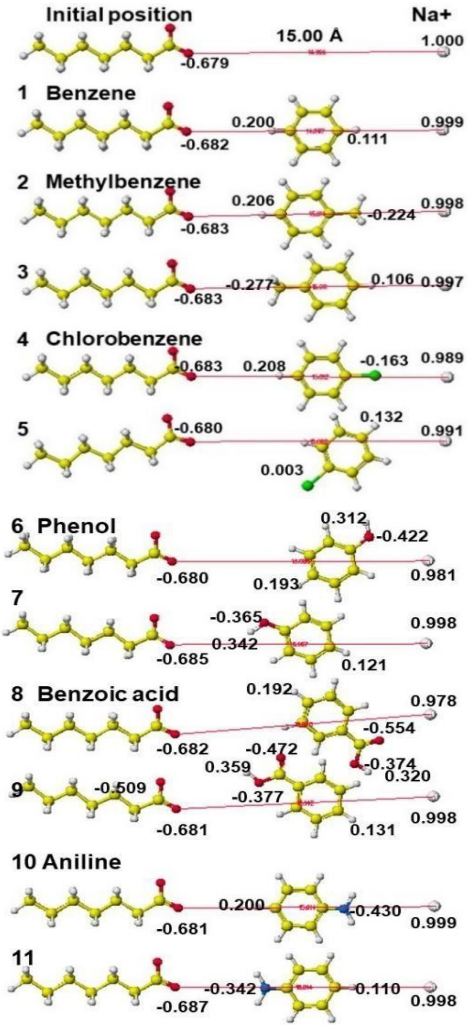

Figure 34.1-17. Contribution of a sodium ion in the ionized carboxy group and analyte binding

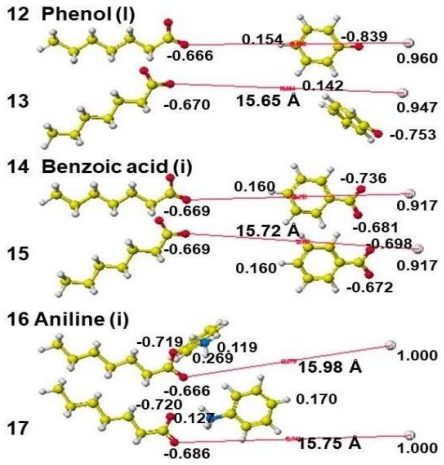

Table 9. Compete for molecular interaction between ionized carboxy-group and sodium ion

Molecule	MIHB	MIES	MIVW	Figure
Benzene	0.000	0.000	0.143	34.1
Methylbenzene R	0.000	0.000	0.172	34.2
Methylbenzene L	0.000	0.137	0.288	34.3
Chlorobenzene R	0.000	0.790	0.335	34.4
Chlorobenzene L	0.000	-0.295	0.389	34.5
Phenol R	0.007	0.266	0.429	34.6
Phenol L	-0.010	0.314	0.228	34.7
Benzoic acid (M) R	-0.023	1.633	0.312	34.8
Benzoic acid (M) L	-0.056	0.535	0.283	34.9
Aniline (M) R	0.001	0.022	0.190	34.10
Aniline (M) L	-0.002	-0.013	0.206	34.11
Phenol (I) R	0.000	1.969	0.043	34.12
Phenol (I) L	0.000	1.877	0.564	34.13
Benzoic acid (I) R	0.000	3.836	0.121	34.14
Benzoic acid (I) L	0.000	3.787	0.105	34.15
Aniline (I) R	0.000	6.761	0.785	34.16
Aniline (I) L	0.000	7.263	0.269	34.17

R & L: Substitutes faced the carboxy group, and the phenyl group faced the carboxy group. M & I: molecular & ionized form analytes; MIHB, MIES, MIVW: molecular interaction energy values of hydrogen bonding, electrostatic interaction, and van der Waals force, unit: kcal·mol^{-1}.

The electron localization was observed from the *p*-hydrogen apc change (0.164 to 0.193 au). The phenolic oxygen seemed rejected from the carboxy group, but a significant electron shift of the oxygen was not observed. The benzoic acid carbonyl oxygen contacted the sodium ion like the phenolic oxygen by electrostatic Interaction (MIES 1.633 kcal·mol^{-1}). The apc changed from -0.470 to -0.554 au (Figure 34.8). The benzoic acid carboxy group was also repulsed from the carboxy group (Figure 34.9). Aniline was like a neutral compound even though the electron was localized (Figure 34.10).

The ionized phenol was kicked off dynamically from the carboxy group and caught by the sodium ion (Figure 34.13). The phenolic oxygen contact with the sodium ion via electrostatic Interaction (MIES 1.999 kcal·mol^{-1}). The oxygen apc changed from -0.759 to -0.839 au, and the sodium ion apc changed from 1.000 to 0.960 au (Figure 34.12). The *p*-hydrogen apc also changed from 0.112 to 0.154 au. The behavior of ionized benzoic acid was the same as that of the ionized phenol, and the ionized carboxy was repulsed from the carboxy group and caught by the sodium ion (Figure 34.15). The oxygen and *p*-hydrogen apc changed from -0.673 and -0.124 to -0.698 and 0.160 au. In Figure 34.14, ionized benzoic acid oxygen contacted the sodium ion, and the oxygen and *p*-hydrogen apc changed from -0.673 and 0.124 to -0.403 and 0.160 au). The primary Interaction was the electrostatic force; the MIES values were 3.836 (Figure 34.15) and 3.787 (Figure 34.14) kcal·mol^{-1}). The plus-charged ionized aniline was repulsed from the sodium ion and contacted the carboxy group (Figure 34.16). The nitrogen apc changed from 0.182 to 0.119, and the hydrogen apc changed from 0.219 to 0.269 au. The primary force was electrostatic Interaction (6.764 kcal·mol^{-1}). In Figure 34.17, the plus charged amino group contacted

the carboxy group by electrostatic Interaction (MIES 7.263 kcal·mol^{-1}). The nitrogen and hydrogen apc changed from 0.182 and 0.219 to 0.127 and 0.271 au. The calculated molecular interaction energy values are summarized in Table 9.

1.4.2. Competition with Na+ for binding with ionized amino-group

The ionized heptylamine and sodium ion are plus charged. The ionic strength should affect the competitive Interaction with analytes. Both the ionized amino group and the sodium-ion induced their electron localization; the analytes benzene, methylbenzene, phenol, and aniline did not contact either the ionized heptylamine or the sodium-ion. The chlorobenzene shifted toward the sodium-ion with weak electrostatic Interaction (MIES 0.521 kcal·mol^{-1}). The chlorobenzene contacted the heptylamine with weak electrostatic Interaction and van der Waals force (MIES 0.549 and MIVW 1.072 kcal·mol^{-1}). Their key atom's apc values were not changed significantly (Figure 34.22). Benzoic acid carbonyl oxygen contacted the sodium-ion (MIES 1.390 kcal·mol^{-1}), and the apc changed from -0.470 to -0.527 au (Figure 34.25). Such electrostatic Interaction was observed between the carboxyl oxygen and heptylamine (MIES 2.586 kcal·mol^{-1}), and the oxygen apc changed from -0.470 to -0.570 au (Figure 34.26). The electron-rich ionized phenolic oxygen bound with both cations via electrostatic Interaction (MIES 3.663 and 4.618 kcal·mol^{-1}) in Figures 34.29 and 30. The oxygen apc changed from -0.759 to -0.808 and -0.803 au. The p-hydrogen apc also changed from 0.124 to 0.111 and 0.130 au. The behavior of ionized benzoic acid was the same as that of the ionized phenol. The ionized carboxyl oxygen contacted the sodium ion and heptylamine via electrostatic Interaction (MIES 5.033 and 7.542 kcal·mol^{-1}). The ionic oxygen apc changed from -0.673 to -0.685 and -0.723 au (Figures 34.31 and 32). The sodium ion apc changed from 1.000 to 0.931, too. The plus charged aniline amino group was repulsed by the sodium ion and the heptylamine. Their MIES values were negative. In Figure 34.33, the kicked aniline contacted the heptylamine alkyl-group via van der Waals force (MIVW 5.132 kcal·mol^{-1}). The calculated molecular interaction energy values are summarized in Table 10.

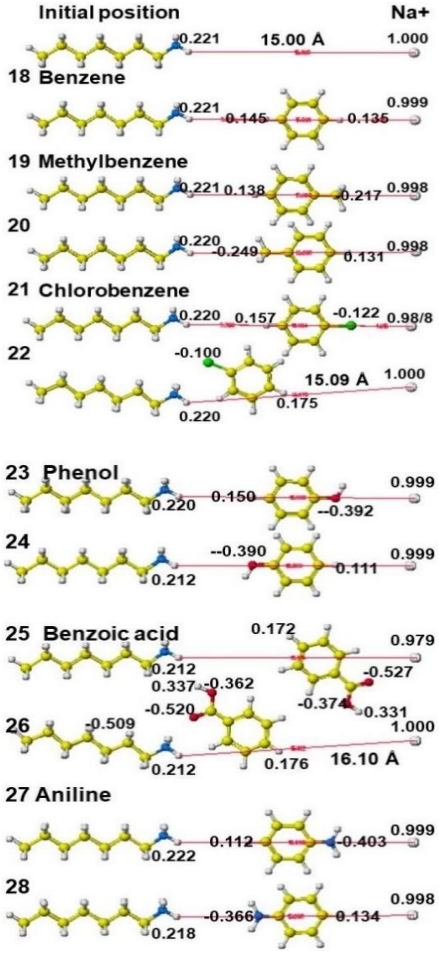

Figure 34.18-34. Contribution of a sodium ion in the ionized amino group and analyte binding

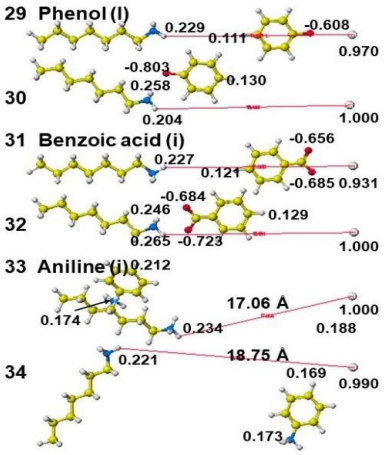

Table 10. Compete for molecular interaction between ionized heptylamine and sodium ion

Molecule	MIHB	MIES	MIVW	Figure
Benzene	0.000	0.000	0.131	34.18
Methylbenzene R	0.000	0.052	0.247	34.19
Methylbenzene L	0.000	-0.044	0.221	34.20
Chlorobenzene R	0.000	0.521	0.252	34.21
Chlorobenzene L	0.000	0.579	1.072	34.22
Phenol R	0.007	-0.087	0.155	34.23
Phenol L	0.06	-0.041	0.155	34.24
Benzoic acid (M) R	-0.024	1.390	0.281	34.25
Benzoic acid (M) L	-0.041	2.580	0.834	34.26
Aniline (M) R	0.001	-0.006	0.169	34.27
Aniline (M) L	0.001	-0.008	0.176	34.28
Phenol (I) R	0.000	3.633	0.101	34.29
Phenol (I) L	0.000	4.618	0.921	34.30
Benzoic acid (I) R	0.000	5.033	0.119	34.31
Benzoic acid (I) L	0.000	7.542	0.426	34.32
Aniline (I) R	0.000	-1.582	5.132	34.33
Aniline (I) L	0.000	-1.394	0.426	34.34

R & L: Substitutes faced toward the amino group and phenyl group faced toward the amino group. M & I: molecular & ionized form analytes; MIHB, MIES, MIVW: molecular interaction energy values of hydrogen bonding, electrostatic interaction, and van der Waals force, unit: kcal·mol^{-1}.

1.4.3 Competition with Na+ for binding with guanidino-group

The competitive sodium ion effect for the molecular Interaction of the guanidino group with these analytes was basically the same as that of the amino group. Benzene, methylbenzene, phenol, and aniline did not contact the guanidino group or the sodium ion. The high electron density chlorobenzene chlorine moved toward the guanidino group; however, the phenyl group contacted the guanidino group via hydrogen bonding (MIHB 4.529 kcal·mol^{-1}). The electron density benzoic acid oxygen contacted the sodium ion via electrostatic Interaction (MIES 1.362 kcal·mol^{-1}). The oxygen apc changed from -0.470 to -0.524 au, and the sodium ion apc changed from 1.000 to 0.976 au (Figure 34.42). In Figure 34.43, the benzoic acid tightly contacted the guanidino group via hydrogen bonding (MIHB 4.622 kcal·mol^{-1}); however, the carbonyl oxygen and hydroxy hydrogen apc changed slightly from -0.470 and 0.374 to -0.462 and 0.371 au. This result indicated that the guanidino group contacted the phenyl group. The MIVW (2.257 kcal·mol^{-1}) supported the interaction site.

The minus-ion phenol oxygen contacted the sodium ion via electrostatic Interaction (MIES 3.497 kcal·mol^{-1}), and the oxygen and sodium ion apc changed from -0.759 and 1.000 to -0.807 and 0.969 au, respectively (Figure 34.46). The ionized oxygen was pulled to the guanidino group and tightly bound via hydrogen bonding and electrostatic Interaction (MIHB 4.734 and MIES 4.111 kcal·mol^{-1}). The oxygen and *p*-hydrogen apc changed from -0.759 and 0.112 to -0.713 and 1.444 au, and the guanidino hydrogen apc changed from 0.295 to 0.346 au. The results indicated that the contact center was the phenyl group. The van der Waals force also contributed to the contact (MIVW 1.195 kcal·mol^{-1}). The ionized benzoic acid carboxy group contacted both sodium ion and the guanidino group (Figures 34.48 and 49), and the primary interaction force was electrostatic Interaction (MIES 4.972 and 5.890 kcal·mol^{-1}). In Figure 34.48, the oxygen and the sodium apc changed from -0.673 and 1.000 to - 0.686 and 0.931 au). The oxygen and the guanidino hydrogen apc changed from -0.673 and 0.295 to -0.715 and 0.356 au. The plus charged amino group repulsed from the sodium ion and contacted the guanidino group via hydrogen bonding (MIHB 4.472 kcal·mol^{-1}) in Figure 34.50, and the amino nitrogen and *p*-hydrogen apc changed from 0.182 and 0.206 to 0.175 and 0.234 au. The plus charged aniline and the guanidino group should not contact via electrostatic Interaction, but hydrogen bonding and van der Waals interaction (MIVW 1.564 kcal·mol^{-1}) were possible interaction mechanisms. The calculated interaction energy values are summarized in Table 11. The sodium ion worked as negatively charged ions. The contribution of a negatively charged chlorine ion was demonstrated in the following experience.

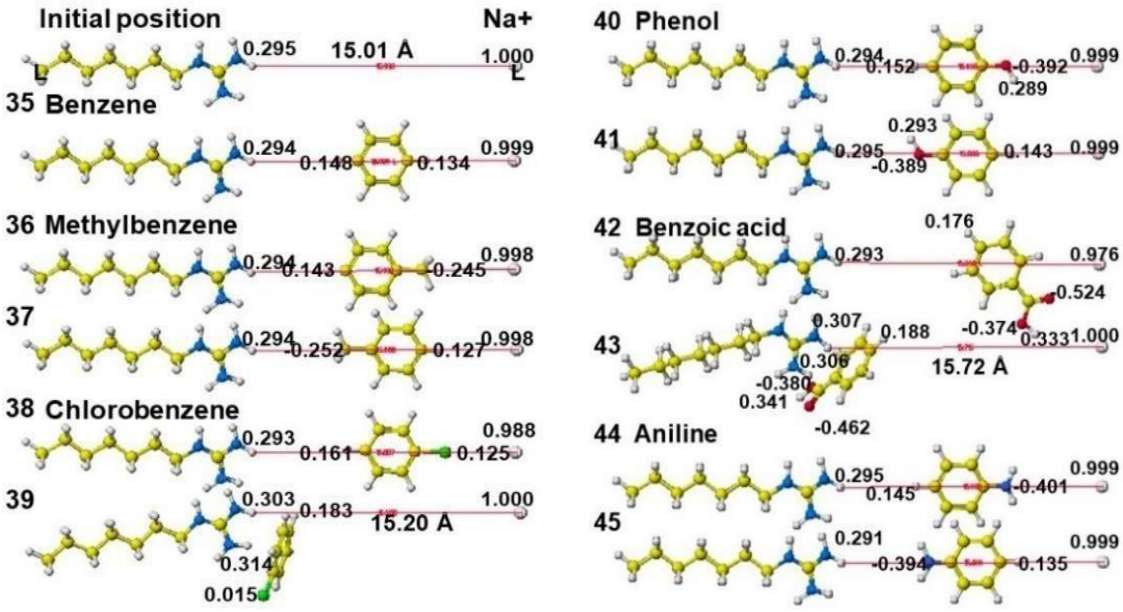

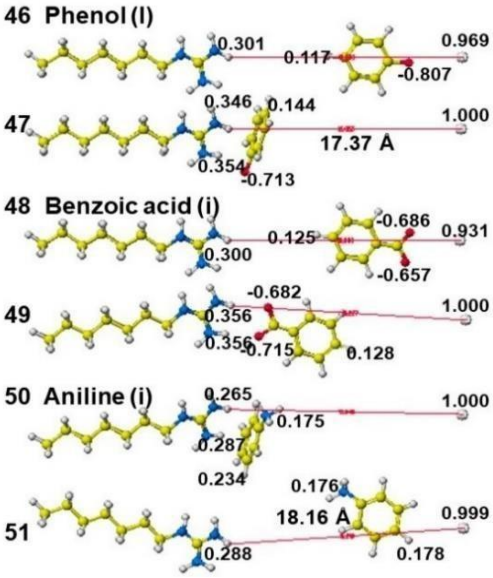

Figure 34.35-51. Contribution of a sodium ion in the guanidino group and analyte binding

Table 11. Compete for molecular interaction between heptylguanidine and sodium ion

Molecule	MIHB	MIES	MIVW	Figure
Benzene	0.014	0.000	0.121	34.35
Methylbenzene R	0.025	-0.057	0.227	34.36
Methylbenzene L	0.009	-0.011	0.234	34.37
Chlorobenzene R	0.011	0.553	0.255	34.38
Chlorobenzene L	4.529	-0.766	1.629	34.39
Phenol R	0.028	-0.090	0.132	34.40
Phenol L	0.033	0.007	0.130	34.41
Benzoic acid (M) R	-0.021	1.362	0.313	34.42
Benzoic acid (M) L	4.622	0.609	2.257	34.43
Aniline (M) R	0.026	-0.002	0.146	34.44
Aniline (M) L	0.016	-0.011	0.155	34.45
Phenol (I) R	0.005	3.497	0.150	34.46
Phenol (I) L	4.734	4.111	1.195	34.47
Benzoic acid (I) R	0.008	4.972	0.131	34.48
Benzoic acid (I) L	0.096	5.890	0.572	34.49
Aniline (I) R	4.472	-2.246	1.564	34.50
Aniline (I) L	0.003	-1.886	0.407	34.51

R & L: Substitutes faced the guanidino group, and the phenyl group faced the guanidino group. M & I: molecular & ionized form analytes; MIHB, MIES, MIVW: molecular interaction energy values of hydrogen bonding, electrostatic interaction, and van der Waals force, unit: kcal·mol^{-1}.

1.4.4 Competition with Cl- for binding with ionized carboxy-group

The sodium ion was replaced with a chlorine ion, and studied the negative charged ion effect for the competitive binding. The chlorine ion was locked. The carboxy group and chlorine-ion induced the electron localization of analytes, but benzene, methylbenzene, and aniline did not bind with either the carboxy group or chlorine ion; even electron localization was induced in their molecules. The electron-rich chlorine was repulsed from the carboxy group (Figure 35.5), and the chlorine and *p*-hydrogen apc changed from -0.051 and 0.163 to -0.095 and 0.204 au. In Figure 35.7, the ionized heptanoic acid oxygen contacted the phenol hydroxy group via electrostatic Interaction (MIES 2.083 kcal·mol^{-1}). The hydroxy oxygen apc changed from -0.386 to -0.428 au (Figure 35.7). Benzoic acid carboxy group contacted the chlorine via weak hydrogen bonding and electrostatic Interaction (MiHB 0.379, MIES 0.974 kcal·mol^{-1}). In Figure 35.9, the benzoic acid carboxy group contacted the heptanoic acid oxygen via electrostatic Interaction (MIES 2.320 kcal·mol^{-1}), and the contact site oxygen apc changed from -0.664 and -0.470 to -0.657 and -0.379 au (Figure 35.9).

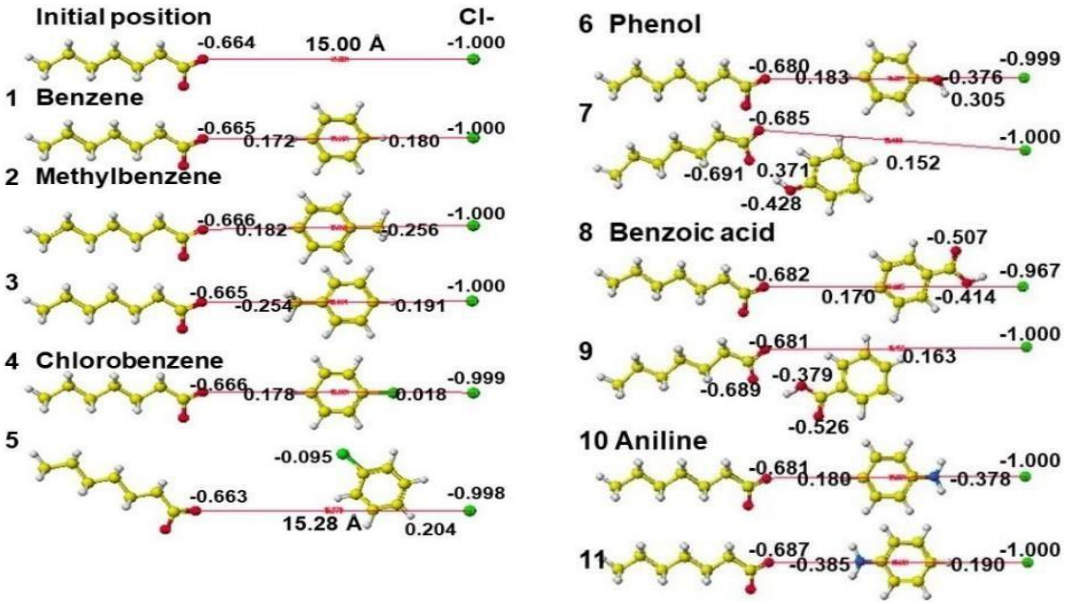

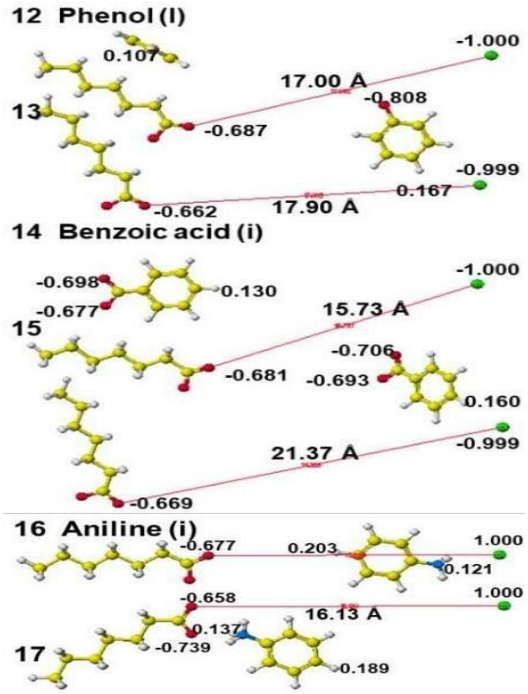

Figure 35.1-17. Contribution of a chlorine ion in the ionized carboxy group and analyte binding

Table 12. Compete for molecular interaction between ionized heptanoic acid and chlorine ion

Molecule	MIHB	MIES	MIVW	Figure
Benzene	0.000	0.000	0.135	35.1
Methylbenzene R	0.000	0.037	0.258	35.2
Methylbenzene L	0.000	0.065	0.254	35.3
Chlorobenzene R	0.000	-0.362	0.345	35.4
Chlorobenzene L	0.000	0.315	0.631	35.5
Phenol R	0.009	0.072	0.155	35.6
Phenol L	-0.002	2.083	0.599	35.7
Benzoic acid (M) R	0.379	0.974	0.227	35.8
Benzoic acid (M) L	-0.181	2.320	0.364	35.9
Aniline (M) R	0.012	0.009	0.157	35.10
Aniline (M) L	-0.001	0.012	0.195	35.11
Phenol (I) R	0.000	-0.981	4.010	35.12
Phenol (I) L	0.000	-1.546	0.579	35.13
Benzoic acid (I) R	0.000	-0.855	2.418	35.14
Benzoic acid (I) L	0.000	-0.934	0.709	35.15
Aniline (I) R	0.000	4.495	0.366	35.16
Aniline (I) L	0.000	8.534	0.136	35.17

R & L: Substitutes faced the carboxy group, and the phenyl group faced the carboxy group. M & I: molecular & ionized form analytes; MIHB, MIES, MIVW: molecular interaction energy values of hydrogen bonding, electrostatic interaction, and van der Waals force, unit: kcal·mol^{-1}

The negatively ionized phenolic oxygen was kicked off the chlorine ion and trapped by the heptanoic acid via van der Waals force (MIVW 4.010 kcal·mol^{-1}) located beside the heptanoic acid alkyl group (Figure 35.12). The ionized phenol was also kicked off from the heptanoic acid (Figure 35.13). The ionized benzoic acid phenomena were the same as that of ionized phenol, and the ionized benzoic acid carboxy group was kicked off from both the chlorine ion and the heptanoic acid (Figures 35.14 and 15), and the heptylcarboxylic acid alkyl group caught the phenyl group (MIVW 2.418 kcal·mol^{-1}) in Figure 35.14. The plus-charged aniline contacted with both the chlorine ion and the heptanoic acid (Figures 35.16 and 17) via electrostatic Interaction (MIES 4.495 and 8.531 kcal·mol^{-1}). The contact center nitrogen pc changed from 0.182 to 0.121 and 0.137 au). The chlorine (Figure 35.16) and the oxygen (Figure 35.17) apc changed from -1.000 and -0.664 to -0.981 and -0.658 au. The calculated molecular interaction energy values are summarized in Table 12.

1.4.2 Competition with Cl⁻ for binding with ionized amino-group

Analytes were located between the plus-charged heptylamine and the negatively charged chlorine to their competitive effect. The clear move of benzene, methylbenzene, and aniline was observed even electron localization was induced. The chlorobenzene chlorine induced contact to the heptylamine via electrostatic Interaction and van der Waals force (MIES 0.716, and MIVW 1.194 kcal·mol^{-1}), and the chlorine apc changed from 0.051 to -0.128 au (Figure 35.22). The phenol hydroxy contacted the chlorine ion *via* electrostatic and van der Waals force (MIES 0.860 and MIVW 0.513 kcal·mol^{-1}). The chlorine ion apc changed from -1.000 to -0.981 au (Figure 35.23). The hydroxyl group was kicked off from the heptylamine (Figure 35.24). The benzoic acid carboxy contacted both chlorine ion and the heptylamine via electrostatic Interaction (MIES 0.878 and 2.734 kcal.mol^{-1}). The hydroxy hydrogen and carbonyl oxygen apc changed from 0.324 and -0.470 to 0.404 and -0.587 au.

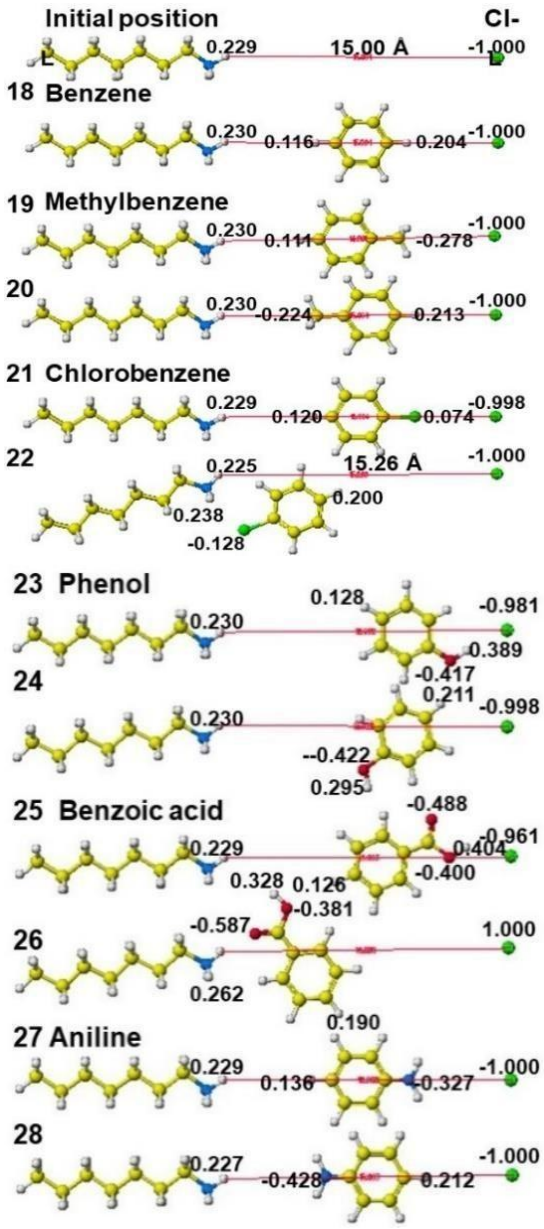

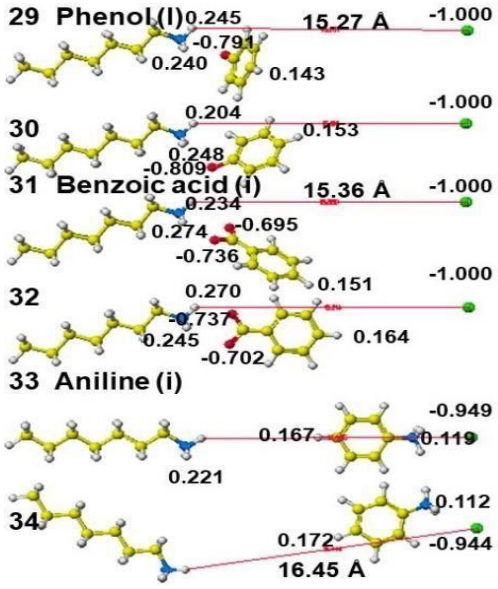

Figure 35.18-34. Contribution of a chlorine ion in the ionized amino group and analyte binding

Table 13. Compete for molecular interaction between ionized heptylamine and chlorine ion

Molecule	MIHB	MIES	MIVW	Figure
Benzene	0.000	0.000	0.126	35.18
Methylbenzene R	0.000	0.115	0.266	35.19
Methylbenzene L	0.000	-0.109	0.230	35.20
Chlorobenzene R	0.000	-0.712	0.336	35.21
Chlorobenzene L	0.000	0.716	1.194	35.22
Phenol R	0.463	0.860	0.513	35.23
Phenol L	0.007	0.034	0.579	35.24
Benzoic acid (M) R	0.366	0.878	0.201	35.25
Benzoic acid (M) L	-0.040	2.734	0.674	35.26
Aniline (M) R	0.011	-0.017	0.143	35.27
Aniline (M) L	0.002	0.018	0.181	35.28
Phenol (I) R	0.000	3.158	1.151	35.29
Phenol (I) L	0.000	3.298	0.994	35.30
Benzoic acid (I) R	0.000	6.447	0.418	35.31
Benzoic acid (I) L	0.000	6.461	0.413	35.32
Aniline (I) R	0.000	3.045	0.295	35.33
Aniline (I) L	0.000	2.943	0.480	35.34

R & L: Substitutes faced toward the amino group and phenyl group faced toward the amino group. M & I: molecular & ionized form analytes; MIHB, MIES, MIVW: molecular interaction energy values of hydrogen bonding, electrostatic interaction, and van der Waals force, unit: kcal·mol^{-1}.

The ionized phenol was kicked off from the chlorine ion and contacted the heptylamine via electrostatic Interaction (MIES 3.158 kcal·mol^{-1}), and the oxygen apc changed from -0.459 to -0.791 au (Figure 35.29). In Figure 35.30, the phenolic oxygen directly contacted the heptylamine via electrostatic Interaction (MIES 3.298 kcal.mol^{-1}), and the apc changed from -0.759 to -0.809 au. The ionized benzoic acid behavior was the same as that of ionized phenol. The carboxy group was kicked off from the chlorine ion and contacted the heptylamine via electrostatic Interaction (MIES 6.447 kcal·mol^{-1}), and the oxygen apc changed from -0.673 to -0.695 and -0.736 au (Figure 35.31). The carboxy directly contacted the heptylamine via electrostatic Interaction (MIES 6.461 kcal·mol^{-1}), and the oxygen apc changed from -0.673 to -0.737 au (Figure 35.32). The ionized aniline directly contacted the chlorine ion via electrostatic Interaction (MIES 3.045 kcal·mol^{-1}), and the nitrogen apc changed from 0.182 to 0.119 au (Figure 35.33). The amino group kicked off the heptylamine and was caught by the chlorine ion via electrostatic Interaction (MIES 2.943 kcal.mol^{-1}, and the nitrogen apc changed from 0.182 to 0.112 au (Figure 35.34). The calculated molecular interaction energy values are summarized in Table 13.

1.4.3 Competition with Cl⁻ for binding with guanidino-group

The heptylguanidine action was similar to that of the heptylamine, and benzene, methylbenzene, phenol, and aniline did not contact either the guanidino group or the chlorine ion, even the electron localization was induced. The electron-rich chlorobenzene chlorine was repulsed from the chlorine ion and trapped by the guanidino group via hydrogen bonding and van der Waals interaction (MIHB 4.694, MIVW 1.545 kcal·mol^{-1}). The chlorine apc changed from 0.051 to -0.012 au (Figure 35.39). The benzoic acid contacted the chlorine ion via electrostatic Interaction and hydrogen bonding (MIES 0.917, MIHB 0.372 kcal·mol^{-1}), and the hydroxy hydrogen and chlorine ion apc changed from 0.324 and -1.000 to 0.403 and -0.962 au (Figure 35.42). However, the benzoic acid carboxy was repulsed from the guanidino group (Figure 43).

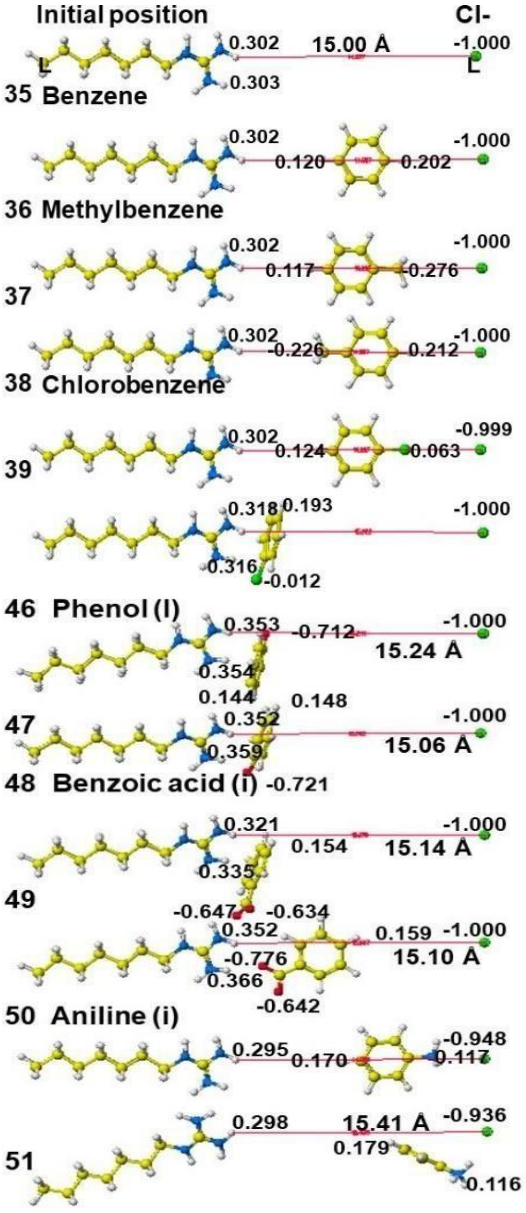

Figure 35.35-51. Contribution of a chlorine ion in the guadinino group and analyte binding

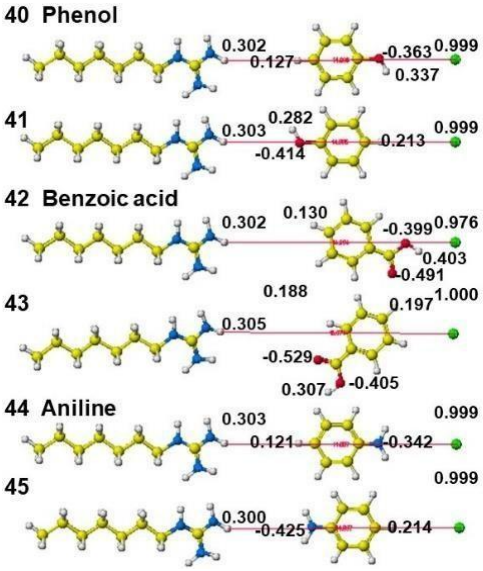

Table 14. Compete for molecular interaction between heptylguanidine and chlorine ion

Molecule	MIHB	MIES	MIVW	Figure
Benzene	0.014	0.000	0.117	35.35
Methylbenzene R	0.025	0.105	0.223	35.36
Methylbenzene L	0.009	-0.084	0.230	35.37
Chlorobenzene R	0.018	-0.628	0.280	35.38
Chlorobenzene L	4.694	-0.290	1.545	35.39
Phenol R	0.028	0.143	0.139	35.40
Phenol L	0.029	-0.056	0.144	35.41
Benzoic acid (M) R	0.372	0.917	0.196	35.42
Benzoic acid (M) L	0.004	0.543	0.487	35.43
Aniline (M) R	0.032	-0.014	0.138	35.44
Aniline (M) L	0.012	0.015	0.189	35.45
Phenol (I) R	4.780	1.808	1.331	35.46
Phenol (I) L	4.737	2.746	1.159	35.47
Benzoic acid (I) R	4.463	0.381	1.643	35.48
Benzoic acid (I) L	0.142	4.919	0.307	35.49
Aniline (I) R	0.005	3.160	0.278	35.50
Aniline (I) L	0.001	2.481	0.592	35.51

R & L: Substitutes faced the guanidino group, and the phenyl group faced the guanidino group. M & I: molecular & ionized form analytes; MIHB, MIES, MIVW: molecular interaction energy values of hydrogen bonding, electrostatic interaction, and van der Waals force, unit: kcal·mol^{-1}.

Ionized phenol oxygen was repulsed from the chlorine ion and caught by the guanidino group via hydrogen bonding, electrostatic Interaction, and van der Waals force (MIHB 4.780, MIES 1.808, and MIVW 1.331 kcal·mol^{-1}). The conformation was observed as their apc change. The phenolic oxygen, *p*-hydrogen, and guanidino hydrogen apc changed from -0.759, 0.112, and 0.302 to -1.712, 0.144, and 0.353 au (Figure 35.46). The phenol directly contacted the guanidino group; however, the electron-rich oxygen contacted the electron-poor hydrogen (MIHB 4.737, MIES 2.746, and MIVW 1.159 kcal·mol^{-1}), and the phenolic oxygen and the guanidine hydrogen apc changed from -0.759 and 0.000 to -0.721 and 0.000 au (Figure 35.47). The behavior of ionized benzoic acid was similar, and the ionized carboxy group was repulsed by the chlorine ion and trapped by the guanidino group (Figure 35.48) via hydrogen bonding and van der Waals force (MIHB 4.463, MIVW 1.643 kcal·mol^{-1}). The carboxy oxygen and the guanidino hydrogen apc changed from -0.673 and 0.000 to -0.647 and 0.000 au, but the *p*-hydrogen and the other guanidino hydrogen apc changed from 0.124 and 0.302 to 0.154 and 0.321 au. The result indicated that the contact center was the phenyl group. The ionized carboxy directly contacted the guanidino group via electrostatic Interaction (MIES 4.919 kcal.mol^{-1}), and the oxygen and the guanidino hydrogen apc changed from -0.673 and 0.000 to -0.776 and 0.000 au (Figure 35.49). The ionized aniline contacted the chlorine ion via electrostatic Interaction (MIES 3.160 kcal.mol^{-1}), and the nitrogen and the chlorine apc changed from 0.182 and -1.000 to 0.117 and -0.948 au (Figure 35.50). The ionized amino group was repulsed by the guanidino group and trapped by the chlorine ion via electrostatic Interaction, and the nitrogen and the chlorine ion apc changed from 0.182 and -1.000 to 0.116 and -0.936 au (Figure 35.51).

The simple model analysis of biologically active ion-exchange groups provided the fundamental action of ion-exchange groups to various substitutes. The ion-exchange groups contacted molecules by combining ion-ion Interaction, hydrogen bonding, and van der Waals force, and these interactions were quantitatively described as electrostatic Interaction, hydrogen bonding, and van der Waals energy values by molecular mechanics calculation. Such fundamental knowledge provided basic approaches in the specific analysis of protein (enzyme) properties

2. Quantitative Analysis of Enzyme Reactions

Quantitative analysis of enzyme reactions allows for the effective design of new drugs and the development of mutants to prepare practical immunoassays. It also reduces animal testing. Molecular engineering approaches for the generation of improved molecules for applications in various industrial, research, and medical settings are in increasing demand. Designing proteins requires fundamental knowledge about the enzyme reaction mechanisms quantitatively. In this context, a quantitative analysis of enzyme reactivity has been developed. Auto docking programs are not satisfactory for this purpose mainly because they recognize only the molecular shape and not the priority of the reaction center. Enzymatic reactions are typically simple chemical reactions in specific chambers where electron transfer can occur under low-energy conditions. One possible approach is the replacement of the original substrate used for obtaining a protein crystal with a new substrate, followed by a quantitative analysis of the novel conformations produced. Quantitative methods for analyzing enzyme reactivity are critical for developing precise diagnostic methods, drug discovery, and reducing the number of tests on animals. Although the specific affinity of an enzyme reaction can be analyzed *in silico*, it is not easy to generalize the selectivity of an enzyme reaction.

In addition, we cannot automatically use the downloaded protein structures from the PDB file, and we have to fix the structure correctly. We have to oversee the downloaded structure and search for strange bonds and amino acids. Basically, amino acid structures are fixed while reconstructing for the exhibition. However, lysine ε-amino group nitrogen shows like sp^2 atom or connects with an unexpected atom. A critical molecule is a coenzyme whose structure is not automatically fixed. The following demonstration describes this evidence and the correction practice.

Proteins soften the stereo structure, collect various substrates, and tighten the complex structure; then, they metabolize the substrates. Or the substrates tighten the complex structure and inhibit the enzyme activity. Such complexing mechanisms are a combination of ion-ion interaction (Coulombic force), hydrogen bonding, and van der Waals force. Furthermore, steric hindrance affects the feasibility. Therefore, the properties of ion-exchange groups were quantitatively analyzed using ion-exchange groups binding alkyl groups to avoid the matrix effect of ion-exchange groups, and the details are described in previous chapters. The fundamental approach was applied for quantitative analysis of enzyme reactivity, such as alanine racemase, serine racemase, alcohol dehydrogenase,

cinnamyl alcohol dehydrogenase, and *D*-amino acid oxidase (DAO), and *D*-aspartic acid oxidase (DDO). The residue arginine was the key amino acid to hold amino acids for these oxidases and racemases.

2.1. Human D-amino acid oxidase (DAO)

D-Amino acids have been found in various tissues; however, *D*-amino acids are not proteinogenic amino acids and are enzymatically oxidized. Improving the analytical method found the importance of *D*-amino acids in maintaining living creatures. In the beginning, the stereo structure of human *D*-amino acid oxidase was not reported; therefore, the stereo structure was constructed from the yeast stereo structure of *D*-amino acid oxidase.

The step-by-step processes for correcting the downloaded protein structures are described in reference 25. Proteins naturally recognize enantiomers. The study of protein recognition of enantiomers was applied to analyze the reactivity of DAO, which selectively oxidizes *D*-amino acids (*D*-AAs). DAO was the second flavoenzyme to be discovered. Krebs first detected DAO activity in tissue specimens in 1935 [26]. This enzyme is present in various organisms, such as bacteria, yeast, fungi, mollusks, insects, fish, amphibians, reptiles, birds, and mammals. Although there is a slight difference in the total number of amino acid residues, the amino acid sequences are highly conserved. The physiologic function has been reviewed [27]. The catalytic activity varies for *D*-AAs. DAO has broad substrate specificity with a preference for *D*-AAs bearing hydrophobic side chains of up to four carbon atoms, followed by those carrying polar and aromatic groups [28]. The physiological role, stereo structure, and reaction mechanism of DAO were reviewed, including the mutants [29].

Many crystallographic structures of DAO are readily available from the Protein Data Bank [30]. The substrates of the DAO complexes were varied. The substrates were replaced with an amino acid. The conformation of the DAO-amino acid complex was then optimized using MM2 calculations to analyze which amino acid residue of DAO was directly involved in the binding, based on various atomic distances and electron transfer determined from the atomic apc of neighboring atoms. Furthermore, the stereo structure of human DAO was estimated from the sequence data NP001908 [31], and the stereo structure of pig kidney DAO 1VE9 [30] because of the similarity of these sequences; and the selectivity of the estimated human DAO was analyzed. The selectivity of DAO mutants was also analyzed after docking with various amino acids [32-34].

Downloaded DAO 3cuk is shown in Figure 36. The down-loaded structure indicates that it is not a single set of an enzyme, and picking up one enzyme, is shown in Figure 37 with a long bald bond. The modified bond indicates the existence of an unrealistic structure in the downloaded structure. The bond is a missing peptide of S57, D58, P59, N60, and N61. Further analysis of the structure based on the amino acid sequence indicates the lack of eight amino acids P297, T198, G299, P300, S301, K337, and S340. These amino acids are far from the reaction chamber and may not affect the reactivity; however, they may affect the enzyme' steric hindrance to collecting a substrate. The correction may be completed by cutting irregular bonds, but adding amino acid may be required.

The downloaded human *D*-amino acid dehydrogenase (2e49) consists of a tetramer holding 3-hydroxy-2-iminopropanoic acid to make the crystal, as shown in Figure 38. After removing water molecules, the monomer is optimized, as shown in Figure 39, where the location of 3-hydroxy-2-iminopropanic acid and coenzyme FAD are indicated. However, the structures of FAD and substrate 3-hydroxy-2-iminopropanoic acid structures are not acceptable. The 3-hydroxy-2-iminopropanoic acid carboxy group connects with the arginine (R283) guanidyl group via ion-ion Interaction. However, the *D*-amino acid oxidation location is the same.

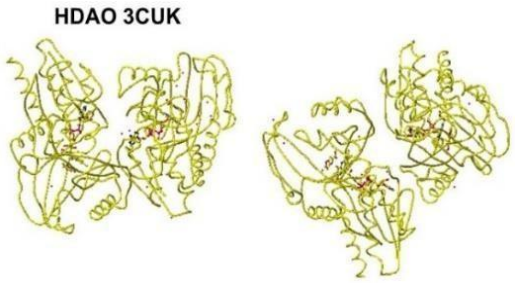

Figure 36. Downloaded HDAO 3cuk

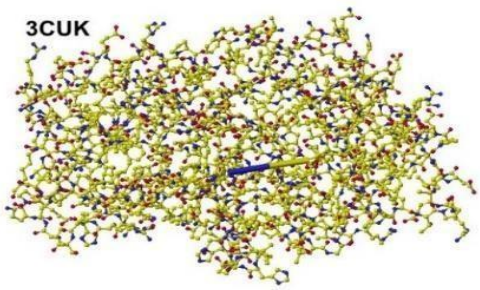

Figure 37. Single structure of 3cuk

Another HDAO uses a high-mass 3-hydroxyquinoline-2(1H)-one to make the crystal (3g3e). Comparison of the additional molecule mass demonstrates the different number of regional amino acids: Figures 40 and 41 exhibit the extracted conformations of 3g3e and 2e49, respectively. The number of molecules within 3Å from high mass 3-hydroxyquinoline-2(1H)-one is eight, and those within 3Å from low mass 3-hydroxy-2-iminopropanoic acid are only four. The structure of 3g3e is highly dense, and that of 2e49 has selective space. These Figures indicate that structures of coenzyme and the crystallization contributed molecule are not precisely exhibited.

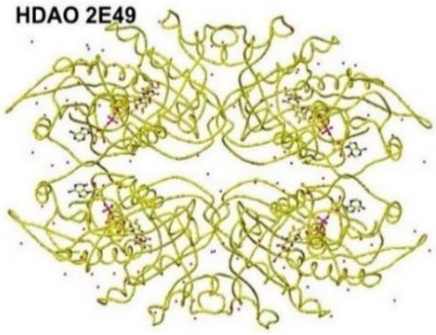

Figure 38. Downloaded HDAO 2e49

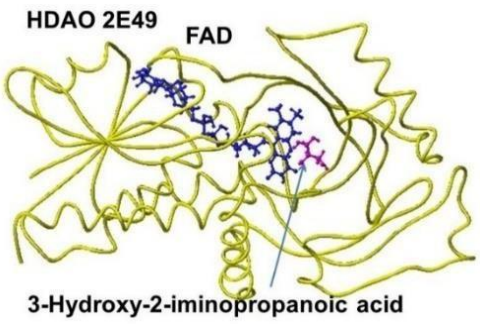

Figure 39. optimized HDAO 2e49

Figure 40. Downloaded and extracted 3g3e

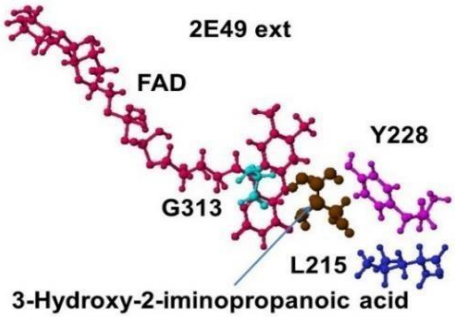

Figure 41. Downloaded and extracted 2e49

The extracted coenzyme FAD from 2e49 is shown in Figure 42, where the original and corrected FAD structures are shown. The circle parts are not the right structure; therefore, these structures are corrected, and the entire structure is optimized. The extracted molecules within 3Å from 3-hydroxy-2-iminopropanoic acid are shown in Figure 41. The total number of molecules increases from four to seven.

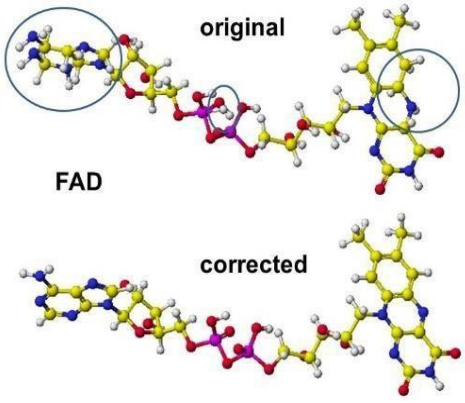

Figure 42. Correction of coenzyme structure

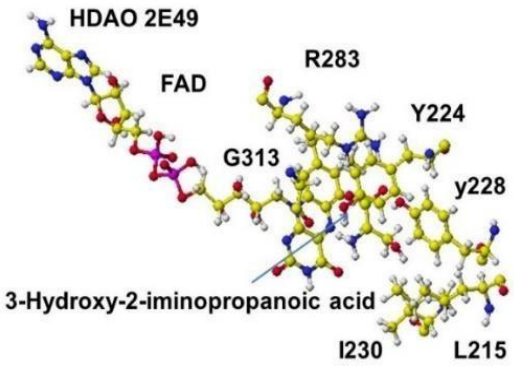

Figure 43. Extracted molecules from the corrected 2e49

Citation: Toshihiko Hanai. Quantitative In Silico Analytical Chemistry for Drug Discovery: From Ion-Ion Interaction to Covid-19 Variants Transmissibility and the Binding Inhibitors. Journal of Analytical Techniques and Research. 8 (2026): 38-109.

The 3-hydroxy-2-iminopropanoic acid is replaced with *D*-alanine, and the complex is optimized after superimposing their carboxy groups. Figure 44 shows the optimized structure of the *D*-alanine complex, and Figure 45 shows the extracted molecules within 3Å from *D*-alanine.

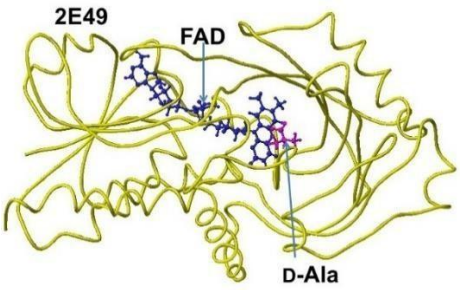

Figure 44. D-Alanine complex with 2e49

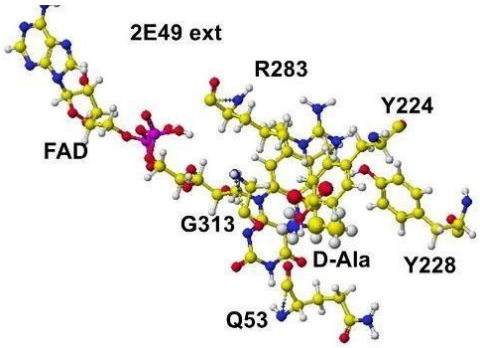

Figure 45. Extracted molecules within 3Å from *D*-alanine

When a stereo structure of a human enzyme is unreported, the stereo structure must construct from a known structure and human sequences; when the yeast protein structure is used, it does not directly construct human protein structure and uses a relatively near mammalian structure as an intermediate. It is unnecessary to replace many amino acids and keep the stereo structure without a large deformation in this process. The similarity of yeast and pig residual amino acids is 26 and 85%, respectively, to human residual amino acids, and the analogy of pig and human amino acids is 90%.

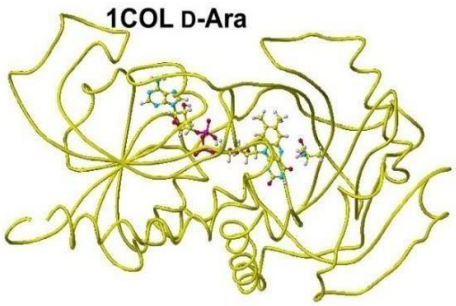

Figure 46. Yeast *D*-amino acid oxidase

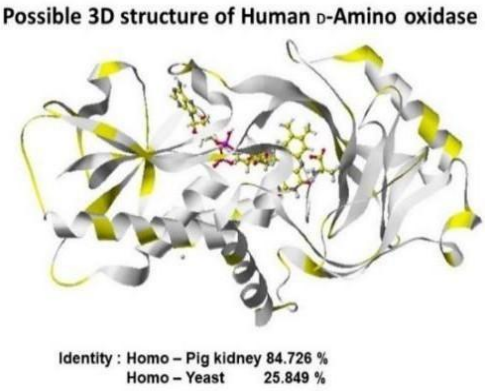

Figure 47. Constructed human *D*-amino acid oxidase

The difference between yeast *D*-amino acid oxidase and the constructed human *D*-amino acid oxidase from yeast *D*-amino acid oxidase is the visuality of the coenzyme FAD. FAD is hidden in human *D*-amino acid oxidase and quite visual in yeast *D*-amino acid oxidase. The visuality may support the high selectivity of human *D*-amino acid oxidase, and yeast *D*-amino acid oxidase easily collects various *D*-amino acids oxidizes.

There is no guarantee that an auto-docking program correctly replaces substrates. The simple method is superimposing these carboxy groups to face the arginine guanidyl group and replacing them. Extract molecules within 3Å from the amino acid after optimizing the whole structure. Then, the extracted complex is locked and optimized using MOPAC-PM5 (or the latest) to obtain atomic partial charge values. This approach is an advanced method of studying chromatographic retention mechanisms.

This enzyme reaction is the oxidation of amino acid amino group and changes a keto acid; therefore, the key atoms are the substrate amino acid α-carbon, amino group nitrogen, and flavine ring carbonyl group. The yeast *D*-amino acid oxidase 1cop mutant M215R reactivity ($\log k_{cat}/K_m$) was related to α-carbon and nitrogen apc with $r = 0.964$ (n = 7). The substrate amino acids are *D*-asparagine, *D*-glutamic acid, *D*-alanine, NMDA, *D*-glutamine, *D*-aspartic acid, and methionine.

Citation: Toshihiko Hanai. Quantitative In Silico Analytical Chemistry for Drug Discovery: From Ion-Ion Interaction to Covid-19 Variants Transmissibility and the Binding Inhibitors. Journal of Analytical Techniques and Research. 8 (2026): 38-109.

The calculated 14 *D*-amino acids α-carbon apc of human DAO (HDAO) constructed from pig DAO (1ve7) and HDAO (3znn, 3g3e, 2du8) was correlated with the enzyme reactivity (U mg^{-1} protein) with greater than r = 0.8. Even if no actual stereo structure exists, the constructed stereo structure using a stereo structure of different spacy and amino acid sequence supports further analysis of enzyme specificity. The substrate amino acids are *D*-asparagine, *D*-glutamine, *D*-alanine, *D*-phenylalanine, *D*-methionine, *D*-valine, *D*-leucine, *D*-serine, *D*-threonine, *D*-tryptophan, *D*-cysteine, *D*-arginine, *D*-lysine, and *D*-histidine.

When a sheep DAO is necessary, the stereo structure can be driven from pig DAO. The calculated pig DAO and sheep DAO α-carbon apc corrected to their relative oxidation reactivity with r = 0.92 (n = 7) and 0.83 (n = 7), respectively. The substrate amino acids are *D*-alanine, *D*-serine, glycine, *D*-aspartic acid, *N*-methyl-*D*-aspartic acid, *D*-glutamic acid, and γ-butyric acid.

Further analysis was performed on the selective inhibition of kojic acid that inhibited amino acid oxidation. The inhibition can be explained by the electron localization of the oxygen contacting the R283 guanidyl group. The inhibition ratio (%) and these Δapc values were correlated with r = 0.98 (n = 4). The selective enzyme reactivity can be quantitatively analyzed based on the apc of the reaction center atoms obtained by forming a complex inside the enzyme stereo structure.

2.2. Human acidic D-amino acid oxidase DDO

The oxidation reactivity of DAO was quantitatively analyzed *in silico* [32-34] because D-amino acids exist in mammal tissues, especially in the brain [35-37]. DAO is the catabolic enzyme that stereo specifically acts on several neutral and basic D-amino acids (but not on acidic *D*-amino acids), including free *D*-serine [38]. *D*-Serine plays an essential role in regulating brain function by acting as an endogenous ligand for the *N*-methyl-*D*-aspartate (NMDA) receptor (a subtype of the *L*-glutamate receptor family) and a δ2 glutamate receptor [39-41]. Besides *D*-serine, free *D*-aspartic acid has also been studied extensively. Unlike the tissue (brain)-specific expression of *D*-serine, substantial amounts of *D*-aspartic acid are present in a wide variety of tissues and cells in mammals, particularly those that make up the central nervous, neuroendocrine, and endocrine systems. Several lines of evidence suggest that *D*-aspartic acid plays an important role in regulating developmental processes, hormone secretion, and steroidogenesis [42,43]. Acidic *D*-amino acids, such as *D*-aspartic acid, *D*-glutamic acid, and NMDA, are degraded by another *D*-amino acid-specific enzyme, *D*-aspartate oxidase (DDO). DAO and DDO are flavin adenine dinucleotides (FAD)-containing flavoproteins that catalyze the oxidative deamination of D-amino acids to generate 2-oxo acids along with hydrogen peroxide and ammonia. The mammalian DAO and DDO are presumed to regulate the levels of several endogenous and exogenous *D*-amino acids, including *D*-serine and D-aspartic acid, in various organs [38,44]; however, their physiological roles *in vivo* remain to be fully clarified.

The three-dimensional (3D) structures of mammalian and yeast DAOs have been determined [21-25]. These studies revealed that the driving force of molecular interactions is the Coulombic force between an active site residue arginine's guanidyl group of DAO and a carboxyl group of the substrate amino acid. A mutant, M213R of yeast DAO (PDB ID: 1C0P) [18], was prepared to analyze the freshness of food [26]. The stereo structure of sheep DAO was constructed from pig DAO (PDB ID: 1VE9); even the amino acid sequence of sheep DAO differs from that of 1VE9 by 8.5% to analyze the inhibition of the oxidation [27]. The structure of the docked complex of an enzyme, FAD, and a substrate was attempted to be optimized using the molecular mechanics 2 (MM2) calculation of the CAChe™ program. The tightness of the complex was determined as the energy value difference; however, the molecular interaction energy values were not quantitatively related to the enzyme reactivity. The tightness, but not the reactivity, was affected by the molecular size. Further calculation of the apc using MOPAC-PM5 of the CAChe™ program indicated the feasibility of the chemical reactions [32-34].

Previously, the role of Ser-308 in mouse DDO was investigated using site-specific mutational analysis of this residue [52]. Here, alanine-, glycine-, and tyrosine-substitution mutants (S308A, S308G, and S308Y mutants, respectively) were prepared, and their enzyme properties were characterized [52]. The stereo structures of these mutants, in addition to a double-point mutant of mouse DDO (S308G-G309Y mutant), were constructed *in silico* and optimized using the MM2 calculation (shown in Figure 36). Furthermore, apc of key atoms was calculated using a MOPAC-PM5 program, and then the reactivity of these mouse DDO mutants was analyzed [53,54].

Acidic *D*-amino acids, such as *D*-aspartic acid, *D*-glutamic acid, and NMDA, are degraded by another *D*-amino acid-specific enzyme, DDO. DDO is also flavin adenine dinucleotide (FAD)-containing flavoproteins that catalyze the oxidative deamination of *D*-amino acids to generate 2-oxo acids along with hydrogen peroxide and ammonia. DDO selectively oxidizes acidic amino acids, and three guanidyl groups exist nearby FAD to trap an acidic *D*-amino acid via ion-ion Interaction with the two carboxy groups.

Mouse DDO (MDDO) is constructed from pig DAO (PDB 1k1f) and MDDO amino acid sequencer (NCGI: NM 027442.5) to study the MDDO specificity. The similarity and analogy are 43 and 56%, respectively. The constructed human DDO (HDDO), rat DDO (RDDO), cow DDO (CDDO), and mouse DDO (MDDO) are held *D*-aspartic acid as the substrate; then, these complexes are optimized. These structures are shown in Figure 48. The reaction selectivity can be imagined from their openness to catch various *D*-amino acids. The most selective HDDO exhibits a little FAD and *D*-aspartic acid, and the least selective MDDO exhibits a wide openness for trapping substrates.

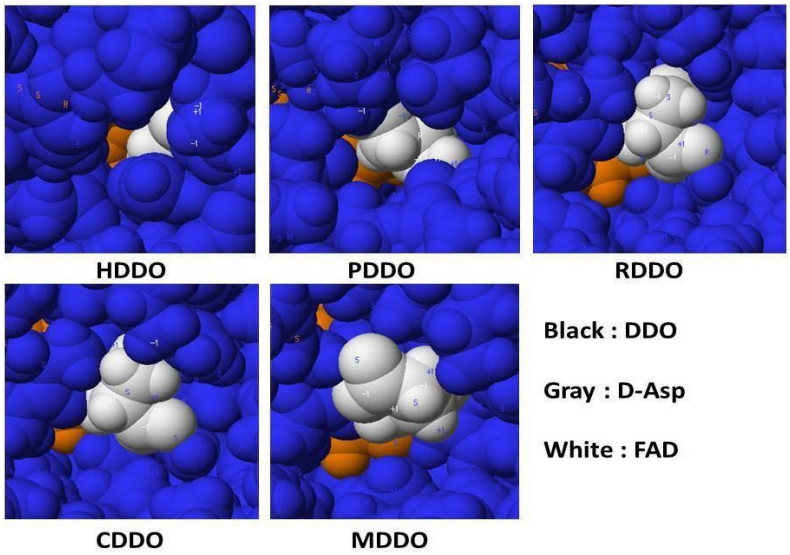

Figure 48. Optimized structures of HDDO, PDDO, RDDO, CDDO, and MDDO with FAD and *D*-aspartic acid

Figures 49 and 50 show the conformation of PDDO and MDDO. These conformations demonstrate the feasibility of their modified stereo structures where the fundamental structures of their reaction sites are very identical.

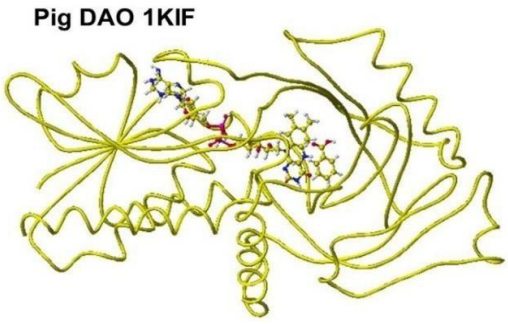

Figure 49. Original PDAO structure

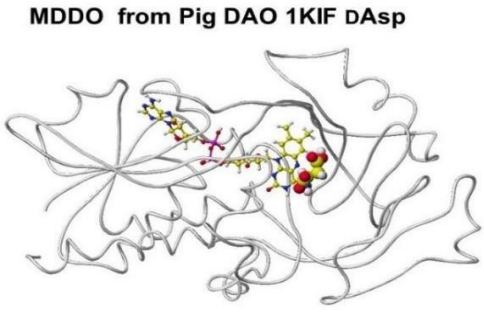

Figure 50. Constructed MDDO from PDAO

Five mutants of MDDO (S308A, S308Gn S308D (wild), S308G-G309Y, S308Y) are constructed, and their reactivity with *D*-aspartic acid and NMDA are analyzed. Their correlation between α-carbon apc and their reactivity (V_{max}/V_m) is 0.85 (n = 5) and 0.90 (n = 5), respectively.

Citation: Toshihiko Hanai. Quantitative In Silico Analytical Chemistry for Drug Discovery: From Ion-Ion Interaction to Covid-19 Variants Transmissibility and the Binding Inhibitors. Journal of Analytical Techniques and Research. 8 (2026): 38-109.

The higher reactivity of S308G than S308Y depends on the steric hindrance, and a larger residual amino acid inhibits the contact of aspartic acid with the FAD ring. The mutation of S308 affects the contact tightness of *D*-aspartic acid with the FAD ring. Figures 51 and 52 visually demonstrate the tyrosine's conformation covering the FAD ring and inhibiting *D*-aspartic acid contact.

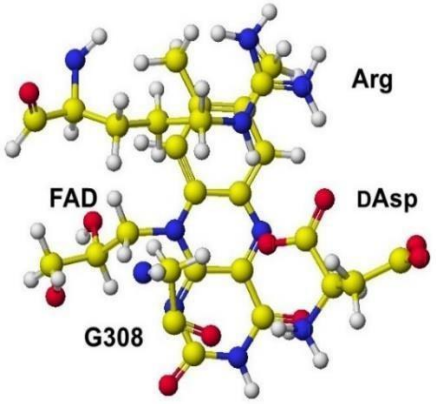

Figure 51. Location of MDDO S308G

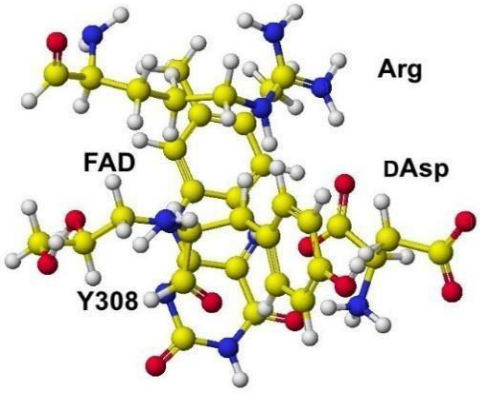

Figure 52. Location of MDDO S308Y

HDDO PDF: 6rkf is downloaded to study HDDO specificity. The downloaded 6rfc is a hexamer, as shown in Figure 53. The single complex structure contains the substrate (2-amino-2-hydroxymethyl-propane-1,3-diol), and three arginines exist within 3Å from the substrate. After replacing the substrate with D-aspartic acid, the complex is reoptimized, and the optimized structure, including *D*-aspartic acid, is shown in Figure 54. The peptide Y141 - G143 is different from the sequencer data (C143 – C141) of UniProtKB-Q99489(OXDD_HUMAN). However, the 6rkf structure is used for further analysis of HDDO. In addition, the constructed MDDO and RDDO from 6rkf do not show any irregularity. Figure 55 shows HDDO constructed from PDDO with *D*-aspartic acid.

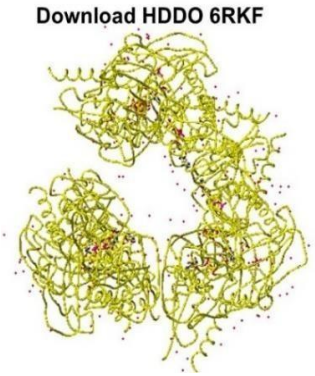

Figure 53. Downloaded HDDO

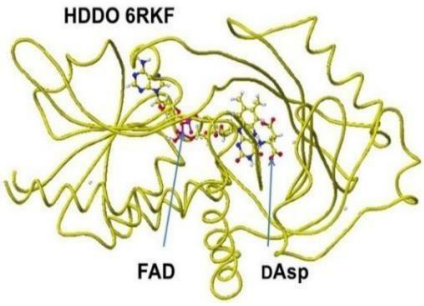

Figure 54. Optimized 6rkf with *D*-aspartic acid

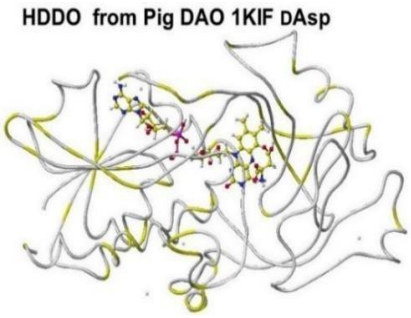

Figure 55. HDDO from PDDO 6ekf

The molecules within 3Å from *D*-aspartic acid are shown in Figure 56. The contact atoms with *D*-aspartic acid are shown in Figure 57, where two guanidyl groups, R237 and R278, contact with *D*-aspartic acid β-carboxy groups via ion-ion interaction, and R216 guanidyl group contacts with *D*-aspartic acid α-carboxy group via ion-ion Interaction. The multi-ion-ion interactions of DDO differ from DAO, which forms only one ion-ion Interaction.

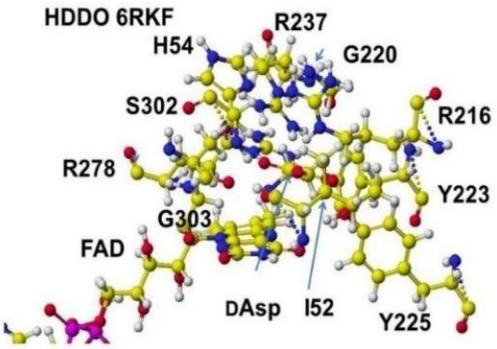

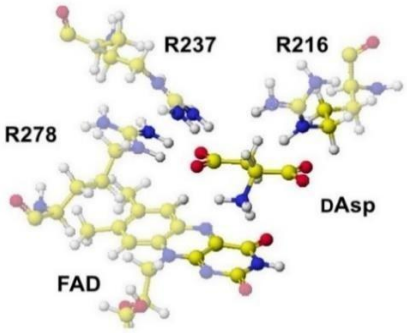

Figure 56. Molecules within 3Å from *D*-aspartic acid

Figure 57. Contact atoms with *D*-aspartic acid

Red (black), blue (dark gray), yellow (light gray), white, and magenta: oxygen, nitrogen, carbon, hydrogen, phosphorous

RDDO is constructed by replacing amino acids of 6rkf for studying species specificity, and the structure is shown in Figure 58. Figure 59 shows RDDO constructed from PDDO. Both structures are very similar.

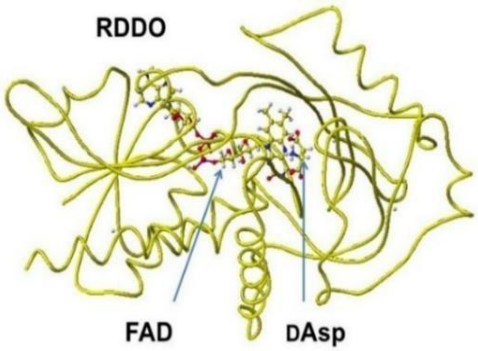

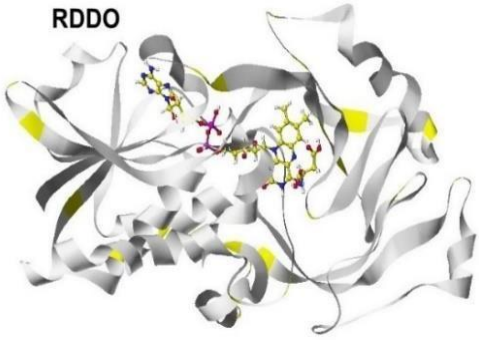

Figure 58. RDDO structure from 6rkf

Figure 59. RDDO structure from PDAO

Figure 60 shows molecules within 3Å from *D*-aspartic acid, and Figure 14 shows contact atoms with *D*-aspartic acid. The protein arginine R237 and R278 contact with β-carboxy group, and R218 contact with α-carboxy group of *D*-aspartic acid, like contact the conformation of HDDO.

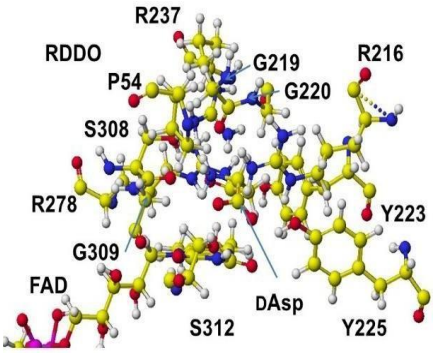

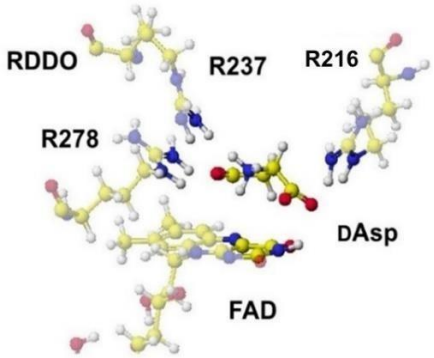

Figure 60. Molecules within 3Å from *D*-aspartic acid

Figure 61. Contact atoms with *D*-aspartic acid

In addition, MDDO is constructed by replacing amino acids of 6rkf for studying species specificity, and the structure is shown in Figure 62. Figure 63 shows MDDO constructed from PDDO.

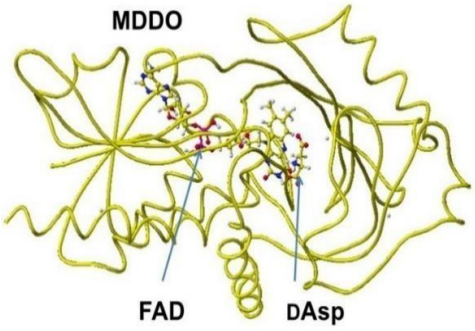

Figure 62. MDDO structure from 6rkf

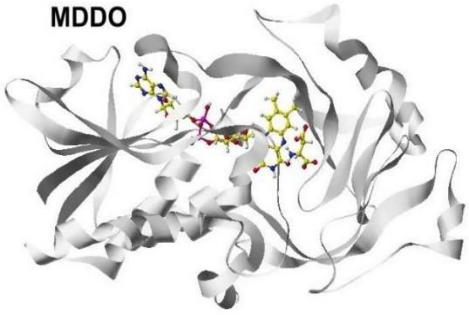

Figure 63. MDDO structure from PDAO

Figure 64 shows molecules within 3Å from *D*-aspartic acid, and Figure 65 shows contact atoms with *D*-aspartic acid. The protein arginine R218, R237, and R278 contact with β-carboxy group and FAD contacts with α-carboxy group of *D*-aspartic acid. These three DDO structures looked similar, but the conformation of these reaction centers is a little different. A minor difference in residual amino acids affects the location of arginine and produces their electron localization degree.

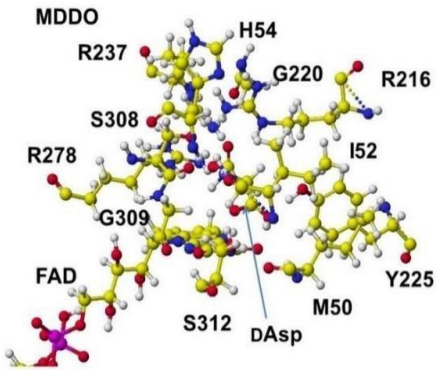

Figure 64. Molecules within 3Å from *D*-aspartic acid

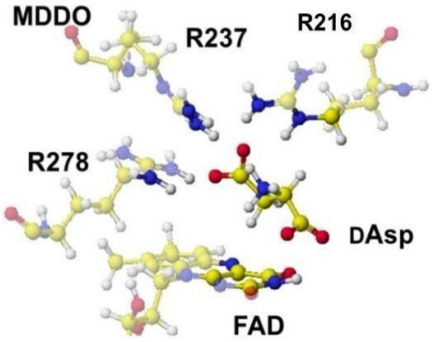

Figure 65. Contact atoms with *D*-aspartic acid

Quantitative analysis of enzyme reactivity can be performed by replacing the substrates, and even the stereo structure is unknown. The necessary stereo structure can be constructed from a known stereo structure and the target compound's amino acid sequencer datum. The stereo structures constructed from other species are similar, but there is no guarantee whether the newly constructed structures reflect the species' actions or not.

One selection difficulty is the definition of secondary structure indications between right-handed alpha (H) and 310 helices (G), which are defined for the same spiral peptides. For example, the last spiral peptide of HDDO consisting of 16 amino acids (W315 – H330) is shown using the right-handed alpha and 310 helix definition in Figure 66. The threads form structures that indicate a tight and soft tube.

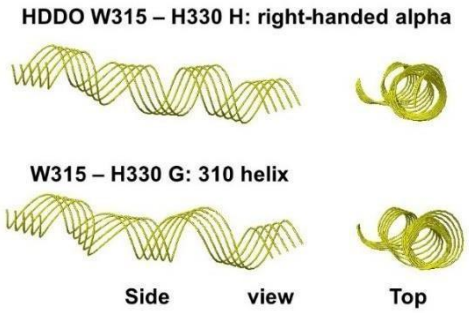

Figure 66. Different spiral structures are defined by different secondary structures

The secondary structure definitions are not identical for similar amino acid locations in the actual amino acid sequences. The residual amino acid difference produces a slight difference in stereo structure due to the steric hindrance. The flexibility of holding a substrate is not clear from the crystal structures.

The comparison of HDAO 3ch8 from 2e49 and 2du8 clarifies the lack of five amino acids (S57 – N61) and six amino acids (R296 – S301) in 3ch8. The secondary structure of T43 – A48 is 310 helix and right-handed alpha for 2e49 and 2du8. That of W185 – Q190 is a right-handed alpha, and that A186 – Q190 of 2e49 is 310 helix, and G183 – L186 of 2du8 is 310 helix, D218 – G222 of 2e49 is 310 helix, but no secondary structure is for 2du8 and 3cuk. In addition, several amino acids are different under the same secondary indication, and these different secondary structures should affect the reaction selectivity.

The molecular mass of compounds used for crystallization also affects the steric conformation of enzymes. The comparison of the amino acid sequencer of 6rkf, HDAO 4qfc holds 4-hydroxy-6-[2-(7-hydroxy-2-phenyl-2H-chromene-6-yl)ethyl]pyridazine-3(2H)-one lacks many amino acids: S25 – P29, D58 – P62, L296 – T303, D2, T3, A4, T55, T59, I61, T63, P102, V106, Q287, T288, L290, L291, A292, C328, H330, and A335. The two missing peptides are shown as bold bonds in Figure 67. Molecules within 3Å from this large mass compound are shown in Figure 68. HDAO 4qfc cannot be used to construct an HDDO.

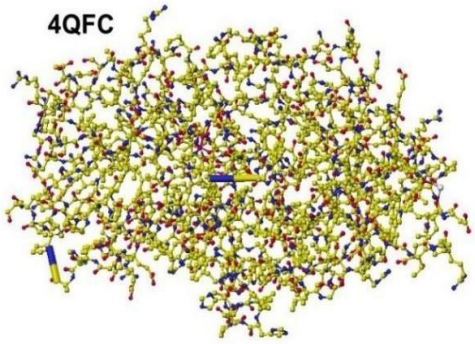

Figure 67. Stereo structure of HDAO 4qfc

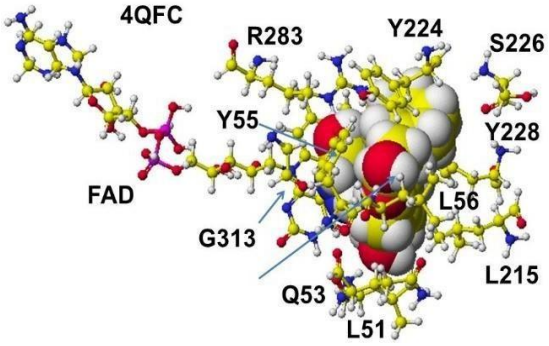

Figure 68. Molecules within 3Å from the compound

Another similar structure, 4qfd, holds 3-(7-hydroxy-2-oxo-4-phenyl-2H-chromene-5-yl)propanoic acid also lacks many amino acids, such as L56 – P62, H24 – L30, and others. Whether such large mass compounds are naturally held in the enzyme is not clear. 4qfc and 4fd are prepared from the same enzyme, but their secondary structures are not identical. Therefore, we must carefully evaluate the downloaded stereo structure by comparing the amino acid sequence data.

2.3. Alcohol Ddehydrogenase

Alcohol dehydrogenase (ADH) belongs to the oxidoreductase family, a class of enzymes responsible for the catalysis of biological oxidation and reduction reactions. ADH catalyzes the inter-conversion between alcohols and the corresponding aldehydes or ketones using NADH as a coenzyme. A protein fluorescence quenching study ruled out the necessity of product dissociation [56]. The proton release preceded NAD^+ reduction at neutral pH value. After ternary-complex formation, the catalytic step results in forming the enzyme-NADH-aldehyde complex. The zinc ions, considered to be involved in the catalysis, have not been elucidated; however, a likely role for the zinc ions would be to increase the acidity of the alcohol hydroxyl group, thus facilitating hydride transfer by a related mechanism [57-59]. The stoichiometry of the oxidation reaction has suggested the release of one proton from the alcohol. Further, no free radical reduction was observed involving the carbon-hydrogen bond cleavage, which was probed using halo ketones to test for the involvement of a radical intermediate in the NADH/liver alcohol dehydrogenase reduction reaction. A three steps reaction mechanism was considered rather than a direct release mechanism [60].

The alcohol molecule binds to the zinc ion through the oxygen atom, and this inner sphere binding induces the ionization of the alcohol to the alkoxide form. The formation of a zinc-bound alkoxide ion is necessary to form

the closed conformation of the LADH ternary complex prior to the hydride transfer. The lower the p*K*a value of alcohol, the greater the inductive effect on the hydride-donor carbon atom. For alcohols with electron-donating substituents at the C2 atom, the ionization would occur with a relatively higher p*K*a value, and the hydride transfer would therefore occur more quickly [61]. The catalytic efficiency of the amphibian alcohol dehydrogenase enzyme ADH8, which is the vertebrate ADH with coenzyme NADPH, is greater for the medium- or long-chained substrates such as hexanal, *trans*-2-hexanal, and several retinoid isomers, in corresponding alcohols or retinols [62]. The comparison of three-dimensional (3D) structures suggested that a zinc ion may mediate the displacement of the zinc-bound water molecule with an alcohol or an aldehyde molecule, and the water was not assigned any catalytic role [63]. The possible electron transfer can be determined by the electron localization of the targeted atoms and by the location of the alcohol hydroxyl group. The detailed crystal structure of the cinnamyl ADH from *Saccharomyces cerevisiae* has been determined [64]. Further, the crystal structure of the ternary complex of the slow-allele form of *Drosophila melanogaster* ADH with NADH and acetate has also been determined [65]. The stereo structure of the *Drosophila melanogaster* ADH-S and a theoretically built homology model for the enzyme were compared. Moreover, the differences in the crystal structures of five available *Drosophila lebanonensis* ADHs in multiple complex forms were evaluated, residue conservation at the active site was examined, and the metagenesis data available for the enzymes were interpreted [66].

Quantitative analysis of an enzyme activity allows for the design of mutants required to develop practical immunoassay methods, enzymatic biosensors, engineered enzymes, and new drugs. The basic phenomenon of molecular recognition by proteins has been studied based on quantitative analysis of molecular interactions using chromatography. Alcohol dehydrogenase (ADH) belongs to the oxidoreductase family, a class of enzymes responsible for the catalysis of biological oxidation and reduction reactions. ADH catalyzes the inter-conversion between alcohols and the corresponding aldehydes or ketones using NADH as a coenzyme. Two types of ADHs exist, one is zinc-dependent, and another is zinc-independent. They require coenzyme NAD (Nicotinamide-8-iodo-adenine-dinucleotide); therefore, the reaction selectivity is an interesting subject. Drosophila melanogaster's H is zinc independent; the downloaded crystal structure (PDB 1MG5) is shown in Figure 69.

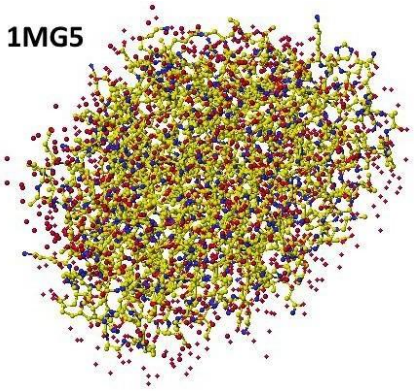

Figure 69. Download PDB 1MG5 structure

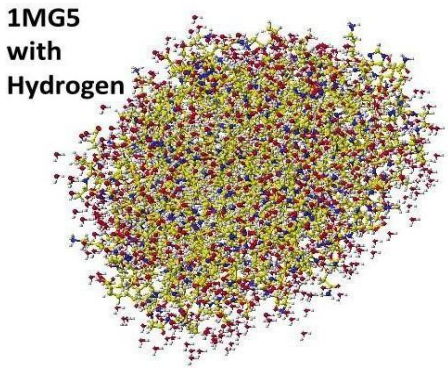

Figure 70. Addition of hydrogen using Valence

Red (black), blue (dark gray), yellow (light gray), and white are oxygen, nitrogen, carbon, and hydrogen.

The structure in Figure 69 is not clear the ADH conformation; therefore, the addition of hydrogen to water molecule oxygen using Valence was achieved. The result produced Figure 70 structure. Selected water in the menu and erased water, making clear the ADH structure, are shown in Figure 71. The original file appears as a dimer, as shown in Figure 72. The rotating structures are shown in Figure 73 to demonstrate their clear images. Figure 74 shows the location of coenzyme NAD and the substitute aldehyde. The structures of NAD and aldehyde are not as their actual structures. Generally, we have to doubt the downloaded coenzyme and substitute structures.

Citation: Toshihiko Hanai. Quantitative In Silico Analytical Chemistry for Drug Discovery: From Ion-Ion Interaction to Covid-19 Variants Transmissibility and the Binding Inhibitors. Journal of Analytical Techniques and Research. 8 (2026): 38-109.

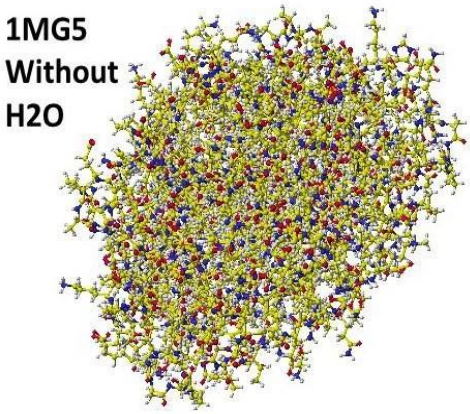

Figure 71. 1MG5 removed the water molecules

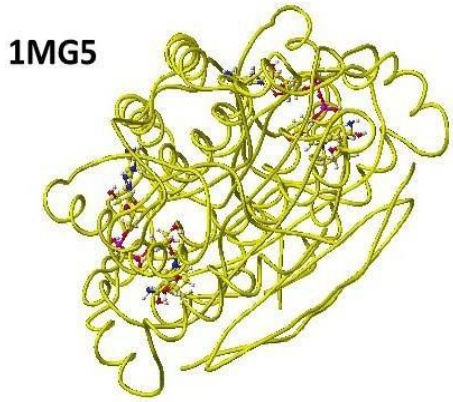

Figure 72. Single thread structure

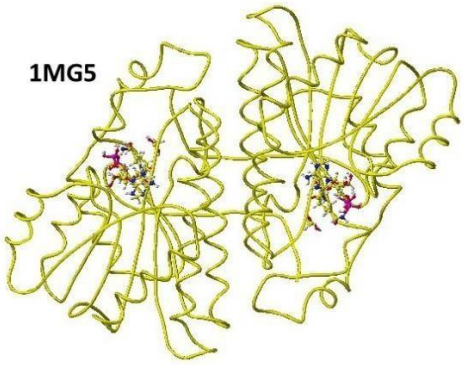

Figure 73. Location of two sets of molecules

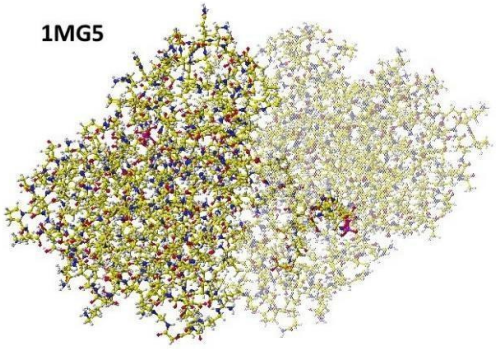

Figure 74. An original molecular view of Figure 73

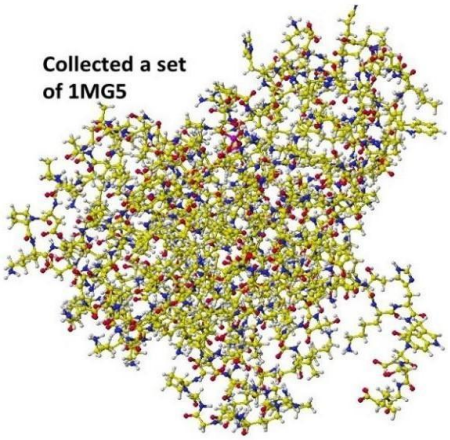

Figure 75. Extracted one ADH complex

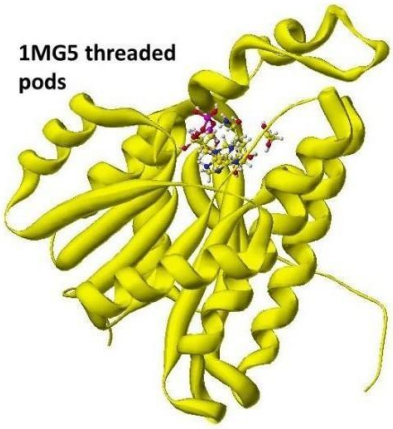

Figure 76. Threaded pods view of ADH

In the fixing process of a downloaded protein structure, lysine is exhibited as a strange molecule whose ε-amine hydrogen connects to strange oxygen located far from the lysine. The ε-amino nitrogen should be a plus charge sp^3 atom, but it appears as sp^2 amine. Carefully watch aspartic and glutamic acid carbonyl groups. The double bond appears as a single bond, and the sulfur atom of cysteine is also incorrectly appeared. Usually, residual amino acids are presented as corrected structures; however, we must carefully watch their structure before further analysis. Select an amino acid on the sequence chart, watch the enlarged structure, and watch step-by-step and correct the structure. Figure 77 shows an extracted structure of coenzyme NAD and the fixed structure.

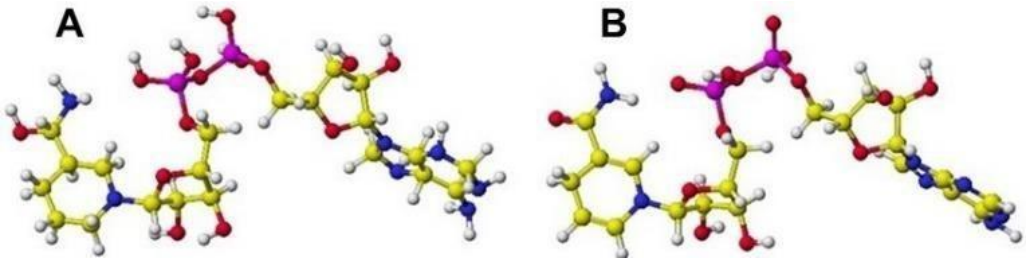

Figure 77. Downloaded and extracted NAD (A) and corrected NAD (B), Red (black), Blue (dark gray), yellow (light gray), white, and large magenta (black) are oxygen, nitrogen, carbon, hydrogen, and phosphorus.

After correcting the protein structure, the thread structure presents the location of the coenzyme and substitute. Then, optimize the structure using the MM2 program. Now, replace the original substrate with a targeting analyte and optimize the new complex structure. Repeat the process and analyze the enzyme specificity. Figures 78 and 79 demonstrate the optimized structures, including isopropyl alcohol and acetaldehyde.

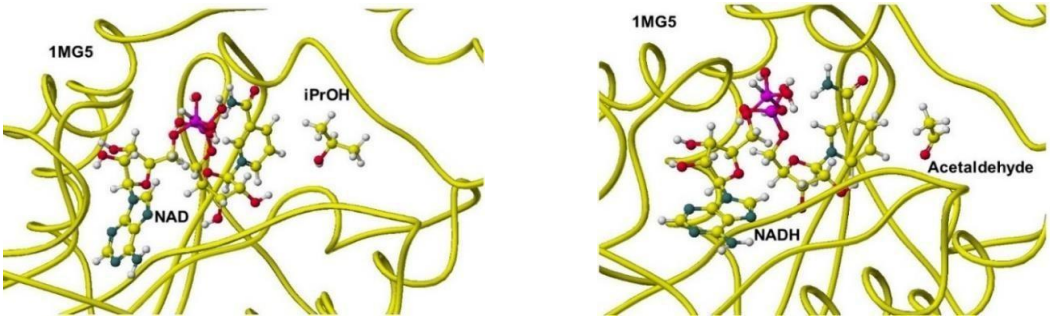

Figure 78. Optimized structures of isopropyl alcohol oxidation and acetaldehyde reduction reaction

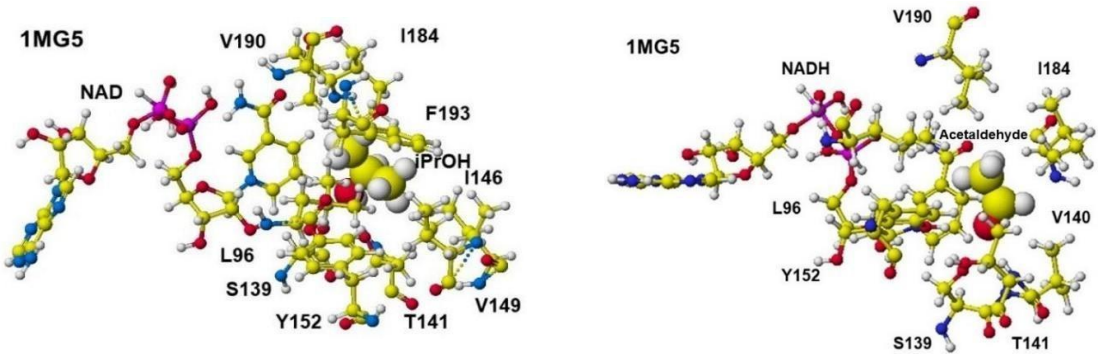

Figure 79. Extracted conformations of isopropyl alcohol and acetaldehyde locations with NAD.

After optimizing the complex structure, extract molecules within 3Å from the substitute, as shown in Figure 79. The extracted complex is locked; then optimized using MOPAC PM5 or the latest program to analyze the specificity. Read apc of target atoms and study the balance from the original value. The difference (balance) of the apc value indicates the reactivity: the larger the value, the stronger the reaction. The balance (Δ) apc values of α-carbon was related to reactivity, suggesting the enzyme's substrate specificity. The Δapc values of ethyl alcohol, propyl alcohol, butyl alcohol, pentyl alcohol, isopropyl alcohol, isobutyl alcohol, furfural, allyl alcohol, and cinnamyl alcohol are related to their V max/*K*m($min^{-1} \cdot mg^{-1}$) values with a correlation coefficient of 0.838 (n = 9).

In the oxidative reaction, V max/ *K*m ($min^{-1} \cdot mg^{-1}$) values correlated to the Δapc values of the 5^{th} carbon of pyridine ring with r = 0.915 (n = 9). The substitutes are formaldehyde, acetaldehyde, propyl aldehyde, butyl aldehyde, pentyl aldehyde, benzyl aldehyde, furfural, acrolein, and cinnamyl aldehyde.

The structure of PDB 4W6Z of zinc-dependent ADH (ADHZ) from yeast is shown in Figure 80. The thread structure indicated that the downloaded structure is like a dimer. It looks like two molecules, as shown in Figures 80 and 81; the rotating structure indicates a tetramer (Figure 82). Figure 83 shows the selected dimer. The left side complex did not include coenzyme; therefore, the right side complex was used. One set of the enzyme, including a coenzyme and a substitute, is shown in Figure 84. Figure 85 indicates the precise location of zinc, coenzyme, and substitute.

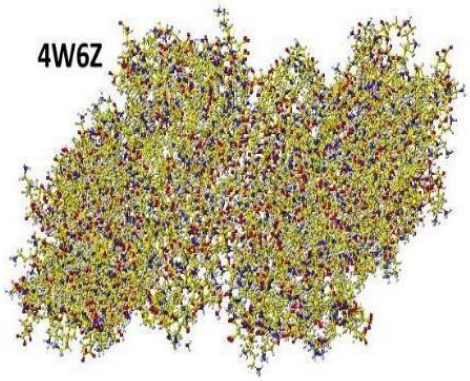

Figure 80. Downloaded ADHZ, 4W6Z

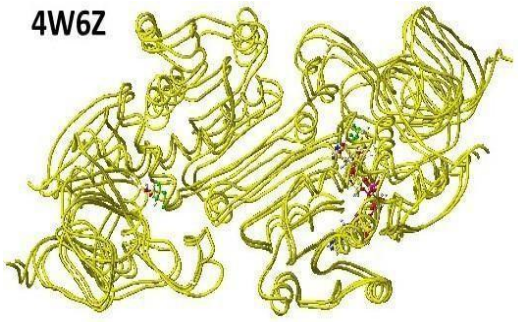

Figure 81. Thread structure of Figure 80.

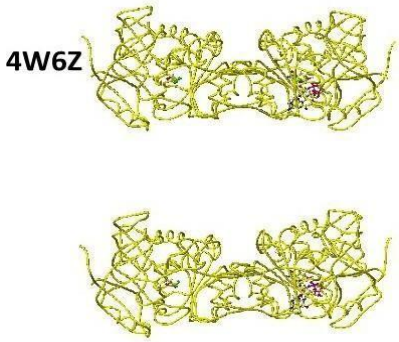

Figure 82. Rotated structure of Figure 81

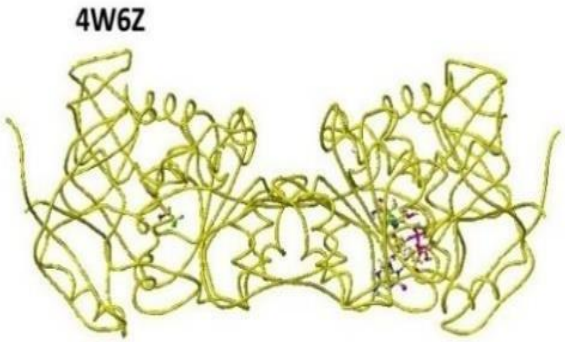

Figure 83. A pair of 4W6Z structure

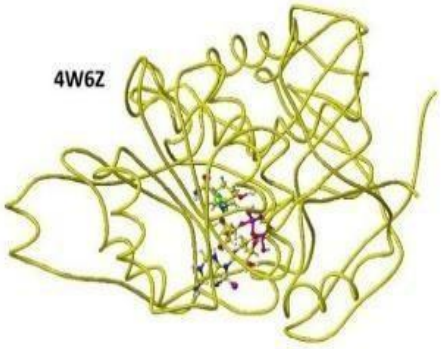

Figure 84. A set of enzyme ADHZ.

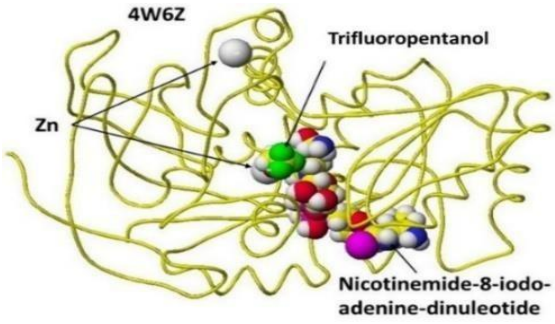

Figure 85. Location of coenzyme, zinc, and substitute

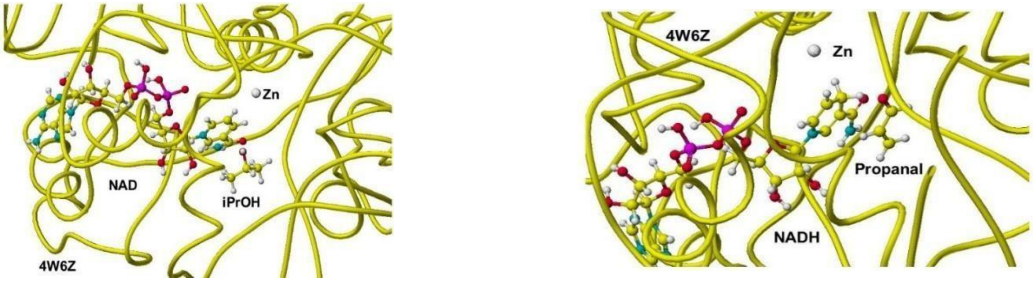

Figure 86. Optimized locations of isopropyl alcohol and propyl aldehyde

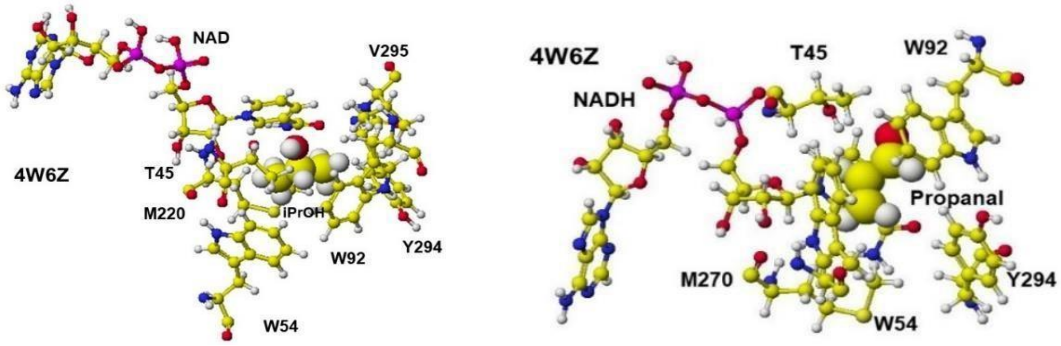

Figure 86a. Extracted conformations around iPrOH and Propanal

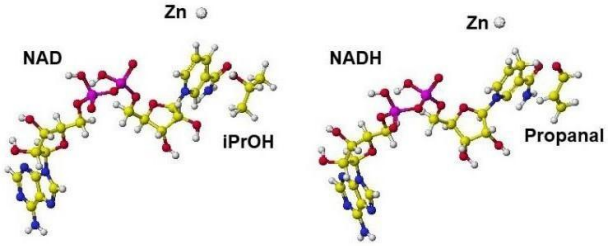

Figure 87. Extracted conformations of coenzyme, zinc, and substitute

The structure of proteinogenic amino acids in yeast ADHZ (PDB 4W6Z) was right; therefore, after correcting the structure of the coenzyme and substitute, the complex structure was optimized using the MM2 program. Replaced the original substitute with target alcohol and optimized the structure. This process was repeated as done for the 1MG5 complex and analyzed the reaction selectivity. Then, selected molecules within 3Å locked these molecules (Figure 87) and optimized using MOPAC PM5 (or the latest program). Read the α-carbon's apc of ethyl alcohol, propyl alcohol, butyl alcohol, pentyl alcohol, isopropyl alcohol, isobutyl alcohol, furfural, allyl alcohol, and cinnamyl alcohol, and the difference from the original values was calculated. The Δapc values indicated the enzyme's substrate specificity. The correlation coefficient to their Vmax/*K* m ($min^{-1} \cdot mg^{-1}$) values was 0.869 (n = 9). In the oxidative reaction, the correlation between the Δapc values of the 5th carbon of the pyridine ring and their Vmax/*K*m ($min^{-1} \cdot mg^{-1}$) was r = 0.915 (n = 9). The substrates were formaldehyde, acetaldehyde, propyl aldehyde, butyl aldehyde, pentyl aldehyde, benzyl aldehyde, furfural, acrolein, and cinnamyl aldehyde.

Studying the enzyme's substrate specificity is easy if the stereo structure of proteins is listed in the PDB file. Download a structure, carefully correct the molecule's structure, then optimize the complex structure using an MM2 program. Then replace the original substitute with a target substitute by superimposing these structures and optimizing the new complex structure. Extract molecules within 3Å from the substitute, and lock them for further optimization using MOPAC PM5 or the latest program to obtain apc values. Calculate the balance of apc values and correlate it with the measured reactivity. The following chapters demonstrate the enzyme reactivity of different enzymes.

2.4. Cinnamyl-alcohol dehydrogenase (CAD) ELI3-2

CAD, a YMR318C gene product, is specific for NADPH and shows activity for a wide variety of substrates. In the context of CAD, aldehydes are processed with a 50-fold higher catalytic efficiency than the corresponding alcohols [67]. The apo and holo-structures of an NADPH-dependent CAD from *Saccharomyces cerevisiae* were reported. The Saccharomyces cerevisiae ScAdh6p is structurally a heterodimer composed of one subunit in the apo conformation and the other subunit in the holo conformation. The specificity of ScAdh6p towards NADPH is mainly due to the tripod-like interactions of the NADPH terminal phosphate group with the S-210, R-211, and K-215 residues of the enzyme. The size and shape of the substrate-binding pocket correlated well with the substrate specificity of ScAdh6p towards cinnamaldehyde and other aromatic compounds. The function of the CAD enzymes found in bacteria and yeast needs to be established clearly [65]. CAD enzymes were originally discovered

in plants, where they catalyze the biosynthesis of lignin precursors. Transgenic trees that exhibit reduced CAD activity are easier to delignify; hence, this family of enzymes is a favored target for biotechnological modifications [68]. However, one of the members of the CAD family, ELI3, shows different enzymatic activities that are not related to lignin synthesis. The enzyme mannitol dehydrogenase, found in celery, oxidizes mannitol to mannose. Mannitol dehydrogenase is the ELI3 pathogenesis-related protein from parsley and Arabidopsis [67]. The biochemical function of *Arabidopsis thaliana* defense-related protein ELI3-2, found in *Escherichia coli,* is aromatic alcohol: $NADP^+$ oxidoreductase enzyme. This enzyme demonstrates a strong preference for various aromatic aldehydes in comparison to the corresponding alcohols; however, no mannitol dehydrogenase activity was detected [70].

Above mentioned reports do not provide a clear answer for the ADH reaction mechanism. The role of a cofactor is to activate the protein by either changing its 3D structure or by actually participating in the overall reaction mechanism. The contribution of zinc in the ADH mechanism have been studied using a model compound in non-aqueous condition; however, the effects of zinc catalysis in terms of rate enhancements or product yield were small and did not give a proper understanding of the important enzymatic process [71, 72]. Therefore, the crystal structures of a zinc-dependent *Saccharomyces cerevisiae* ADH (4W6Z in PDB) and a zinc-independent *Drosophila melanogaster* ADH (1MG5 in PDB) were used as model enzymes, and their binding affinities were evaluated after replacing the substrate with alcohols and aldehydes to study the ADH reaction mechanism. Further study was carried out for the quantitative analysis of the enzyme reactivity of CAD ELI3 [73].

The biochemical function of *Arabidopsis thaliana* defense-related protein ELI3-2, found in *Escherichia coli,* is aromatic alcohol: $NADP^+$ oxidoreductase enzyme. This enzyme demonstrates a strong preference for various aromatic aldehydes compared to the corresponding alcohols; however, no mannitol dehydrogenase activity was detected. The downloaded cinnamylalcoholdehydrogenase (CAD-2CP5) did not include coenzyme NADP+; therefore, 1PIW was downloaded and used as a mold.

The amino acid sequences of ELI3 and 1PIW are different, and their sequence similarity is 33.4%. However, if the enzyme reaction mechanisms were to be the same for both enzymes, they should have similar stereo conformations. Hence, the amino acid residues of 1PIW were replaced by those of ELI3, and the conformation was optimized using MM2 calculations [25]. Figure 88 shows the downloaded 1PIW structure, and Figure 89 shows the ELI3 modified from 1PIW.

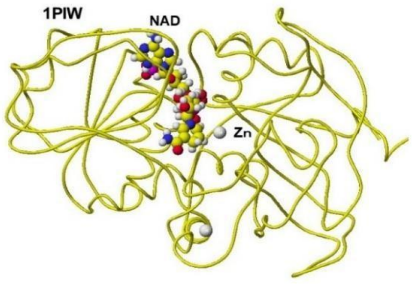

Figure 88. Structure of downloaded 1PIW

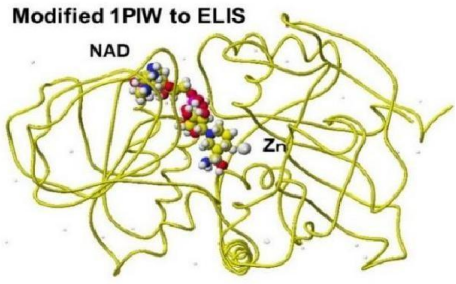

Figure 89. Constructed ELI from 1PIW

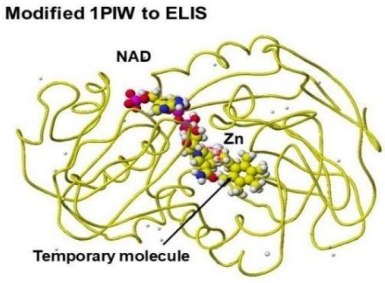

Figure 90. ELI3 with high molecular mass substrate

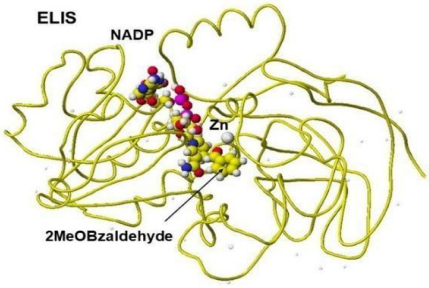

Figure 91. ELI3 with 2-methoxybenzaldehyde

The 1PIW modified ELI3 structure kept the fundamental stereo structure of 1PIW. ELI3 handles large molecules; therefore, the original substrate was modified to enlarge the molecular mass for easy docking with large compounds, as shown in Figure 90. Then, the temporary substrate was replaced with a target substrate. Figure 91 shows the optimized ELI3 and 2-methoxybenzaldehyde complex. Figure 92 shows the ELI3 and 4-Coumaraldehyde complex, and Figure 93 shows the extracted molecules within 3Å from the substitute.

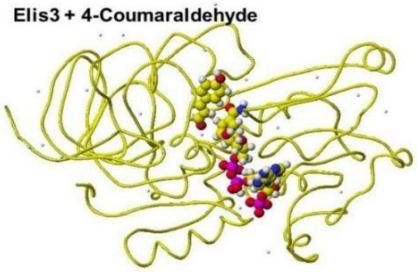

Figure 92. ELI3 and 4-coumaraldehyde complex

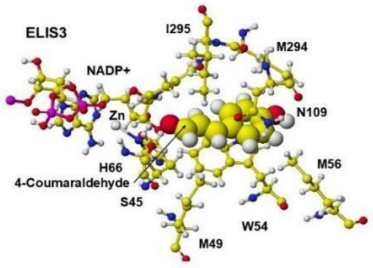

Figure 93. Location of amino acids, Zn, and $NADP^+$

In the modification process from the mold protein to a target protein, step-by-step optimization is necessary. Figure 94 shows the optimized ELI3 structure after replacing all amino acids. The optimized structure kept the helix structures, but the interactions between coils failed, and the coenzyme was wholly separated.

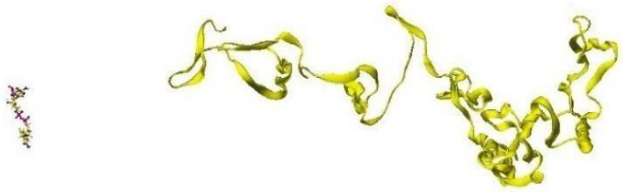

Figure 94. Directly optimized ELI3 structure after replacing whole amino acids.

Technically, replacing amino acids and optimizing processes is crucial to modifying the original protein to the mutant. All amino acids were first locked during stereo replacement to avoid effects on the original stereo structure. Subsequently, selected amino acids at the beginning and end positions of the protein were replaced under unlocked conditions because changes to these amino acids do not damage the stereo structure of the protein. The resulting new structure was then optimized using the MM2 calculation.

An amino acid within a helix was selected and replaced with the desired amino acid in the second step. The whole structure was optimized, while the new amino acid was kept unlocked. Further, the conformation of the replaced amino acid was analyzed to make sure that this amino acid was independent of other amino acids. Consequently, the newly replaced amino acid and both side amino acids were unlocked, and the protein structure was optimized. The entire stereo structure was optimized again by unlocking all amino acids. Amino acids present in helices were unlocked, if necessary, before final optimization using MM2 [26].

First, replacing the helix amino acids, then replacing the connected ribbon high freedom peptide amino acids. Replacing both end amino acids is simple; these amino acids may not contribute to the enzyme reaction. Further attention is to replacing the large mass substrate with the small original substrate used to make the crystal because the steric hindrance may cause unacceptable conformation. The stereo structure of ELI3 shown in Figure 89 indicates that the reaction chamber space is very narrow for large mass substrates. Therefore, the substrate trifluoroalcohol fluorine is converted to methyl to enlarge the reaction chamber, as shown in Figure 90. The reaction center group position has to keep the location, and unreacted may cause steric hindrance groups to be enlarged. When further enlarging, the reaction chamber converts one hydrogen of methyl.

Now, replace the original substrate with a targeting analyte by superimposing their alcoholic hydroxy or aldehyde carbonyl groups; optimize the new complex structure. Repeat the process and analyze the enzyme specificity. Figure 95 demonstrates the optimized structure of 2-methoxybenzaldehyde, zinc, NADP+, and S45 conformation with their atomic distance and apc values. This approach can analyze enzyme reactivity related to

substrate reactivity (electron localization); however, the cinnamaldehyde reactive group is located against the coenzyme after optimizing the Amber program with the auto-docking method using the 1PIW enzyme. The automatic operation using the auto-docking program should be doubted.

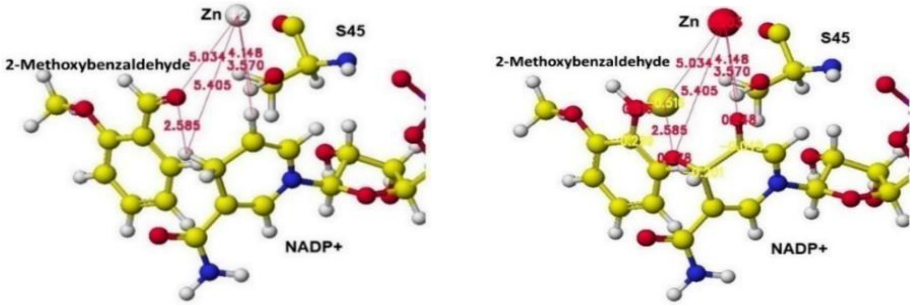

Figure 95. Location of 2-methoxybenzaldehyde and their atomic distance and apc

The nearest atom from the aromatic aldehyde oxygen was threonine hydrogen, but the reactive hydrogen was the 4th carbon-hydrogen of the pyridine ring. The enzyme reactivity of the aromatic aldehydes, V_{max}/K_m, correlated well with the apc on the analyte aldehyde carbon, the 4th-carbon, and the 4th-hydrogen of the pyridine ring. The correlation coefficients were 0.785, 0.730, and 0.754 (n = 6), respectively. The highest correlation coefficient of 0.899 (n = 6) was obtained for the atomic distance between the aldehyde oxygen and the 4th-carbon of the pyridine ring.

The substrates were 2-methoxybenzaldehyde, 3-methoxybenzaldehyde, salicylaldehyde, benzaldehyde, cinnamaldehyde, and 4-coumaraldehyde. The oxygen of cinnamaldehyde and 4-coumraaldehyde existed near zinc; therefore, the zinc should contribute to the reaction. The above results support the feasibility of the modified ELI3 structure from 1PIW.

2.5. Alanine racemase

The racemization mechanism of amino acids was studied using arylglycines as the model amino acids. The zwitterion had the greatest reactivity. The inductive effect of the NH_3^+ group stabilizes the incipient carbanion and reduces the electron density of the α-carbon removal of the proton attached to the α-carbon leaves behind a planar carbanion [74]. Introducing an electron-negative substituent on the α-carbon atom or on the amino group promotes racemization. Ionic strength is modestly affected by this reaction. The push-pull mechanism was proposed for the racemization of arylglycines in sodium phosphate buffer [75]. The racemization of alanine by alanine racemase is thought to be proceeded by an initial *trans*-alimentation, followed by α-hydrogen (αH) abstraction to give the resonance-stabilized carbanion. Deprotonation on the opposite face yields the antipodal aldimine with subsequent release of the isomerized alanine moiety. The differential active sites for *R*- and *S*-alanine has been proposed. The detailed mechanistic features, however, remain unclear [76]. The crystal structures of alanine racemase bound with reaction intermediate analogs, *N*-(5'-phosphopyridoxyl)-*S*-alanine and *N*-(5'-phosphopyridoxyl)-*R*-alanine, were determined. Tyrosine-265' (Y265') and lysine-39 (K39) are the catalytic bases for abstracting the α-proton from *S*- and *R*-alanine. The alanine carboxyl group directly contributes to mediating proton transfer between the two catalytic bases K39 and Y265'. The protonated carboxylic group is readily formed to stabilize the α-carbanion [77]. PLP enzymes exist in their resting state as Schiff bases with an active site lysine residue. The incoming amine-containing substrate displaces the lysine ε-amino group from the internal aldimine. Y265' and K39 are likely to be the two acid/base catalysts in a two-base mechanism of racemization [78]. The results indicate that the amino group of the substrate amino acid should be close to the binding site. The efficient catalysis of *S*-alanine deprotonation by PLP and alanine racemase was studied using a computational chemical method. Large solvation effects of the external aldimine cofactor lower the p*K*a of the α-amino acid. Unprotonated PLP increases the acidity of the α-amino acid [79]. Co-enzyme P.L.P. contributes to the racemization reaction process. The electron delocalization in PLP is affected by R136 and R219 [80].

Racemization occurs in vitro without an enzyme [75,81]. If the reaction process follows the same scheme in vivo, the ionized alanine should be located near the aldehyde of PLP, or the lysine (K39) nitrogen binds with PLP

and replaces K39. Racemization occurs when a substrate alanine must compete with K39 to bind with the PLP aldehyde. An αH on the substrate alanine indicates the possibility of deprotonation inside the alanine racemase. Here, the reaction selectivity of alanine racemase mutants was quantitatively studied based on the above-reported results, and the selectivity of the mutants was compared according to the stereo structure of the alanine racemase. The selective reactivity was determined from data obtained using the mutants arginine-219-lysine (R219K), arginine-219-alanine (R219A), and arginine-219-glutamic acid (R219E) to investigate the role of R219 in catalysis [82]. Different conformations, including K39-conjugated PLP, were constructed to make complexes with either *S*- or *R*-alanine, and the structures were optimized. The conformation of alanine was then examined to study the reactivity of the mutants. The PLP ring nitrogen is involved in an intermolecular OHN hydrogen bond with an aspartic acid (Q222) side-chain, and the phosphate group forms three hydrogen bonds with other amino acid residues of aspartate aminotransferase from *Escherichia coli* [83].

R-Amino acids were believed not to be residual amino acids; however, improving the analytical method found a small amount of *R*-amino acids existed in various locations. Especially, anadromous fish store a large amount of *R*-amino acids in the sea and converts them to *S*-amino acid in the river. *R*-amino acid is not a trace amount; therefore, it is easily detected without analytical error. The conversion is enzymatically achieved; therefore, the enzyme racemase activity has been studied in many spaces. Racemase requires pyridoxal 5'-phosphate (PLP) as the coenzyme. The quantitative analysis of the reaction mechanisms is not simple because the properties of precursor and reaction products are very identical. Oxidation and reduction reactions produce different molecules; therefore, identifying these compounds is relatively easy compared to optical isomers. Usually, the racemization mechanisms are believed to occur dynamically by removing α-hydrogen from one side and adding hydrogen from another side. Another possible mechanism is that the amino acid becomes a flat structure and then turns over inside the reaction chamber.

The alanine racemase 1L6G structure, whose substrate is *R*-alanine, was downloaded from the RCSB Protein Data Bank, and any irregular residues and atoms were corrected. The PLP-alanine complex was then separated into individual molecules. Mutants were constructed by replacing R219 with different amino acids. The stereo structure of the complexes was optimized using molecular mechanics force-field parameters (MM2). Furthermore, the apc of key atoms was calculated using MOPAC PM5 after extracting the *R*-alanine, PLP, and surrounding amino acid residues within 3Å of the *R*-alanine. Figure 96 shows the downloaded 1l6g. Figure 97 shows water molecules by adding hydrogen to oxygen atoms using the Valence menu.

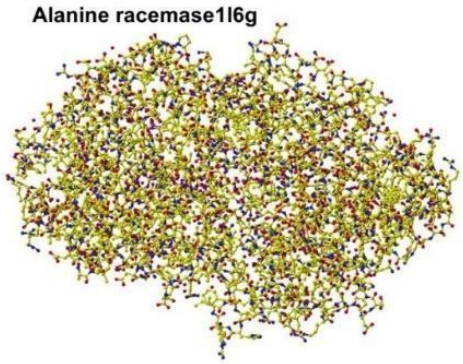

Figure 96. Downloaded alanine racemase1l6g.

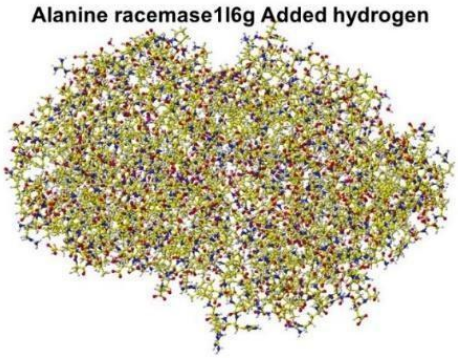

Figure 97. Addition of hydrogen to erase water

Figure 98 exhibits the distribution of water molecules; however, water molecules do not exist between coenzyme PLP and *R*-alanine. Figure 99 shows the thread structure, and further correction of the molecule is necessary. The K129 ε-amino group nitrogen structure should be an ionized sp^3 atom and should not bind water molecules circled in Figure 100. Cut bond between *R*-alanine and PLP and collected the structures of PLP and *R*-alanine. The alanine amino group should be an amino ion, and the carbonyl group should be recovered after replacing carbon with oxygen. The single bonds of the PLP pyridine ring were converted to double bonds, and sp^3 carbon was fixed to sp^2 carbon, then used Valence to adjust the numbers of hydrogen. In addition, the hydroxy oxygen atom should be sp^2 and fixed atomic distances.

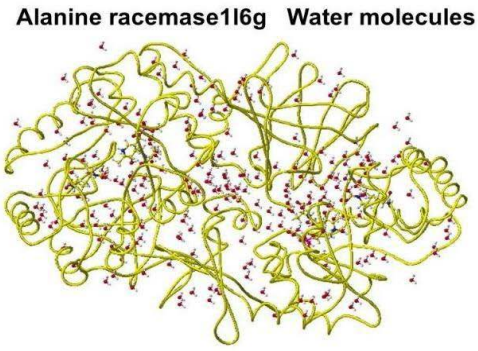

Figure 98. Distribution of water molecules

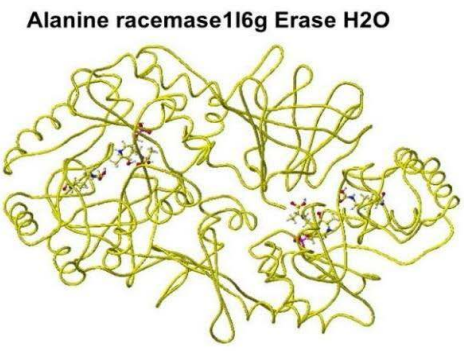

Figure 99. Protein (1l6g) spread structure

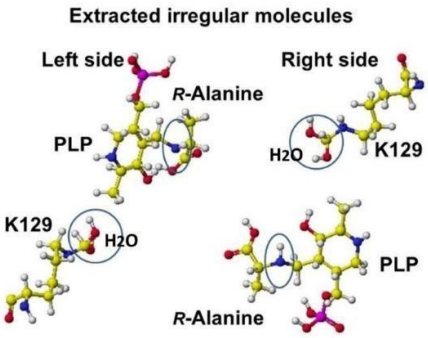

Figure 100. Extracted circled unrealistic molecules

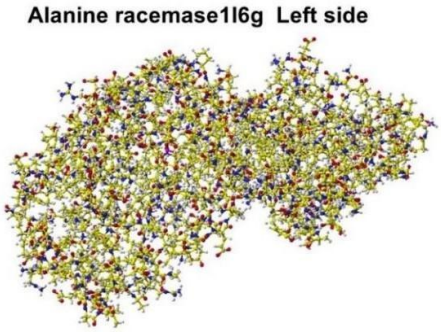

Figure 101. Left-hand side structure of Figure 99

Figure 101 shows the corrected structure of Figure 99 left-hand side. While correcting unrealistic molecules, lock whole molecules to keep the stereo structure and unlock only the molecule to be corrected. After one correction, lock the molecule, then move to correct the following molecule. Repeat this process provides a molecule for further study. After the correction, optimize the complex structure using the MM2 program.

Figure 102 shows the optimized structure with *R*-alanine; then, lock the structure in Figure 102, and replace *R*-alanine with *S*-alanine after superimposing their carboxy groups. Figure 103 shows the optimized structure with *S*-alanine. After optimizing structures Figures 102 and 103 show the extracted molecules within 3Å from *R*- and *S*-alanines. Then, locked the structures and optimized using the PM5 program to obtain atomic distance and apc value of target atoms. Figures 104 and 105 show their extracted complex structures for *R*- and *S*-alanines.

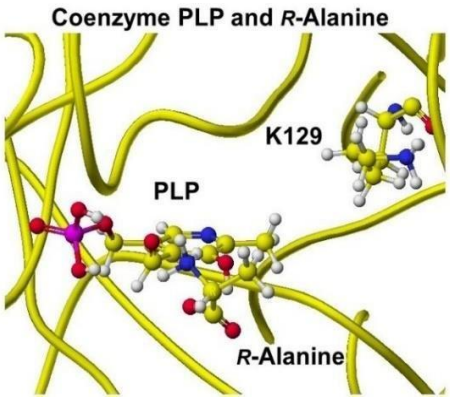

Figure 102. Optimized complex structure with *R*-alanine

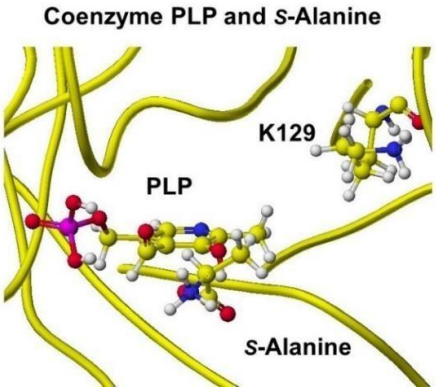

Figure 103. Optimized complex structure with *S*-alanine

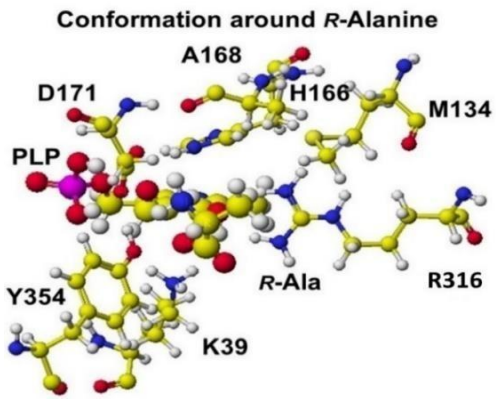

Figure 104. Molecules within 3Å from *R*-alanine

Figure 105. Molecules within 3Å from *S*-alanine

Figure 104 shows the properties of original *R*- and *S*-alanines and Figure 105 shows the properties of extracted *R*- and *S*-alanines from their complex structures for analyzing the balance. Figures 106and 107 show the atomic angles of these *R*- and *S*-amino acids.

Figure 106. The original structure of *R*- and *S*-alanine

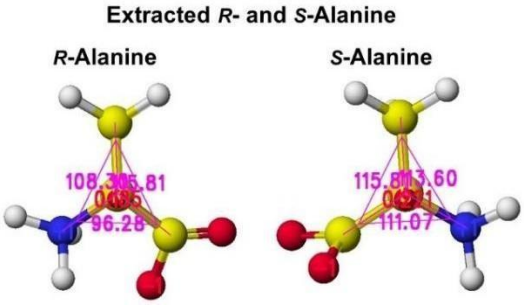

Figure 107. Extracted structure of *R*- and *S*-alanine

When the trigonal pyramid structure conversion process from *R*-alanine to *S*-alanine passes the flat conformation, α-hydrogen (αH) properties should produce different values from the original values. Therefore, the atomic angle related to αH and apc should be changed. In Figure 106, the sum of atomic angle was 322.29°, and apc of αH and α-carbon (αC) were 0.186 and - 0.240 au for both *R*- and *S*-alanines. In Figure 12, the sum of atomic angle was 320.39°, and apc of αH and αC were 0.185 and -0.166 au for *R*-alanine. However, the sum of atomic angle was 340.50°, and the apc of αH was 0.221 au for *S*-alanine. The racemization produced such a change of atomic angle and apc.

In addition, the same analysis was performed using the downloaded 1l6f file where *R*-alanine is free from PLP Deprotonation of the αC and the formation of imine are the basic mechanisms underlying alanine racemase reactivity. The atomic distance between αH and αC and the apc of αH changed little in the conformations of the molecular forms of PLP and tyrosine. The apc of the alanine αC was well correlated with the reactivity, and the value was high for *R*-alanine. The difference between 1l6g and 1l6f is that the structure of PLP and *R*-alanine produced a little different conclusion. Therefore, the complex with *S*-alanine of optimized 1l6g was used and reversed the process. Then, the conformation of *R*-alanine was analyzed. The apc of αH and αC were 0.202 and 0.102 au differed from the original values.

The substrate alanine could not bind with PLP and could not replace K39 bound with PLP; rather, the substrate alanine formed a complex with PLP. The calculations were performed without solvent (water). The results may not be directly comparable with those *in vitro*. However, the Lewis acid-base interaction is the strongest, and because water molecules cannot interrupt the Lewis acid-base interaction, this may work as a bridge to fill the gap. Here, the quantitative analysis of the selective reactivity of alanine racemase was achieved. The *R*-form of alanine was stable in complexes with this enzyme due to the favorability of the enzyme structure. The probability depends on the reality of the stereo structure. The downloaded secondary structure of pairs of

monomers was not the same. The computer system cannot construct the actual stereo structure by itself. Which structure is the right structure? Remains the fundamental question?

2.6. Human serine racemase

Substantial levels of *R*-serine in the mammalian brain were discovered in 1992 [85]. Mammalian SR (HSR) was first purified from rat brains and functionally characterized in 1999 [86]. The serine racemase synthesizes *R*-serine from *S*-serine and controls the *R*-serine level by oxidation of *R*-serine to pyruvate. *R*-Serine is the main endogenous co-agonist of the *N*-methyl-*D*-aspartate (NMDA)-type glutamate receptor (NMDAR) involved in important functions such as synaptic plasticity, learning, memory, and excitotoxicity. The X-ray crystal structure of mammalian and rat serine racemase were determined to provide a molecular basis for rational drug design. The racemization reaction was critically dependent on the proximity of the catalytic S82 to the substrate, as shown by the closed ligand-bound structures. [87]. SR was most active as a noncovalent dimer containing one or more free sulfhydryl in the enzyme's active center or a modulatory site. The recombinant HSR was sensitive to oxidative stress *in vivo,* perhaps consistent with a scenario in which such modification plays a role in feedback or other forms of regulation [88]. A decrease in *R*-serine concentration was reported in psychiatric diseases such as schizophrenia and bipolar disorder: association studies had linked DAO and the primate-specific gene 72 (pLG72) with schizophrenia susceptibility. The opportunity to regulate DAO activity opened the way to the *R*-serine level *in vivo* and thus to act on different pathological states involving the alteration in the NMDAR function. *R*-serine levels were decreased in cells overexpression HDAO, while co-transfection with PLP restored *R*-serine levels and decreased the HDAO activity. The results highlight the cellular function of HDAO in *R*-serine catabolism and confirm the role of pLG72 as a negative effector of the flavoenzyme. The Interaction of pLG72 to HDAO on the cytosolic side of the outer mitochondrial membrane induced enzyme inactivation and sped up its degradation. In this way, cytosolic *R*-serine was preserved, and cells were protected from oxidative stress by hydrogen peroxide generated by the flavoprotein in the cytosol. pLG72 inhibited HDAO and highlighted the specificity of class C compounds as they did not inhibit glucose oxidase or DDO [89]. The potential involvement of *R*-serine in neurodegenerative diseases pertains to the impaired activity of DAO, which has the potential for development as a therapeutic agent in Amyotrophic Lateral Sclerosis. An up-regulation of *R*-serine is caused either by impaired metabolism of *R*-serine by DAO or increased biosynthesis by SR [90]. Serine racemase was a PLP-dependent enzyme catalyzing the racemization of *S*-serine to *R*-serine; however, the enzymatic racemization reaction was not fully understood [91]. Therefore, the bi-functional reaction mechanisms of mammalian SR were quantitatively analyzed *in silico,* as was the case for DAO [25,33,34] and alanine racemase [84].

R-Serine was believed not to exist in mammalian tissue; however, the improving analytical method determined its existence in the mammalian brain. Since then, *R*-Serine has been considered the main endogenous co-agonist of the *N*-methyl-*D*-aspartate (NMDA)-type glutamate receptor (NMDAR) that involves essential functions such as synaptic plasticity, learning, memory, and excitotoxicity. Serine racemase (SR) is a pyridoxal 5'-phosphate (PLP)-dependent enzyme that catalyzes *S*-serine's racemization to *R*-serine and also oxidizes *R*-serine to pyruvate. The bi-functional reaction is supposed to occur at one location. Considering the reaction efficiency, *R*-serine converted from *S*-serine and oxidized at the same location is not realistic to produce a certain amount of *R*-serine. However, manganese exists nearby PLP like zinc for alanine racemase. Therefore, the possibility of a bi-functional reaction at separated locations was considered. The downloaded stereo structures of *Rattus norvegicus* (PDB ID: 3hmk) and mammalian (PDB ID: 3l6r and 3l6b) SR were optimized using molecular mechanic (MM2) calculation. Furthermore, the stereo structure of mammalian SR was constructed using 3hmk and the amino acid sequence data. PDB file 316b and 316r lack some amino acids (circled in Figures 2-57,58). Therefore, human SR was constructed from Rattus norvegicus SR (PDF: 3hmk) following the human SR (HSR) amino acid sequence. The downloaded stereos structures of 316b, 316r, and 3hmk are shown in Figures 108-110.

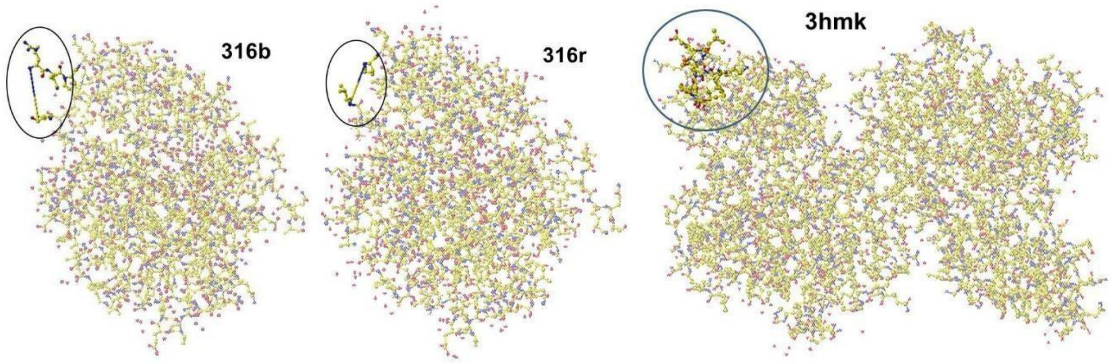

Figure 108. Downloaded 316b **Figure 109.** Downloaded 316r **Figure 110.** Downloaded 3hmk.

Figures 109 and 110 indicated a lack of peptides, and the locations are circles in these Figures. Amino acid sequences of 3hmk and HSR are very similar. Both sides of lacked peptides in 316b, 316r, and 3hmk are identical; the R58 – V68 (RGALNAVRSLV) and P76 – A90 (PKAVVTHSSGNHGQA) are the same. The difference is only T71(A71) and G74(T74) in the lacked peptide. Their secondary structures are the same ribbon band. Therefore, the replacement of two amino acids is quite simple.

After removing water molecules, the thread structures of 316b and 316r are shown in Figures 111 and 112. The location of the missing peptide is far from these reaction centers, and the reconstructed stereo structure promises to evaluate the enzyme specificity. These molecular form compounds in Figure 111 are malonic acid used to produce the complex crystal, coenzyme PLP, and manganese. An additional molecule in Figure 112 is deformed methionine.

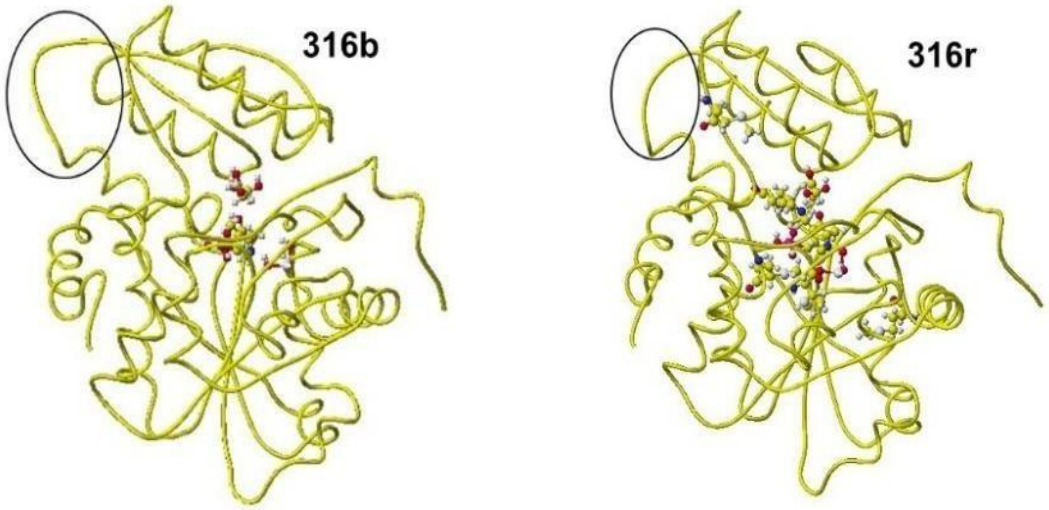

Figure 111. Downloaded and water removed 316b **Figure 112.** Downloaded and water removed 316t

316b lacks 5 amino acids (P69 – E73), and 316r lacks 7 amino acids (P69 – K75). Both structures hold malonic acid and PLP K56 binds PLP in 316r, and the bound molecule is indicated as an unknown molecule. Furthermore, M150, M189, M227, and M279 are also indicated as unknown molecules.

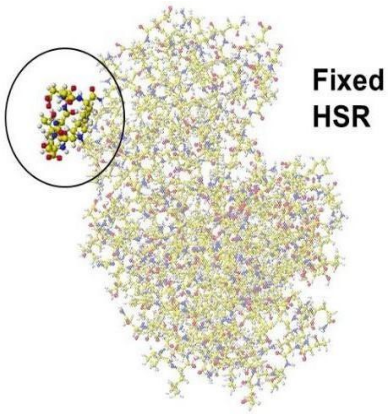

Figure 113. Corrected structure of human serine racemase

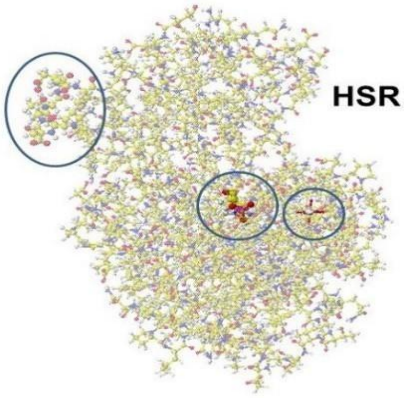

Figure 114. Location of PLP and Mn

Deprotonation of the αC and the formation of imine are the basic mechanisms underlying racemase reactivity. The serine carboxyl and amino groups contact the oppositely charged cation and anion of the residue for electron transfer. The substrate serine formed a complex with PLP. The bond angles of the serine substitute indicated the location of oxidation and racemization. Therefore, the bond angle can be used for the quantitative analysis of racemization.

In the DAO reaction, the arginine guanidyl group contacts with the *D*-amino acid carboxy group *via* ion-ion Interaction; then, coenzyme FAD carbonyl contributes electron localization. Amino acids located within 3Å from malonic acid are K56, N86, G185, G187, G188, and S313. In the case of *D*-amino acid oxidase, the locations of FAD flavine ring carbonyl and the substrate amino group are essential; therefore, the substrate of HSR is replaced with *R*-serine and optimized the structure. The optimized structures with *R*- and *S*-serine are shown in Figures 115 and 116, respectively.

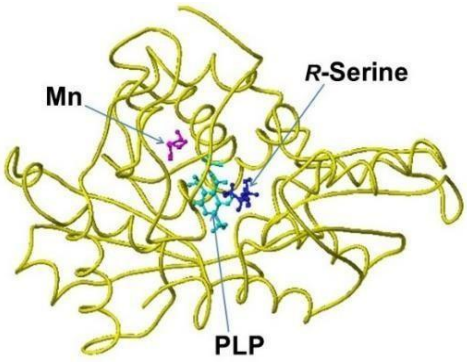

Figure 115. Location of *R*-serine, PLP, and Mn in HSR

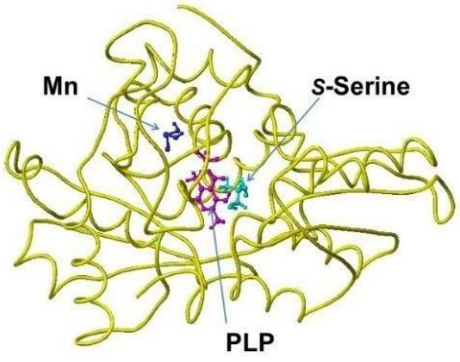

Figure 116. Location of *S*-serine, PLP, and Mn in HSR

Figure 117. Molecules within 3Å from *R*-Serine

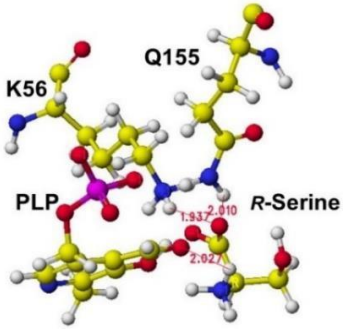

Figure 118. Atomic distance from *R*-Serine

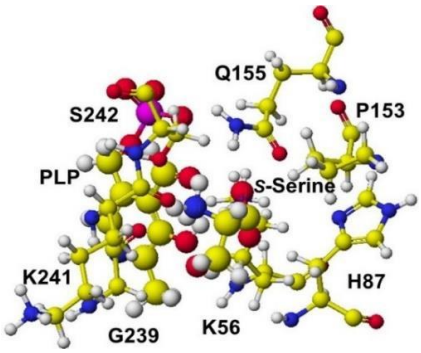

Figure 119. Molecules within 3Å from *S*-Serine

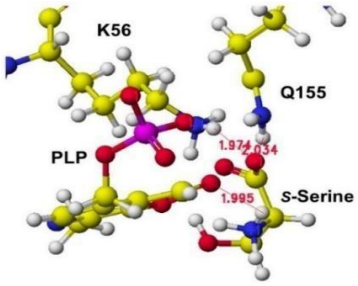

Figure 120. Atomic distance from *S*-Serine

Figures 118 and 120 show that the corresponding arginine of *D*-amino acid oxidase is lysine (K56), whose ionized ε-amino group exists within 2Å from the serine carboxy group. The glutamine amino group (Q155) may contribute to racemization. The αC apc value of *R*- and *S*-serine increased to -0.192 and -0.186 from -0.397 and -0.384, respectively. The nitrogen apc of *R*- and *S*-serine decreased from 0.076 and 0.077 to -0.017 and -0.025 au, respectively. Therefore, deamination should occur in this location as *D*-amino acid oxidase. When the original apc value (-0.384 au) of *S*-serine was used, the Δapc of *R*-serine was smaller (0.19 au) than that of *S*-serine. The result supported the fact that SR relatively oxidized *S*-serine at the location. Normally HSR favors *S*-serine elimination activity over SR activity [93]. Manganese forms a complex using the hydroxyl group as a ligand [94], and the possible conformation indicates that the hydroxyl group of serine may indeed contribute as a ligand. Serine was non-enzymatically oxidized to pyruvate at the sites where metal ions exist. However, the metal ion is located near the PLP carbonyl group, according to the schematic explanation. Manganese is located at the site opposite the oxidation reaction center in the enzymatic reaction. Furthermore, the catalytic activity of manganese is weak compared to aluminum, copper, and iron, where the metals are involved in the deamination of serine but not racemization [95]. Manganese forms multi-ligands with water molecules [96-98].

On the other hand, amino acids within 3Å from Mn are E210, A214, and D-216. The carbonyl group of glutamic acid (E210) and aspartic acid (D216) may contribute to the complex formation with Mn. Put *S*-serine at the location and optimize the complex structure. The optimized structure is shown in Figure 121, and amino acids within 3Å from *S*-serine are shown in Figure 122.

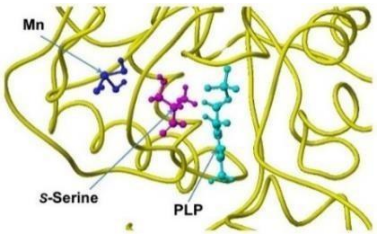

Figure 121. Optimized structure of *S*-serine and Mn complex.

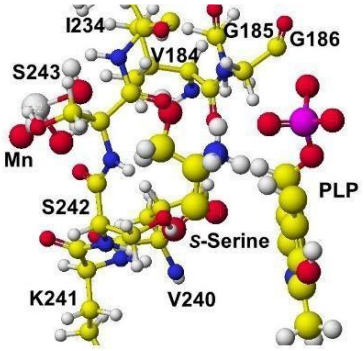

Figure 122. Amino acids within 3Å from *S*-serine

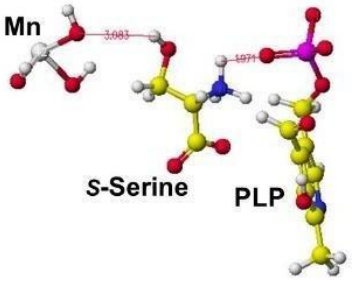

Figure 123. Extracted conformation

The optimization makes the flat serine structure. The atomic angle of the carboxy group-αC-αH expanded from 328 to 342°. However, the optimized structures with *R*-serine and alanine do not indicate their possible flat structures. Such structure change occurs only for *S*-serine, indicating that racemization should occur near Mn. I remember that Dr. Tanaka mentioned the possibility of Mn as an essential element and may contribute to nervous system disorders in 1979 Montreal. The actual activity of Mn may contribute to serine racemase activity. [99].

3. Protein-Protein Interaction from SARS COVID-19 Variants Transmissibility and the Binding Inhibitors

The fundamental analysis of ion-exchange groups made clear their molecular recognition of various compounds, and the interaction mechanisms are a combination of van der Waals forces, hydrogen bonding, and electrostatic Interaction. Furthermore, ion-ion interaction, described as electrostatic Interaction, is the primary force for protein-substrate binding. The performance was applied to analyze the selective protein-protein interactions.

Severe Acute Respiratory Syndrome Corona Virus 2 (SARS-CoV-2) (COVID-19) virus variants have spread rapidly throughout the entire world [100,101]. The binding of SARS-CoV-2 with ACE-2 (Angiotensin-converting enzyme 2) causes more severe infection than influenza. The stereo structures of SARS-CoV and SARS-CoV-2 are similar, and the ACE2-binding mode of the SARS-CoV-2 S-RBD (Spike protein Receptor-Binding Domain) is nearly identical to that of the SARS-CoV RBD [102]; however, The external fusion proteins of influenza virus (SARS-CoV) are relatively rigid, and those of SARS-CoV-2 are wildly flexible [103]. Comparison of amino acid sequences of bat-CoV, SARS-CoV, and SARS-CoV-2 determine the impact of the mutation and loops in RBD of SARS-CoV and ASRC-CoV-2 are required in order to predict a possible zoonotic event in the future [104]. Furthermore, the family tree of SARS-CoV-2 is determined and predicted new variants [105-107]. Furthermore, the newly developed analytical method was applied for quantitative *in silico* analysis of the SARS-CoV-2 S-RBD mutant's binding affinity with ACE-2. The transmissibility can be analyzed based on the molecular structure of SARS-CoV-2 mutants. A computational chemical analysis of the molecular Interactions of model compounds was performed to consider the binding site of amino acids of SARS-CoV-2 and ACE-2 [108].

The stereo structure of the SARS-CoV-2 and ACE-2 complex was determined, and the binding site of SARS-CoV-2 with ACE-2 was clarified [109]. The downloaded stereo structure of SARS-CoV-2 with the ACE-2 complex (RSC. PDB:7mjk) indicates that the binding site of ACE-2 contains many acidic amino acids [110]. Figure 124 shows the downloaded COVID-19 protein 7mjk structure consisting of a complex with saccharides. Figure 125 shows one extracted molecule without adsorbed saccharides with the location of mutated amino acids indicated using 0.5Å atom size amino acids. The missing several amino acid residues are between L176 and Q185, V620 and N641, Q675 and S691, and T827 and N856. The ACE-2 binding site with the S-RBD is indicated as ACE-2. The ACE2 protein structure is shown in Figure 126, where many acidic amino acids are lined up at the contact site with S-RBD, and these acidic amino acids are indicated as 0.5Å atoms for easy identification. The location of mutated amino acids in S-RBD is shown in Figure 127.

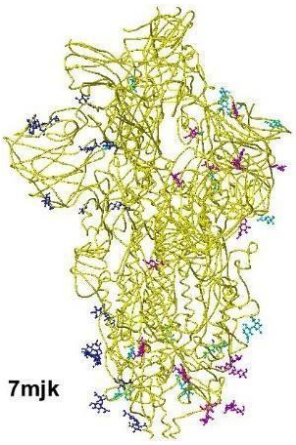

Figure 124. Structure of COVID-19 protein 7mjk

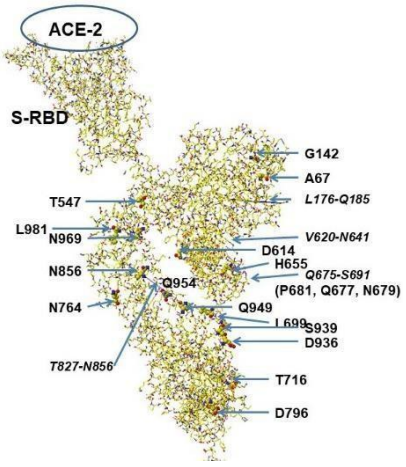

Figure 125. Location of mutated amino acids excluding S-RBD

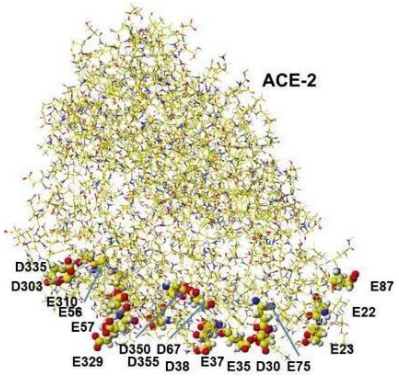

Figure 126. The contact site of ACE2 protein

The mutation of the COVID-19 protein was very fast, and over 40 mutants have been identified in two years. Several mutant structures of S-RBD (N331 - K529) are shown in Figure 127. Mutants with high transmissibility replaced the acidic and neutral amino acids with basic amino acids. The reason for their high transmissibility is

clear from the previous demonstration. Analyzing ion-ion interactions using simple ion-exchange groups demonstrated the high electrostatic energy values between a cation and an anion interaction. The strong ion-ion interaction was the primal force the proteins correct a substitute for the selective enzyme reaction.

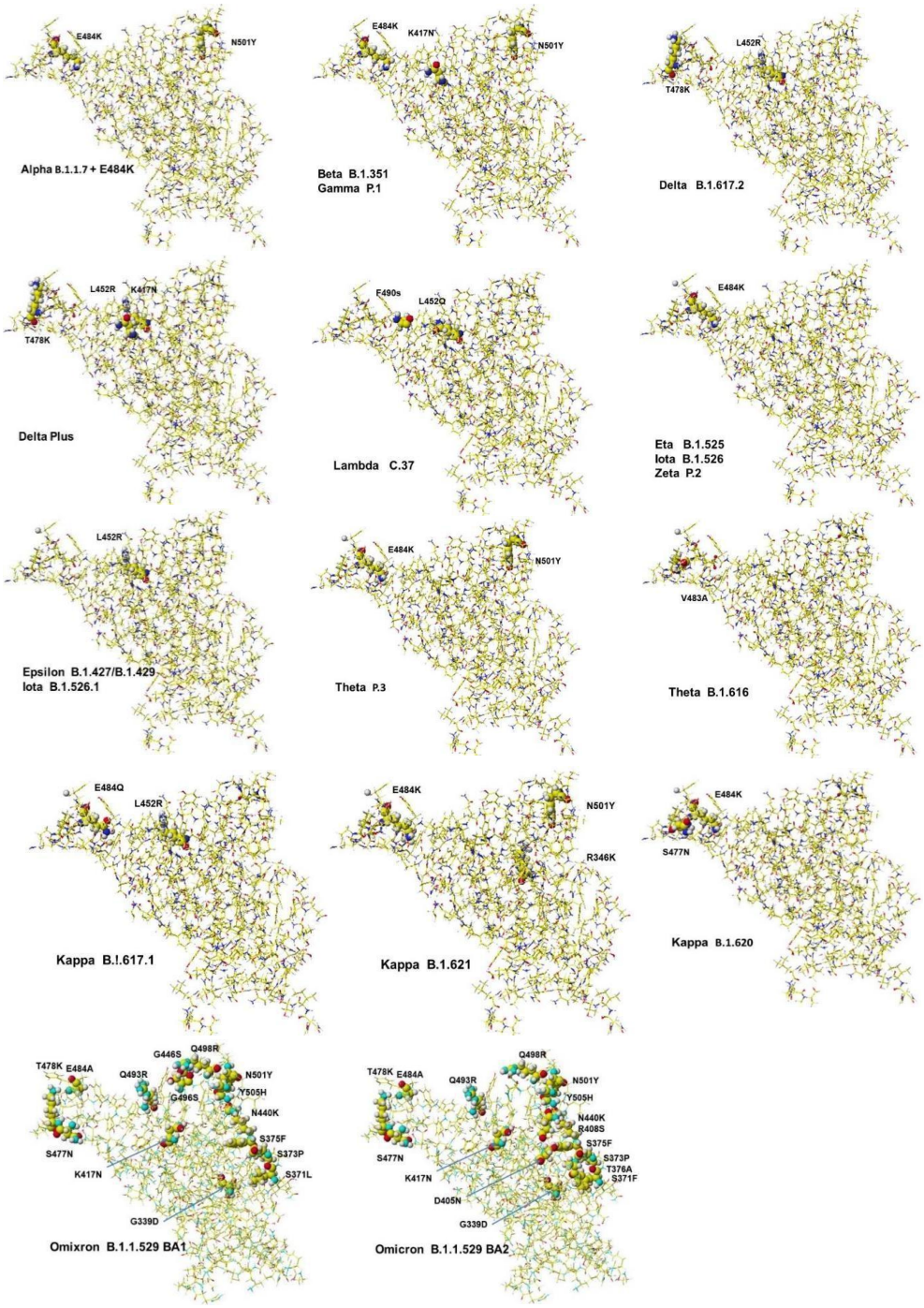

Figure 127. Mutated S-RBD protein

The S-RBD mutant amino acids of beta and gamma are the same; those of eta, iota, and zeta, and those of epsilon and another iota are the same; therefore, these individual structures are not given. Considering the contact site mutated amino acids, the existence of basic amino acids enhanced their transmissible strength. The mutated amino acids are summarized in Table 15. The transmissible strength was first analyzed based on the molecular interaction energy values between two amino acids. Omicron XD, XE, and XF are hybrid Delta with Omicron BA1, BA2, and BA3 are considered to cause severe infection. Both Omicron BA1 and BA2 include T478K mutation but not L452R mutation. Increasing numbers of basic amino acids hike the risk of severe illness.

Table 15. Mutated amino acids of SARS-CoV-2 S-RBD mutants

WHO	Lineage+	Mutated amino acids
WT		N501
Alpha	B.1.1.7	N501Y
Alpha	B.1.1.7+E484K	E484K, N501Y#2
Beta	B.1.351	K417N, E484K, N501Y
Delta	B.1.517.2	L452R, T478K
Delta plus	AY.1	K417N, L452R, T478K
Epsilon	B.1.427/B.1.429	L452R
Eta	B.1.525	E484K
Gamma	P.1	K417N, E484K, N501Y
Gamma	P.1	K417N, E484K, N501Y#2
Iota	B.1.526	E484K (Eta B.1.525)
Iota	B.1.526.1	L452R
Kappa	B.1.617.1	L452R, E484Q
Kappa	B.1.620	S477N, E484K
Kappa	B.1.621	R346K, E484K, N501Y
Lambda	C.37	L452Q, F490S
Mu	B.1.621	R346K, E484K, N501Y
Theta	P.3	E484K, N501Y (AlphaB.1.7 +E484K)
Theta	B.1.616	V483A
Zeta	P.2	E484K (Eta B.1.525)
Omicron	BA1	G339D,S371L,S373P,S375F, K417N,N440K,G446S,S477N ,T478K,E484A, Q493R,G496S,Q498R ,N501Y,Y505H
Omicron	BA2	G339D,S371F,S373P,S375F,T376A, D405N,R408S,K417N,N440K,S477N,T478K, E484A,Q493R,Q498R,N501Y,Y505H

Table 16. Molecular interaction energy values between two amino acids kcal·mol^{-1}

Amino acid	MIFS	MIHB	MIES	MIVW
Glu + Ala (A)	10.48	0.07	11.35	-0.92
Glu + Arg (R)	84.05	25.29	64.31	-3.30
Glu + Asn (N)	33.56	18.74	16.47	-2.17
Glu + Asp*(D)	-5.05	-0.05	-5.09	0.01
Glu + Glu*(E)	-5.73	0.02	-5.75	-0.01
Glu + Gln (Q)	31.27	17.19	16.49	-2.40
Glu + Gly (G)	16.21	-0.11	15.50	-1.06
Glu + His (H)	21.20	4.30	17.04	0.25
Glu + Leu (L)	8.16	0.11	7.15	1.06
Glu + Lys (K)	142.03	33.80	120.21	-8.67
Glu + Pro (P)	5.32	-0.004	5.40	0.53
Glu + Thr (T)	25.17	9.29	16.69	0.08
Glu + Tyr (Y)	24.75	9.85	20.04	-0.26
Glu + Phe (F)	12.61	0.07	9.41	2.91
Glu + Ser (S)	22.53	9.68	14.34	-0.57
Glu + Val (V)	13.26	0.28	13.97	-0.54
Tyr + Asn (N)	-27.71	-14.69	-13.24	5.56
Lys + Asn (N)	43.92	27.77	20.73	-4.65
Lys + Tyr (Y)	31.38	28.95	5.17	-3.52

MIFS, MIHB, MIES, MIVW: Molecular interaction energy values of final structure (FS), hydrogen bonding (HB), electrostatic Interaction (ES), and van der Waals force (VW). *Repulsion, no MI energy. Unit: kcal·mol^{-1}

3.1. Fast analysis of transmissibility by binding strength between two amino acids

SARS-CoV-2 tyrosine 501 (Y501), converted from N501, contacts the Y41 of ACE-2. However, the 449th, 453rd, 489th, and 505th amino acids of SARS-CoV-2 are also tyrosine. On the other hand, many acidic amino acids are present at the contact site of ACE-2. Aspartic acid (Asp, D) is located on the 30th, 38th, and 355th, and glutamic acid (Glu, E) is located on the 23rd, 34th, and 329th. Other amino acids include Y41, R357, R393, K31, and K353. Therefore, a simple binding analysis was carried out. A selected amino acid in ACE-2 was glutamic acid. The counter amino acids of SARS-CoV-2 were amino acids reported in the mutants.

The molecular interaction (MI) energy (kcal·mol^{-1}) between Glu and an amino acid on the surface of SARS-CoV-2 was calculated using the same approach as that used for the MI energy value calculation analyzed using the same approach represented at 1.2. chromatographic molecular interaction mechanisms [111]. The calculated MI energy values are presented in Table 2. MIFS, MIHB, MIES, and MIVW are the MI energy values of the optimized structure, hydrogen bonding, electrostatic interactions, and van der Waals interactions, respectively. MIHB, MIES, and MIVW indicate specific contributions to the interactions. The delta mutant, whose neutral amino acids are replaced with basic amino acids, exhibits very strong transmissibility. The basic amino acids of the delta mutant bind strongly with the acidic amino acids of ACE-2 based on ion-ion interactions, and binding (transmissible) strength is related to molecular interaction strength. Therefore, a one-to-one interaction of SARS-CoV-2 and ACE-2 amino acids was calculated as a simple model interaction. Some model interactions are shown in Figure 128.

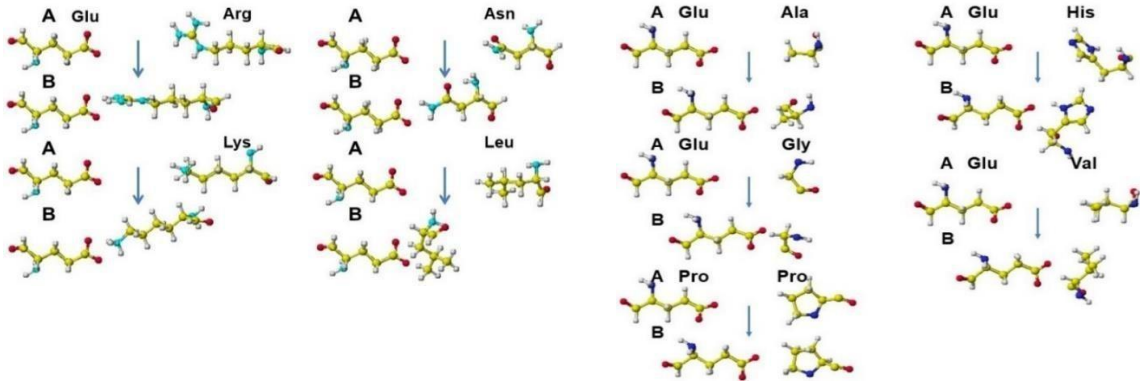

Figure 128. The molecular Interaction between two amino acids

The MI energy change by mutation was calculated using the above individual interaction energy values between two amino acids. The calculation was performed using only contact site amino acids to ACE-2. One example. MIFS energy of a mutation from arginine (R) to lysine (K) is Glu+Lys (142.03) minus Glu+Atg (84.05), making 57.98 kcal·mol^{-1}. The energy balance of other mutations for MIFS, MIHB, MIES, and MIVW are given the following equations.

MIFS energy values of mutarion (kcal·mol^{-1})
FS (R346K) = 142.03 – 84.05 = 57.98
FS (K417N) = 33.56 – 142.03 = -108.67
FS (G446S) = 22.53 – 16.21 = 6.32
FS (L452R) = 87.05 – 8.16 = 78.89
FS (L452Q) = 31.27 – 8.16 = 23.11
FS (S477N) = 33.56 – 22.53 = 11.03
FS (T478K) = 142.03 – 25.17 = 116.86
FS (V483A) = 10.48 – 13.26 = -2.78
FS (E484K) = 142.03 – 0.00 = 142.03
FS (E484Q) = 31.27 – 0.00 = 31.27
FS (E484A) = 10.48 – 0.00 = 10.48
FS (F490S) = 22.53 – 12.61 = 9.92
FS (Q493R) = 84.05 – 31.27 = 52.78
FS (G496S) = 22.53 – 16.21 = 6.32
FS (N501Y) = 24.75 – 33.56 = -8.81

MIHB energy values of mutarion (kcal·mol^{-1})
HB (R346K) = 33.80 – 25.29 = 8.51
HB (K417N) = 18.74 – 33.80 = -15.06
HB (G446S) = 9.68 – (-0.11) = 9.79
HB (L452R) = 25.29 – 0.11 = 25.18
HB (L452Q) = 17.19 – 0.11 = 17.08
HB (S477N) = 18.74 – 9.68 = 9.06
HB (T478K) = 33.80 – 9.29 = 24.51
HB (V483A) = 0.07 – 0.28 = -0.21
HB (E484K) = 33.80 – 0.00 = 33.80
HB (E484Q) = 17.19 – 0.00 = 17.19
HB (E484A) = 0.07 – 0.00 = 0.07
HB (F490S) = 9.68 – 0.07 = 9.61
HB (Q493R) = 25.29 – 17.19 = 8.1
HB (G496S) = 9.68 – (-0.11) = 9.79
HB (N501Y) = 9.85 – 17.74 = -7.89

MIES energy values of mutarion (kcal·mol^{-1})
ES (R346K) = 120.21 – 64.31 = 55.90
ES (K417N) = 16.47 – 120.21 = -103.72
ES (G446S) = 14.34 – 15.50 = 1.16
ES (L452R) = 64.31 – 7.15 = 57.16
ES (L452Q) = 16.49 – 7.15 = 9.34
ES (S477N) = 16.47 – 14.34 = 2.13
ES (T478K) = 120.21 – 16.69 = 103.52
ES (V483A) = 11.35 – 13.97 = -2.62
ES (E484K) = 120.21 – 0.00 = 120.21
ES (E484A) = 11.35 – 0.00 = 11.35
ES (E484Q) = 16.49 – 0.00 = 16.49
ES (F490S) = 14.34 – 9.41 = 4.93
ES (Q493R) = 64.31 – 16.49 = 47.82
ES (G496S) = 14.34 – 15.50 = -1.16
ES (N501Y) = 20.04 – 16.47 = 3.57

MIVW energy values of mutation (kcal·mol^{-1})
VW (R346K) = -8.67 – (-3.30) = -5.37
VW (K417N) = -2.17 – (-8.67) = 6.50
VW (G446S) = -0.57 – (-1.06) = 0.49
VW (L452R) = -3.30 – 1.06 = -2.24
VW (L452Q) = -2.40 – 1.06 = -3.46
VW (S477N) = -2.17 – (-0.57) = -1.60
VW (T478K) = -8.67 – 0.08 = -8.59
VW (V483A) = -0.92 – (-0.54) = -0.38
VW (E484K) = -8.67 – 0.00 = -8.67
VW (E484A) = -0.92 – 0.00 = -0.92
VW (E484Q) = -2.40 – 0.00 = -2.40
VW (F490S) = -0.57 – 2.91 = -3.48
VW (Q493R) = -3.30 – (-2.40) = -0.90
VW (G496S) = -0.57 – (-1.06) = 0.49
VW (N501Y) = -0.26 – (-2.17) = 1.91

The variant's MI energy values were calculated as a combination of the above individual mutation values, and the processes are achieved using the following equations. For example. WT (N501) = Glu+Asn(N) = 33.56, Alpha (N501Y) = (Glu+Tyr(Y)) – (Glu + Asn(N)) = 24.75 – 33.56 = -8.81 kcal·mol^{-1}.

MIFS energy values of mutants (kcal·mol^{-1})
WT (N501) = 33.56
Alpha (N501Y) = -8.81
Alpha+E484K (E484K+N501Y) = 142.03-8.81 = 133.22
Beta (K417N+E484K+N501Y) = -108.47+142.03-8.81 = 24.75
Gamma (K417N+E484K+N501Y)=-108.67+142.03-8.81 = 24.75
Delta (L452R+T478K)=78.89+116.86 = 195.75
Delta plus (K417N+L452R+T478K)=108.67+78.89+116.86 = 87.08
Epsilon (L452R) = 78.89
Eta (E484K) = 142.03
Iota B.1.526 (E484K) = 142.03
Iota B.1.526.1 (L452R) = 78.89
Kappa B.1.617.1 (L452R+E484Q)=78.89+31.27 = 110.16
Kappa B.1.620 (S477N+E484K)=11.03+31.27 = 42.30
Kappa B.1.621 (E484K+N501Y)=142.03-8.81 = 133.22
Lambda (L452Q+F490S) =23.11+9.92 = 33.03
Mu (E484K+N501Y) =142.03-8.81 = 133.22
Theta P.3 (E484K+N501Y)= 142.03-8.81 = 133.22
Theta B.1.616 (V483A) = -2.78
Zeta (E484K) = 142.03
Omicron BA1 (G446S+T478K+E484A+Q493R +G496S+Q498R+N501Y) = 6.32+116.86+10.48+52.78+6.32+ 52.78-8.81= 236.76
Omicron BA2 (T478K+E484A+Q493R+Q498R+N501Y) =116.86+10.86+52.78+52.78-8.81= 224.47

MIHB energy values of mutants (kcal·mol^{-1})
WT (N501) = 18.74
Alpha (N501Y) = -8.89
Alpha+E484K (E484K+N501Y) = 33.80 – 8.89=24.91
Beta (K417N+E484K+N501Y) = -15.06 + 33.80–8.89 = 9.85
Gamma (K417N+E484K+N501Y)= -15.16+33.80 -8.89 = 9.85
Delta (L452R+T478K)=25.18+24.51=49.69
Delta plus (K417N+L452R+T478K)=-15.06+25.18+24.51 = 34.63
Epsilon (L452R) = 25.18
Eta (E484K) = 33.80
Iota B.1.526 (E484K) = 33.80
Iota B.1.526.1 (L452R) = 25.18
Kappa B.1.617.1 (L452R+E484Q) = 25.18+17.19 = 42.37
Kappa B.1.620 (S477N+E484K) = 9.06+33.80 = 42.86
Kappa B.1.621 (E484K+N501Y) = 33.80-8.89 = 24.91
Lambda (L452Q+F490S) = 17.08+9.61= 26.69
Mu (E484K+N501Y) =33.80-8.89= 24.91
Theta P.3 (E484K+N501Y) = 33.80-8.89= 24.91
Theta B.1.616 (V484A) = -0.21
Zeta (E484K) = 33.80
Omicron BA1 (G446S+T478K+E484A+Q493R+ G496S+ Q498R+N501Y)=9.79+24.51+0.07 +8.10+9.79+8.10-8.89 = 51.47
Omicron BA2 (T478K+E484A+Q493R+Q498R+N501Y) =24.51+0.07+8.10+8.10-8.89 = 31.89

MIES energy values of mutants (kcal·mol^{-1})
WT (N501) = 16.47
Alpha (N501Y) = 3.57
Alpha+E484K (E484K+N501Y) = 120.21+3.57 = 123.78
Beta (K417N+E484K+N501Y) = -103.72+120.21+3.57 = 20.06
Gamma (K417N+E484K+N501Y) = -103.72+120.21+3.57 = 20.06
Delta (L452R+T478K)=57.16+103.52 = 160.68
Delta plus (K417N+L452R+T478K)=103.72+57.16+103.52 = 56.96
Epsilon (L452R) = 57.16
Eta (E484K) = 120.21
Iota B.1.526 (E484K) = 120.21
Iota B.1.526.1 (L452R) = 57.16
Kappa B.1.617.1 (L452R+E484Q) = 57.16+16.49 = 73.65
Kappa B.1.620 (S477N+E484K) = 2.13+120.21 = 122.34
Kappa B.1.621 (E484K+N501Y) = 120.21+3.57 = 123.78
Lambda (L452Q+F490S) =9.34+4.93 = 14.27
Mu (E484K+N501Y) =120.21+3.57 = 123.78
Theta P.3 (E484K+N501Y)= 120.21+3.57= 123.78
Theta B.1.616 (V484A) = -2.62
Zeta (E484K) = 120.21
Omicron BA1 (G446S+T478K+E484A+Q493R+G496S+ Q498R +N501Y) = 1.16+103.52+11.3+47.82-1.16+47.82+3.57 = 210.51
Omicron BA2 (T478K+E484A+Q493R+Q498R+N501Y) =103.52 +11.35+47.82+47.82+3.57 = 214.08

MIVW energy values of mutants (kcal·mol^{-1})
WT (N501) = -2.17
Alpha (N501Y) = 1.91
Alpha+E484K (E484K+N501Y) = -8.67 + 1.91 = -6.76
Beta (K417N+E484K+N501Y) = 6.50-8.67+1.91 = 0.26
Gamma (K417N+E484K+N501Y) = 6.50-8.67+1.9 = 0.26
Delta (L452R+T478K)=-2.24-8.59 = -10.83
Delta plus (K417N+L452R+T478K) = 6.50-2.24-8.59= -4.33
Epsilon (L452R) = -2.24
Eta (E484K) = -8.67
Iota B.1.526 (E484K) = -8.67
Iota B.1.526.1 (L452R) = -2.24
Kappa B.1.617.1 (L452R+E484Q) = -2.24-2.40 = -4.64
Kappa B.1.620 (S477N+E484K) = -1.60-8.67 = -10.27
Kappa B.1.621 (E484K+N501Y) = -8.67+1.91= -6.76
Lambda (L452Q+F490S) = -3.46-3.48 = -6.94
Mu (E484K+N501Y) = -8.67+1.91= -6.76
Theta P.3 (E484K+N501Y) = -8.67+1.91= -6.76
Theta B.1.616 (V483A) = -0.92
Zeta (E484K) = -8.67
Omicron BA1(G446S+T478K+E484A+Q493R+G496S+Q498R +N501Y) = 0.49-8.59-0-0.90+0.49-0.90+1.91= -8.42
Omicron BA2 (T478K+E484A+Q493R+Q498R+N501Y) = -8.59-0.92-0.90-0.90+1.91= -9.40

These simple analyses clearly explain the binding mechanisms and demonstrate the significant contribution of electrostatic Interaction, the supporting contribution of hydrogen bonding and van der Waals force did not affect the Interaction. Especially, the mutation to lysine affects the transmissibility. Arginine also enhances the binding. Some mutants changed one amino acid, and others changed multi amino acids of S-RBD proteins. The contribution of MI energy values of mutants was calculated between ACE-2 glutamic acid and S-RBD mutant's contacted amino acids, and the results are summarized in Table 17. The contribution of electrostatic Interaction was described using various experimental data [112-115]. The mutation to basic amino acids enhanced the ion-ion Interaction, and the calculated results support the mutant's transmissibility.

The above MI energy values were calculated for the amino acids of SARS-CoV-2 in contact with ACE-2 Glu. The order of the MIFS energy value of the mutants was Alpha < Theta B.1.616 < Beta, Gamma < Lambda < WT < Kappa B.1.620 < Epsilon, Iota B.1.526.1 < Delta plus < Kappa B.1.617.1 < Alpha + E484K, Kappa B.1.621, Mu, Theta P.3 < Eta, Iota B.1526, Zeta < Delta < Omicron BA2 < Omicron BA1. Ion–ion interaction is the strongest interaction force, and the strength can be obtained as a large MIES value. The amides exhibited relatively strong hydrogen bonding. This simple approach can provide the strength of a mutant's transmissibility. The Alpha-MIFS value was smaller than that of WT, and the transmissibility, based on the calculation, seemed weaker than that of the wild type. The reference stereo structure indicated that SARS-CoV-2 Y501 did not have head-to-head contact with ACE-2 Y41 and contacted the peptide bond nitrogen. However, SARS-CoV-2 N501

only contacted ACE-2 Y41, while SARS-CoV-2 Y501 contacted ACE-2 Y41 and K353. This mutation improved the contact site. Therefore, the MI energy was recalculated between ACE-2 Y41 and SARS-CoV-2 N501 and between ACE-2 K353 and SARS-CoV-2 Y501. The recalculated MI energy values of MIFS of WT. were a minus value (-27.71 kcal·mol^{-1}), and N501Y showed a positive value (52.27 kcal·mol^{-1}). This simple calculation provided the possible transmissibility of variants but did not include steric hindrance. Actual protein-protein interactions should include steric hindrance at the contact site. However, these calculations support the higher transmissibility of SARS COVID-19 mutants; however, the precision should improve the calculation of protein-protein binding energies.

Table 17. Molecular interaction energy values between ACE-2 Glu and SARS-CoV-2 mutants

Mutant	MIFS	MIHB	MIES	MIVW
WT	33.56	18.74	16.47	-2.17
Alpha	-8.81	-8.89	3.57	1.91
Alpha+E484K	133.22	24.91	123.78	-6.76
Beta	24.75	9.85	20.06	0.26
Gamma	24.75	9.85	20.06	0.26
Delta	195.75	49.69	160.68	-10.83
Delta plus	87.08	34.63	56.96	-4.33
Epsilon	78.89	25.18	57.16	-2.24
Eta	142.03	33.80	120.21	-8.67
Iota B.1.526	142.03	33.80	120.21	-8.67
Iota B.1.526.1	78.89	25.18	57.16	-2.24
Kappa B.1.617.1	110.16	42.37	73.65	-4.64
Kappa B.1.620	42.30	42.86	122.34	-10.27
Kappa B.1.621	133.22	24.91	123.78	-6.76
Lambda	33.03	26.69	14.27	-6.94
Mu	133.22	24.91	123.78	-6.76
Theta P.3	133.22	24.91	123.78	-6.76
Theta B.1.616	-2.78	-0.21	-2.62	-0.92
Zeta	142.03	33.80	120.21	-8.67
Omicron BA1	236.76	51.47	210.51	-8.42
Omicron BA2	224.47	31.89	214.08	-9.40

Table 18 Molecular interaction energy values betweer ACE-2 and SARS-CoV-2 mutants

Mutant	MIFS	MIHB	MIES	MIVW
WT	346.0675	284.725	186.499	-58.491
Alpha B.1.1.7	320.9545	233.255	155.734	-41.626
Alpha+E484K	442.3393	218.879	246.999	-4.801
Beta B.1.351	515.7918	340.560	302.832	-41.978
Gamma P.1	Beta			
Delta B.1.517.2	594.1785	321.588	426.310	-70.623
Delta-plus AY.1	511.2668	353.568	264.584	-53.387
Epsilon B.1.427	465.3735	289.895	279.507	-18.675
Eta B.1.525	450.1992	199.843	295.278	-22.293
IotaB.1.526	Eta B.1.525			
Iota B.1.526.1	Epsilon			
Kappa(B.1.617.1)	544.5906	311.860	337.362	-64.514
Kappa(B.1.620)	382.5573	189.907	256.668	-27.934
Kappa(B.1.621)	524.7044	238.331	388.452	-
76.510Lambda C.37345.3966198.131			186.466	-33.126
Mu B.1.621	Kappa B.1.621			
Theta P.3	Alpha+E484K			
Theta B.1.616	487.0045	296.061	279.195	-41.916
Zeta P.2	Eta B.1.525			
Omicron BA1	761.7122	389.186	484.065	-60.100
Omicron BA2	904.3286	475.158	576.588	-73.122

PDB 7kmb. Unit: kcal·mol^{-1}

Therefore, the direct Interaction between SARS-CoV-2 and ACE-2 was quantitatively analyzed to determine the transmissibility using a method used for the quantitative analysis of enzyme reactivity [116]. This calculation used the S-RBD of SARS-CoV-2 and two contact site peptides of ACE-2 (S19-S105 and E329-N394). These four end amino acids of the selected ACE-2 peptides were locked to maintain their stereo structure. This modification was applied based on the calculation capability of a desktop computer. The calculated MI energy values are presented in Table 18.

The calculated transmissibility order (MIFS) was Alpha < Lambda < WT < Alpha+E484K < Epsilon < Delta plus < Beta , Kappa B.1.621 < Kappa B.1.617.1 < Delta B.1.517.2 < Omicron BA1 < Omicron BA2. Figure 6 shows the binding conformation of Omicron BA2 and ACE-2. The Delta-mutant had demonstrated the strongest transmissibility; however, the Omicron replaced the transmissible strength. The higher transmissibility should be caused by mutation from acidic and neutral amino acids to basic amino acids. Lysine and arginine are contained in meat. The calculation was performed using a part of these proteins but not the full-size proteins, and further calculations using full-size structures should improve the precision. In particular, other parts of SARS-CoV-2 are important for protein complex tightness. However, this simple calculation provides a quick estimation of the transmissibility of the mutant and can be used to study inhibitors.

The high transmissibility of Omicron was reported [117, 118]], and the immunogenicity, immune escape, and pathogenicity were described [119]. The difference between the Omicron variant and the Delta variant was analyzed and suggested the higher transmissibility of Omicron by computational studies [120, 121]. Omicron binding affinity to hACE2 is similar to that of the prototype RBD; however, the multi mutation might affect immune escape and transmissibility [122, 123]. Pathophysiological differences between COVID-19 and HIV-1 were described and proposed antibody-based therapeutics to treat comorbid patients [124]. Scanning the RBD

molecular interactions suggested Omicron was more stable than WT [125]. The heavily mutated Omicron variant is highly susceptible to T-cell response; therefore, antibodies are likely less effective, but the activation of T-cells should improve against COVID-19 viruses [126].

3.2. COVID-19 Transmissibility and the binding inhibitors

As demonstrated in 3.1 Fast analysis of transmissibility by binding strength between two amino acids, many acidic amino acids are present at the binding site of ACE-2. The mutation of neutral amino acids of S-RBD to basic amino acids exhibited very strong transmissibility based on ion-ion Interaction. The mutation of amino acids to basic amino acids such as arginine (R) and lysine (K) of S-RBS increases the transmissibility of COVID-19. In the initial study, acidic compounds inhibited the binding of S-RBD with ACE-2 because acidic compounds are repulsed from ACE-2 acidic amino acids but form strong ion-pair with basic compounds.

Therefore, 164 compounds listed in Table 19 were investigated as potential binding inhibitors, including ingredients in flu medicines and food components and proposed drugs in the literature. First, the binding of these candidates with Alpha-S-RBD was performed. All candidates were bound at S-RBS binding site with ACE-2. Second, the binding of these candidates with the ACE-2 binding site with S-RBD was performed. Only compounds having ionized carboxy groups were repulsed. The results are indicated as "repulsed" in Table 19. Only carboxyl compounds were repulsed from ACE-2 as the ionic form. Even if the molecular form compounds were bound with ACE-2 via hydrogen bonding. Phenolic hydroxy and secondary amino groups were also formed by hydrogen bonding with ACE-2 carboxy oxygen.

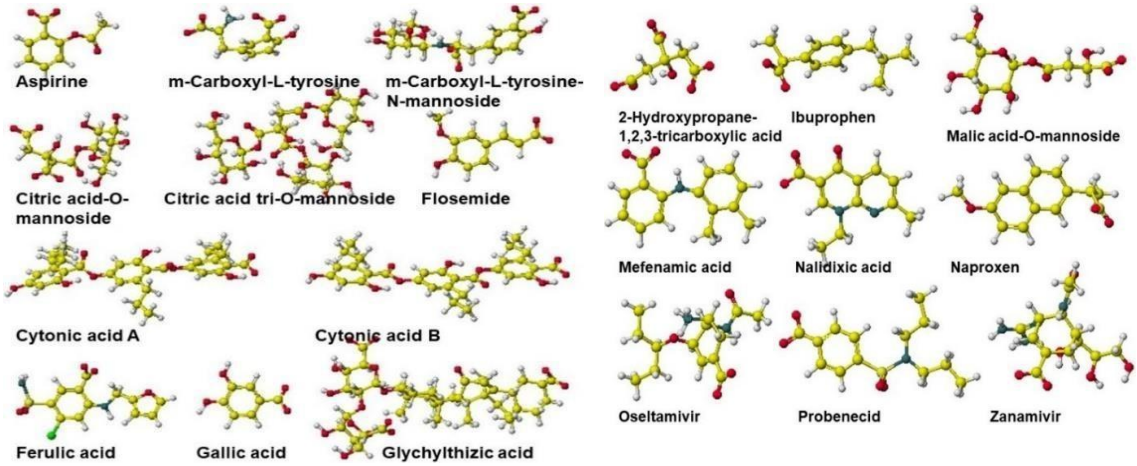

Figure 129. Binding inhibitor candidates, White, light gray, dark gray, black balls: hydrogen, carbon, nitrogen, oxygen

Table 19. Proposed compounds for anti-Covid-19

Compound [ref]	MIHB	MIES	MIVW	XlogP	logP*	pKa*
Acetaminophen	22.556	6.459	7.314	0.5	0.9(D), 0.46(S)	9.38(HS),-4.4(D)
Adrenaline	1.879	-36.645	9.929	-1.4	-1.2(D,E),-1.37(H)	8.23(HS),8.59(D),
Amentoflavone [127]	202.902	-2.314	-18.120	5		9.24(HS)
Aminoquinoline [128]	nc	nc	nc	1.3	1.28(H)	
Ascorbic acid	114.660	13.562	-14.768	-		4.1,11.6(W)
Aspirine (I)	repulsed			1.2	1.18(D),1.19(H,E)	3.47(Ch),3.49(HS)
Aspirine-O-mannoside (M)	88.702	32.790	9.539			
Aspirine-O-mannoside (I)	repulsed					
AZD1061,8895 [129]	monoclonal antibody					
Azithromycin [128,130-132]	50.893	20.479	19.384	4	3.03(D),4.02(E)	8.5(D),8.75(HS)
Bamlanivimab [133]	monoclonal antibody					
Baricitinib (Olumiant) [134]	160.670	-13.210	-15.380	-0.5		
Benzoic acid (I)	repulsed			1.9	1.87(H)	3.96, 4.2(Ch)
β-Blocker	109.747	13.473	5.982			
Calcitriol [135]	144.948	-16.333	-9.458	5.1	5(D)	
Captopril [136]	82.331	24.944	-3.189	0.3	0.34(D,E)	
Casirivimab [137]	monoclonal antibody					

Cepharanthine [138]	nc	nv	nc	6.5		
N-Chloroacetylaniline [139]	nc	nc	nc	1.6	1.63(H)-	
N-Chloroacetyl-N'-sulfonamide-piperazine[139]	168.391	-11.246	-16.554	-0.5		
N-Chloroactyl piperidinyl-4-carboxamide [139]	164.716	-1.666	-18.242			
Chlorophenylamine	57.639	5.753	3.635	1.9		
Chlorophenylamine-mannoside	117.796	26.983	-12.663	-		
Citric acid (M)	34.137	26.273	12.308	-1.7	-1.64(D,E)	2.79(D)
Citric acid (I)	repulsed					
Citric acid dimethyl	repulsed					
Citric acid trimethyl	-31.569	-28.320	18.756			
Citric acid-O-mannoside	repulsed					
Citric acid di-O-mannoside	repulsed					
Citric acid tri-O-mannoside	repulsed					
Cytonic acid A (M) [140]	263.069	-3.168	-19.231			
Cytonic acid A (I)	repulsed					
Cytonic acid B (M) [140]	234.665	11.648	-7.886			
Cytonic acid B (I)	repulsed					
Ephedrine	-20.538	-36.343	16.908	0.9	1.13(D)	9.61(Ch),10.3(D),9.65, 10.25(HS)
Etesevimab [133]	monoclonal antibody					
Ethionamide	78.667	23.403	-14.267	1.1	0.5(D)	4.49(HS)
Euchrenone a^{II} [141]	176.775	-16.253	2.503	6.5		
Ferulic acid (I)	repulsed					
Ferulic acid (M)	102.862	25.208	-2.031	1.5	1.51(H)	4.42, 4.58(HS)
Flavonoid	-19.046	-38.559	18.881			
Furosemide (M)	76.890	16.207	-5.917	2	2.03(S)	3.52,3.63(Ch),3.8,7.5(HS)
Furosemide (I)	repulsed			-		
Gallic acid (M)	13.225	5.943	7.976	0.7	0.70(H)	4.21(Ch),4.40(HS.)
Gallic acid (I)	repulsed					
Gallocatechin gallate [127]	191.495	-13.926	-21.252	1.2		
Gingerol	36.512	-20.758	22.002	2.5		
Glychylrrizic acid (M) [142]	48.689	17.600	23.219	6.4		
Glychylrrizic acid (I)	repulsed			-		
Hydroxychloroaquine[128,130-132,143]	32.042	3.842	13.720	3.6		9.67(D)
Ibuprophen (M)	-8.323	3.074	17.239	3.5	3.97(D,E)	4.45(Ch),5.3(D),4.47, 5.2(HS)
Ibuprophen (I)	repulsed					
Isopropylantipyrine	2.452	-1.553	11.248	3.6		
Ivermectin [144,145]	169.012	-7.959	5.777	4.1		
Lactic acid	470.995	-41.160	-9.790	-0.7	-0.72(D,H)	3.86(D,HS)
Lopinavir [128,131]	83.964	27.438	14.638	5.9		
Losartan [145]	166.159	-1.967	1.794	4.3	1.19(D)	5.5(D),5.6(HS),4.07,4.29, 14.27(HS)
Malic acid-O-mannoside (M)	203.675	52.086	1.901			
Malic acid-O-mannoside (I)	repulsed					
Mefenamic acid (M)	80.910	24.118	8.248	5.1	5.12(H),4.2(HM)	4.2(D),4.5(Ch)
Mefenamic acid (I)	repulsed					
Mefloquine (Lariam) [146,147]	-15.651	-37.673	22.934	3.6	4.49(E)	9.46,13.79(HS)
Molnupiravir (Lagevrio) [148,149]	6.149	10.703	18.641	-0.8		
Monoclonal antibodies [150]	monoclonal antibody					
N3 [131]	1.993	0.077	17.653			
Nalidixic acid (M)	44.072	-21.433	7.572	1.4	1.59 (D,E)	6.01(Ch),8.6(D,HS)
Nalidixic acid (I)	repulsed					
Naproxen (M)	20.794	8.143	8.723	3.3	3.18(H)	4.18(Ch), 4.15(D,HS)
Naproxen (I)	repulsed					
Oseltamivir (Tamiflu) [131,151]	repulsed			1.1	1(D)	7.7(HS)
Probenecid (M)	17.869	8.963	13.656			
Probenecid (I)	repulsed					
Remdesivir (GS5734) [128,145,131,151,148,152,143]	-29.369	-34.957	26.600	1.9		
Ritonavir [131,153,143]	44.125	23.473	20.108	6	3.9(D)	
Sotrovimab [153]	monoclonal antibody					
Unifenovir (Arbidol) (M) [154,155]	60.178	14.744	9.711	4.4		
Unifenovir (Arbidol) (I)	-43.969	-39.268	29.022			
Zanamivir (Relenza) (M)[151,152]	83.668	33.302	3.367	-3.2	-3(D)	
Zanamivir (Relenza) (I)	repulsed					

(M), (I): molecular and ionized compounds; MIFS, MIHB, MIES, MUVW: Molecular interaction energy value of the final (optimized) structure, hydrogen bonding, electrostatic and van der Waals interaction (unit: kcal·mol^{-1})
*log*P* and p*K*a from PubChem: D (Drug Bank), E(E.P.A. DSSTox), H(Hansch log*P*), S (Sangster), Ch (ChEMBL), HS (Hazardous substance data bank)

3.3. Analysis of binding inhibitors as the S-RBD complex

Several repulsed compounds being rejected the binding from ACE-2 were selected and made complexes with Delta-S-RBD. The surface of the binding site of both proteins is quite large; therefore, three acidic molecules were used to prepare the complexes with one Delta-S-RBD.

Figure 130 shows that one aspirin molecule bridged the binding between ACE-2 and Delta-S-RBD. The binding site structure was extracted and studied the structure in detail. K478 of Delta-S-RBD should be rejected from the binding with R357 of ACE-2 because both amino acids are basic. However, aspirin bridges these amino acids. This result indicated that a single carboxy group might not effectively inhibit the binding of these proteins (S-RGB and ACE-2). The same results were obtained for benzoic acid and citric acid dimethyl ester.

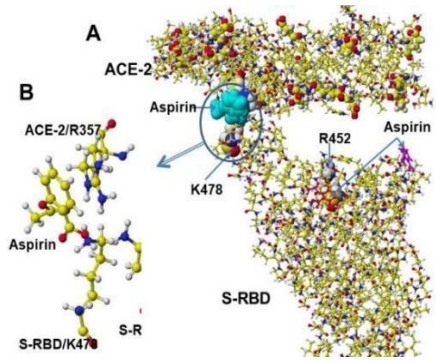

Figure 130. Docking of S-RBD and ACE2 *via* PF 07321332

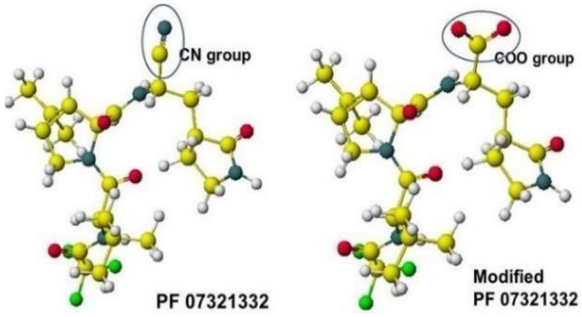

Figure 131. Stereo structure of PF 07321332 and modified PF07321332

3.2.1 Properties of PF 07321332

PF 07321332 was permitted as an oral dose drug; however, PF 07321332 was bound to ACE-2 (Table 19). The chemical structure (Figure 131) was modified for a repulsive compound because carboxy compounds were repulsed from ACE-2. The PF 07321332 cyano group was replaced with a carboxy group due to both cyano and carboxy groups are negatively charged groups. The modified PF 07321332 (Figure 131) was replaced from the original location of PF 07321332 in the protein. The complex structure of PF 07321332 and protein is PDF 7TLL [155].

The downloaded and corrected structure of 7TLL is shown in Figure 132, where the location of PF07321332 was far from the S-RBD binding site with ACE-2. The modified PF 07321332 complex structure is also shown in Figure 132. The residual amino acids with 2.5A from PF 07321332 and the modified PF 07321332 are shown in Figure 133. The PF07321332 cyano group contacted N143, G143, C145, and E166. The cyano group's main binding residual amino acids seemed to be cysteine and asparagine. Those of the modified PF07321332 were N142, G143, C145, E166, and H172. These Figures indicate that the replacement from PF 07321332 to the modified PF 07321332 did not cause significant complex conformation changes and seemed very identical. The electron localization of key atoms was calculated using a PM5 program, and the results are demonstrated in Figure 134. The Interaction with the protein negatively shifted both the cyano and carboxy group's atomic partial charge. PF 07321332 was bound with ACE-2, but the modified PF 07321332 was repulsed; therefore, a complex of Delta S-RBD and modified PF 07321332 was prepared and analyzed whether the complex would be bound or should be repulsed with ACE-2.

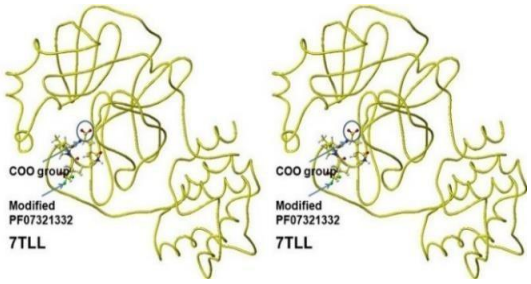

Figure 132. Conformation of PF 07321332 and modified from PF 07321332 trapped protein The cyano and carboxy groups are circled for their identification.

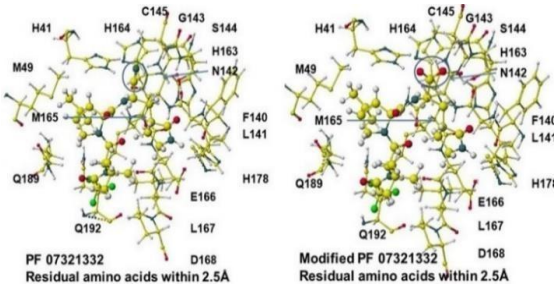

Figure 133. Amino acid residues within 2.5A PF 07321332 and modified PF 07321332 The cyano and carboxy groups are circled for their identification.

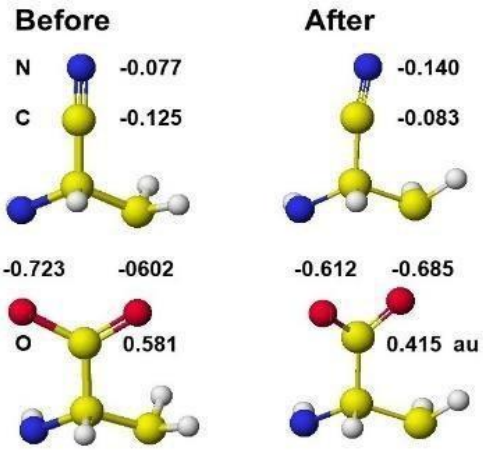

Figure 134. Atomic partial charge of key atoms before complex formation

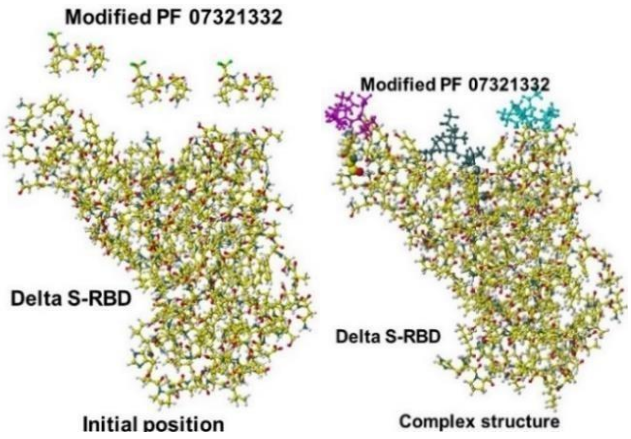

Figure 135. Delta S-RBD and modified PF 07321332 and after complex

The modified PF 0721332 was located above the ACE-2 binding site shown in Figure 135, and the optimized complex structure is also shown in Figure 135, where three modified PF 07321332 molecules were used to cover the binding site. The optimized complex of S-RBD and three modified PF 07321332 molecules faced an ACE-2 binding site, and these compounds were optimized. After optimization, the S-RBD complex with modified PF 07321332 disappeared from the screen due to the repulsion from ACE-2. The structure is not shown because of the long distance between these molecules. This result indicated that the modified PF 0721332 might work as a binding inhibitor for Delta S-RBD binding with ACE-2.

The same approach was performed for the Omicron BA2 variant. However, Omicron BA2 and the modified PF 0721332 complex were bound with ACE-2. The result indicated the modified PF 0721332 might not inhibit the binding. Citric acid inhibited the binding of the Omicron BA2 S-RBD and ACE-2. Figure 136 shows the initial positions of modified PF-07321332 and Omicron BA2-S-RBD, and Figure 136 also shows the bound conformation. Figure 137 shows the complex structure of modified PF-07321332 and ACE-2. For the detail of the Omicron BA2 structure, see Figure 124.

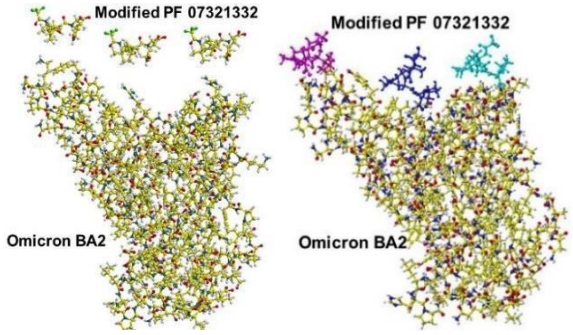

Figure 136. The initial position of Omicron BA2-S-RBD 07321332, and PF-07321332 and the complex structure

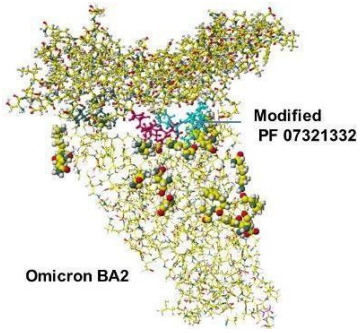

Figure 137. ACE-2, modified PF-Omicron BA2-S-RBD complex

There are two types of drugs. One is trapped by proteins and is not metabolized by the protein (enzyme). This type of compound is a suicide helper. Another type of compound involves DNA activities. Molnupiravir having a basic group is an effective drug for binding with the phosphate of DNA and RNA, and it does not inhibit the S-RBD and ACE-2 binding. Molnupiravir is a latter-type compound. Ideal drugs are not trapped by ACE-2 and keep ACE-2 enzyme activities. Cocktail drugs consisting of a mixture of the drug candidate and acidic compounds may help the feasibility of the proposed compounds.

Closing remark: The mutation of COVID-19 is too fast, following the analysis of the transmissibility and estimation of the multiplication are delayed. How to prevent the infection is an urgent subject. The above analysis suggests that a good inhibitor candidate is citric acid, synthesized from glucose as a normal metabolic process. Kids constantly produce citric acid and other citric acid cycle acids, then synthesize related amino acids, and other important compounds for growing. Aging reduces such activity; therefore, adults must eat food containing essential metabolites. This known metabolism may indicate that kids are less infected [156]. Children's self-protection against COVID-19 was reported and talked about the mysterious results, even though children do not have a particular compound, and the fundamental defense mechanisms should be the same as those of adults [157,158]. It may be the activity of ordinal metabolisms and mass production of various compounds for their growth. In contrast, the aged person does not produce a large quality of actual products. They may not have enough vital metabolites to win from Covid-19 infection if they do not eat balanced food. Food habitude may affect the mortality of meat-eating and vegetable-eating populations by comparison to their food habits. The USA's total death/ and infectibility/population ratio is approximately 14 and 10 times Japan's total death/ and infectibility/population ratio. American's relative concentration of citric acid-related metabolites [159] is lower than Japanese. The "Healthy eating" report presented the regional food habitude [160], suggesting transmissibility and mortality are very high in certain countries. Excess eating of dairy and animal protein seems to relate to the urgent problem. We have to analyze the evidence based on quantitative analytical chemistry continuously.

We need temporary help with vaccines; however, we must maintain our daily health by exercising and eating balanced food. We should avoid continuous vaccination to maintain our immune system as our normal condition against unpredictable viruses and bacteria. Continuous vaccination is like living in a greenhouse and eating supplements. People who used to live in such condition is vulnerable outside of the greenhouse. The unbalanced habitude seems clear evidence for Covid-19 transmissibility and mortality. Understanding fundamental chemistry should help individuals reconsider their lifestyles, including vaccination and drugs.

Conclusion

The fundamental study of ion-exchange group properties was achieved using bio-mimic ion-exchange groups. The ion-exchange groups contribute hydrogen bonding and ion-ion interactions with various molecules. Further study using reproducible molecular interaction measured using chromatography developed a new quantitative analysis method of molecular interactions. The quantitative analytical method was successfully applied to the

quantitative analysis of molecular interaction between a small molecule (substitute) and proteins (quantitative analysis of enzyme reactions). Furthermore, the method applied the quantitative analysis of protein-protein interaction (quantitative analysis of COVID-19 variant transmissibility). The fundamental binding mechanism is ion-ion Interaction. Hydrogen bonding also contributes to the binding of S-RBD with ACE-2.

The transmissibility was quantitatively analyzed as the strength of protein-protein Interaction. Acidic amino acids lined up at the ACE-2 binding site, and high transmissible mutant's S-RBD has mutation from acidic and neutral amino acids to basic amino acids. That is, ion-ion interaction enhanced the binding. Therefore, molecular interaction energy calculation between two amino acids supported the transmissibility. This calculation does not require a high-level computational chemical system. The direct calculation between mutant's S-RBD and ACE-2 accurate the molecular interaction energy difference due to the including steric hindrance of protein stereo structure. The key mutations are L452R, T478K, N440K, Q493R, and Q498R; the multi-mutations to basic amino acids further enhanced the transmissibility.

The binding inhibitor's structure can be designed from these results. The binding strength is based on the mutation to basic amino acids. Acidic amino acids were repulsed from ACE-2 lined-up acidic amino acids. That is, the binding can be inhibited by the compounds having carboxy groups. The binding analysis between the ACE-2 and 80 drug candidates supported that ionized carboxy compounds were repulsed from the ACE-2 binding site. A common inhibitor was citric acid. In addition, the capability of our killer cells has limitations to erase the invented viruses; therefore, the multiplication of viruses is required. The virus multiplication can be reduced by avoiding taking excess amounts of lysine and arginine used for their mutation. A modified oral drug seemed to inhibit the S-RBD binding with the ACE-2. Understanding the fundamental molecular interaction mechanisms can support designing new drug candidates.

Further calculations using full-size structures should improve the precision. Other parts of SARS-CoV-2 contribute to protein complex tightness. However, the above *in silico* analysis quickly estimates the mutant transmissibility and can search for inhibitors.

References

1. Brode, E.R. The determination on hydrogen-ion concentration by a spectrophotometric method and the absorption spectra of certain indicators, J. Am. Chem. Soc 46 (1924) 581-596.
2. I.M. Kolthoff, I.M. Indicator constants, J. Phys. Chem 34 (1929) 1466-1483.
3. Computing across the chemistry curriculum. http://chemed.chem.pitt.edu/ChemEd/ComputingacrosstheChemistryCurriculum.doc
4. Hanai, T. Quantitative evaluation of dissociation mechanisms in phenolphthalein and the related compounds, Journal of Computer Chemistry, Japan 15 (2016) 13-21.
5. Creekmore, T.W., Reilley, C.N. Nuclear magnetic resonance study of ion-exchange resins. Anal Chem 42 (1970) 570-575.
6. Gough, T.E, Sharma, H.D, Subramanian N. Proton magnetic resonance studies of ionic solvation in ion-exchange resins. Part 1. Sulfonated cation-exchange resins. Can. J. Chem 48 (1970) 917-923.
7. Funasaka, W, Hanai, T. Estimation of adsorption mechanisms using NMR and ESCA, Proceeding of Annual Autumn Symposium of Chubu Kagaku Kanren Kyokai (1974) IE04.
8. Hanai T, Hatano, H, Nimura, N, et al. Computational chemical analysis of retention on ion-exchange resin in normal-phase liquid chromatography, Hatano, H., Hanai, T. (Eds) International symposium on chromatography, Jan. 1995, Yokohama, World Sci. Singapore 6 (1995) 97-103.
9. Gur'yonova, E.N, Gol'dshtein, L.P, Romm, L.P. (eds) Donor-acceptor bond, Translated by Kondor, R.; Slutzkin, D. (1975), Halsted Press/John Wiley & Son, New York 366.
10. Guttmann, V. The donor-acceptor approach to molecular interactions, (1978), Prenum Press, New York 279.
11. Walton, H.F. Ion-exchange chromatography, Editor Heftman, E. Chromatography fundamentals and applications of chromatographic and electrophoretic methods, Elsevier, Amsterdam (1983) A225-A255.
12. Acikara, O.B. Ion-exchange chromatography, and its applications, Column chromatography, Chapter 2, Intechopen, London, UK (2013) 32-58.
13. Morgan, P.F, Hanna-Brown, M, Flanagan, R.J. Characterization of a microparticulate strong anion-

exchanger in the HPLC of acidic drugs, Biomed 20 (2006) 765-73.
14. Hanai, T. (ed) Quantitative in silico chromatography, Computational modeling of molecular interactions, RSC, Cambridge 19 (2014) 220-236.
15. Hanai, T. HPLC A Practical Guide, Editor Hanai, T. (ed) Royal Society of Chemistry, Cambridge, UK, (ISBN: 0-85404-515-5, 1999, 1-134. Society of Chemistry, Cambridge, UK 122 (1999) 1-134.
16. Yamauchi, S,, Hanai, T,, Suzuki, J, et al. Development of protamine-bonded phase for separation of saccharide in liquid chromatography J, Chromatogr A 737 (1996) 149-156.
17. Hanai, T., Shimada, K., Koyama, N., et al. Quantitative analysis of selective glycosylation of saccharides with aromatic amines. Carbohydrate Research 498 (2020) 108171
18. Kato, K,, Furukoshi, E,, Hennmi, M, et al. Hanai, T. Definition of HILIC system and quantitative analysis of retention mechanisms, Current Chromatography 5 (2018) 43-52.
19. Hanai, T., Polysiliconedioxide phase Fundamental Properties of Packing Materials for Liquid Chromatography, Separation 6 (2019) 1-20.
20. Laitinen, H.A,, Ewing, G.W., (eds). A History of Analytical Chemistry, The Division of Analytical Chemistry of the American Chemical Society (1977) 327-339.
21. Dickson, T.R. (ed). Introduction to Chemistry, 2000, John Wiley & Sons, New York, 20 (1999) 640.
22. Barker, P.G. (ed). Computers in Analytical Chemistry, 1983, Pergamon Press, Oxford 6 (2010) 472.
23. Gary L., Breneman O., Parker. J. (eds). Chemistry and Computing, 1989, Prentice-Hall, Englewood Cliffs, New Jersey (1980) 197.
24. Hanai T. (ed). HPLC A Practical Guide, Royal Society of Chemistry, Cambridge (1999) pp.134.
25. Hanai T. Basic properties of a molecular mechanics program and the generation of unknown stereo structures of proteins for quantitative analysis of enzyme reactions, in Priscilla Watkins (ed) Molecular mechanics and modeling, Nova Science Publishers, New York (2015) 25-48.
26. Krebs, H.A., Metabolism of amino acids III. Determination of amino acids, Biochem. J. 29 (1935) 1620-1644.
27. Konno, R,, Yasumura, Y., D-Amino-acid oxidase and its physiological function, Int. J. Biochem. 24 (1992) 519-524.
28. Malcolm, D,, Kjell, K. D-Amino acid oxidase II, Specificity, competitive inhibition and reaction sequence, Biochem. Biophys. Acta 96 (1965) 368-382.
29. Pilone, M.S. D-Amino acid oxidase: new findings. Cell. Mol. Life Sci 57 (2000) 1732-1747.
30. RSC Protein Data Bank. www.rcsb.org/pdb/
31. NP 001908, D-amino acid oxidase [Homo sapiens]. www.ncbi.nlm.nih.gov/entrez/query.fcgi?CMD
32. Hanai, T. Quantitative in silico analysis of molecular recognition and reactivity of D-amino acid oxidase. Internet Electronic Journal of Molecular Design5 (2006) 247-259.
33. Hanai T. Quantitative in silico analysis of enzyme reactions: comparison of D-amino acid oxidase and monoamine oxidase. American Biotechnology Laboratory 25 (2007) 12-13.
34. Hanai T. Quantitative in silico analysis of D-amino acid oxidase reactivity and inhibition, Current Bioactive Compounds 13 (2017) 312-317.
35. Nithya, S,, Shanmugarajam, T.S. D-Amino acid oxidase: A review. Asian J. Pharm. Clin. Res 9 (2016) 33-36.
36. Panthis, S,, Chung, H.J,, Jung, J, et al. Physiological importance of hydrogen sulfite: Emerging potent neuroprotector and neuromodulator. Oxid. Med. Cell. Longev 2016 (2016) 9049781.
37. Kimura, H. Signalino molecules: Hydrogen sulfide and polysulfide. Antioxid. Redox. Signal 22 (2016) 362-375.
38. Ohide, H,, Miyoshi, Y,, Maruyama, R, et al. D-Amino acid metabolism in mammals: biosynthesis, degradation and analytical aspects of the metabolic study. J. Chromatogr. B 879 (2011) 3162-3168.
39. Nishikawa, T. Analysis of free D-serine in mammals and its biological relevance. J. Chromatogr. B 879 (2011) 3169-3183.
40. Wolosker, H. NMDA receptor regulation by D-serine: new findings and perspectives. Mol. Neurobiol 36 (2007) 152-164.
41. Kakegawa, W,, Miyoshi, Y,, Hamase, K, et al. D-Serine regulates cerebellar LTD and motor coordination through δ2 glutamate receptors. Nature Neurosci 14 (2011) 603-611.
42. Di Fiore, M.M,, Santillo, A,, Baccari, G.C. Current knowledge of D-aspartate in glandular tissues, Amino Acids 46 (2014) 1805-1818.

43. Katane, M,, Homma, H. D-Aspartate an important bioactive substance in mammals: a review from an analytical and bioanalytical point of view. J. Chromatogr. B 879 (2011) 3108-3121.
44. Katane, M,, Homma, H. D-Aspartate oxidase: the sole catabolic enzyme acting on free D-aspartate in mammals. Chem. Biodivers 7 (2010) 1435-1449.
45. Mattevi A, Vanoni MA, Todone F, et al. Crystal structure of D-amino acid oxidase; a case of active site mirror-image convergent evolution with flavocytochrome b2. Proc. Natl. Acad. Sci. U.S.A 93 (1996) 7496-7501.
46. Mizutani, H,, Miyayama, I,, Hitotsu, K, et al. Three-dimensional structure of porcine kidney D-amino acid oxidase at 3.0Å resolution. J. Biochem. 120 (1996) 14-17.
47. Umhau, S,, Pollegioni, L,, Molla, G, et al. The X-ray structure of D-amino acid oxidase at very high resolution identifies the chemical mechanism of flavin-dependent substrate dehydrogenation. Proc. Natl. Acad. Sci. U.S.A 97 (2000) 12463-12468.
48. Kawazoe, T,, Tsuge, H,, Pilone, M.S, et al. Crystal structure of human D-amino acid oxidase: context-dependent variability of the backbone conformation of the VAAGL hydrophobic stretch-located at the si-face of the flavin ring. Protein Sci 15 (2006) 2708-2717.
49. Kawazoe, T,, Tsuge, H,, Imagawa, T, et al. Structural basis of D-DOPA oxidation by D-amino acid oxidase: Alternative pathway for dopamine biosynthesis, Biochem. Biophys. Res 355 (2007) 385-391.
50. Sacchi, S,, Lorenzi, G,, Molla, M.S, et al. Engineering the substrate specificity of D-amino acid oxidase. J. Biol. Chem 277 (2002) 510-516.
51. De Marche, W.J,, Johnston, G.A.R. The oxidation of glycine by D-amino acid oxidase in extracts of mammalian central nervous tissue. J. Neurochem 16 (1969) 355-361.
52. Katane, M,, Hanai, T,, Furuchi, T, et al. Hyperactive mutants of mouse D-aspartate oxidase: mutagenesis of the active site residue serine 308. Amino Acids 35 (2008) 75-82.
53. Katane, M,, Saitoh, Y,, Hanai, T, et al. Thiolactomycin inhibits D-aspartate oxidase: a novel approach to probing the active site environment, Biochim 92 (2010) 1371-1378.
54. Hanai, T,, Katane, M,, Homma, H. Quantitative in silico analysis of selective enzyme reaction of mammalian D-amino acid oxidase and acidic D-amino acid oxidase mutants, SDRP J. Comp. Chem. Mol. Model. (JCCMM) 2 (2018) 1-9.
55. Katane, M,, Kuwabara, H,, Nakayama, K, et al. Rat D-aspartate oxidase is more similar to the human enzyme than the mouse enzyme, BBA-Proteins and Proteomics 1866 (2018) 806-812.
56. Shore, J.D., Theorell, H., A Kinetic study of ternary complexes in the mechanism of action of liver alcohol dehydrogenase, Arch. Biochem. Biophys 116 (1966) 255-260.
57. Shore, J.D., Brooks, R.L. Kinetic evidence for a binary complex isomerization in the liver alcohol dehydrogenase reaction mechanism, Arch. Biochem. Biophys 147 (1971) 825-827.
58. Shore, J.D,, Gutfreund, H,, Brooks, R.L, et al. Proton equilibria and kinetics in the liver alcohol dehydrogenase reaction mechanism, Biochemistry 13 (1974) 4185-4190.
59. Shore, L.D., Halvorson, H.R,, Lucast, K.D. The role of conformational changes in the liver alcohol dehydrogenase reaction mechanism, FEBS-Symposium 49 (1977) 416-425.
60. Tanner, D.D,, Stein, A.R. On the mechanism of reduction by reduced nicotinamide adenine dinucleotide dependent alcohol dehydrogenase. A-Halo ketones as mechanistic probes, J. Org. Chem 53 (1988) 1642-1646.
61. Pocker, Y,, Page, J.D. Zinc-activated alcohols in ternary complexes of liver alcohol dehydrogenase, J. Biol. Chem 265 (1990) 22101-22108.
62. Rosell, A,, Valencia Pares, X,, Fita, I. et al. Ochoa W.F. Crystal structure of the vertebrate NADP(H)-dependent alcohol dehydrogenase (ADH8), J. Mol. Biol 330 (2003) 75-85.
63. Raj, S.B,, Ramaswamy, S,, Plapp, B.V. Yeast alcohol dehydrogenase structure and catalysis, Biochemistry 53 (2014) 5791-5803.
64. Valencia, E,, Larroy, C,, Ochoa, W.F, et al. Apo and Holo structure of NADP(H)-dependent cinnamyl alcohol dehydrogenase from Saccharomyces cerevisiae, J. Mol. Biol 341 (2004) 1049-1062.
65. Benach, J,, Winberg, J.O,, Svendsen, et al. Drosophila alcohol dehydrogenase: Acetate-enzyme interactions and novel insights into the effects of electrostatics on catalysis, J. Mol. Biol 345 (2005) 579-598.
66. Hanai, T, Quantitative in silico analysis of alcohol dehydrogenase reactivity, Journal of Drug Design and Research 2 (2014) 1-7.

67. Larroy, C,, Fernandez, R.M,, Gonzalez, E, et al. Characterization of the Saccharomyces cerevisiae YMR318C (ADH6) gene product as a broad specificity NADH-dependent alcohol dehydrogenase: relevance in aldehyde reduction, Biochem. J 361 (2002) 163-172.
68. Pilate, G,, Guiney, E,, Holt, K, et al. Field and pulping performances of transgenic trees with altered lignification, Nature Biotechnology 20 (2002) 607-612.
69. Williamson, J.D,, Stoop, J.M.H,, Massel, M.O, et al. Pharr DM Sequence analysis of a mannitol dehydrogenase cDNA from plants reveals a function for the pathogenesis-related protein ELI3, Proc. Natl. Acad. Sci. USA 92 (1995) 7148-7152.
70. Somssich, I.E,, Wernert, P,, Kiedroqwski, S, et al. Arabidopsis thaliana defense-related protein ELIS-3 is aromatic alcohol: NADP+ oxidoreductase, Proc. Natl. Acad. Sci. USA 93 (1996) 14199-14203.
71. Waltz, R,, Vahrenkamp, H. Functional modeling of alcoholdehydrogenase with pyrazoylborate-zinc complexes, Inorganic Chimica Acta 314 (2001) 58-62.
72. Zhang, Y.H,, Vahrenkamp, H. Zinc complexes of a macrocyclic N3O2 ligand for the functional modeling of alcoholdehydrogenase, Inorganic Chimica Acta 351 (2003) 201-206.
73. Uniprot (Q02972), www.ncbi.nlm.nih.gov/entrez/query.fcgi?CMD
74. Umhau, S,, Pollegioni, I,, Molla, G, et al. The x-ray structure of D-amino acid oxidase at very high resolution identifies the chemical mechanism of flavin-dependent substrate dehydrogenation, Proc. Natl. Acad. Sci. USA 97 (2000) 12463-12468.
75. Smith, G.G,, Sivakus, T. Mechanism of the racemization of amino acids. Kinetics of racemization of arylglycines, J. Org. Chem 48 (1983) 627-634.
76. Faraci, E.S,, Walsh, C.T. Racemization of alanine by the alanine racemases from Salmonella typhimurium and Bacillus stearothermophilus: Energetic reaction profiles, Biochemistry 27 (1988) 3267-3276.
77. Watanabe, A,, Yoshimura, T,, Mikami, B, et al. Reaction mechanism of alanine racemase from Bacillus stearothermophilus, J. Biol. Chem 277 (2002) 19166-19172.
78. Toney, M.D. Reaction specificity in pyridoxal phosphate enzyme, Ach. Biochem. Biophys 433 (2005) 279-287.
79. Major, D.T,, Nam, K,, Gao, J. Transition state stabilization and □-amino carbon acidity in alanine racemase, J. Am. Chem. Soc 128 (2006) 8114-8115.
80. Jeffrey, P,, Shaw, J.P,, Petsko, G.A, et al. Determination of the structure of alanine racemase from Bacillus stearothermophilus at 1.9 Å resolution, Biochemistry 36 (1997) 1329-1342.
81. Troiani, A,, Gasparrini, F,, Grandinetti, F, et al. Chiral ions in the gas phase. 1. Intramolecular racemization and isomerization of O-protonated (S)-trans-4-hexen-3-ol, J. Am. Chem. Soc 119 (1997) 4525-4524.
82. Sun, S,, Toney, M.D., Evidence for a two-base mechanism involving tyrosine265 from arginine219 mutants of alanine racemase, Biochemistry 38 (1999) 4058-4065.
83. Sharif, S,, Powell, D.R,, Schagen, D, et al. X-ray crystallographic structures of enamine and amine Schiff bases of pyridoxal and its 1:1 hydrogen-bonded complexes with benzoic acid derivatives: evidence for coupled inter- and intra-molecular proton transfer, Acta Cryst 62 (2006) 480-487.
84. Hanai, T, Quantitative in silico analysis of alanine racemase reactivity, in Priscilla Watkins (ed) Molecular mechanics and modeling, Nova Science Publishers, (2015) 49-71.
85. Hashimoto, A,, Nishikawa, T,, Hayashi, T, et al. The presence of free D-serine in rat brain. FWBS Let 296 (1992) 33-36.
86. Wolosker, H,, Sheth, K.N,, Takahashi, M, et al. Purification of serine racemase: biosynthesis of the neuromodulator D-serine. Proc. Natl. Acad. Sci. U S A 96 (1999) 721-725.
87. Smith, M.A,, Mach, V,, Ebneth, A, et al. The structure of mammalian serine racemase, Evidence for conformational changes upon inhibitor binding, J. Bio. Chem 285 (2010) 12873-12881.
88. Wang, W,, Barger, S.W. Roles of quaternary structure and cysteine residues in the activity of human serine racemase, BMC Biochem 12 (2011) 63.
89. Pollegioni, L,, Piubelli, L,, Molla, G, et al. D-amino acid oxidase-pLG72 interaction and D-serine modulation, Front. Mol. Biosci 5 (2018) 1-12.
90. Kondori, N.R,, Paul, P., Robbin, J.P, et al. Focus on the role of D-serine and D-amino acid oxidase in Amyotrophic Lateral Sclerosis/motor neuron disease (ALC), Front. Mol. Biosci 5 (2018) 1-7.
91. Nitoker, N,, Major, D.T. Understanding the reaction mechanisms and intermediate stabilization in mammalian serine racemase using multiscale quantum-classical simulation, Biochem 52 (2015) 516-527.

92. Hanai, T. Quantitative in silico analysis of alanine racemase reactivity, In Watkins, P. (ed.), Molecular Mechanics and Modeling. Nova Science: New York 3 (2015): 49-71.
93. Nelson, D.L,, Applegate, G.A,, Beio, M.L, et al. Human serine racemase structure/activity relationship studies provide mechanistic insight and point to position-84 as a hotspot for elimination function, J. Biol. Chem 10 (2017) 1-35.
94. Wu, H,, Qi, Y.B,, Kong, J, et al. A seven-coordinate manganese (II) complex formed with the tripodal tetradentate ligand tris(N-methylbenzimidazol-2-ylmethyl) amine, Z. Naturforsch 65 (2010) 1097-1100.
95. Metzler, D.E,, Snell, E.E. Deamination of serine: 1. Catalytic deamination of serine and cysteine by pyridoxal and metal salts, J. Biol. Chem 198 (1952) 353-361.
96. Gorgannezhad, L,, Dehghan, G,, Ebrahimipour, S.Y, et al. Complex of manganese (II) with curcumin: Spectroscopic characterization, DFT study, model-based analysis and antiradical activity, J. Mol. Struc. 1109 (2016) 139-145.
97. Islam, K. Manganese complex of ethylenediaminetetraacetic acid (EDTA)-benzothiazole aniline (BTA) conjugate as a potential liver-targeting MRI contrast agent, J. Med. Chem 60 (2017) 2993-3001.
98. Gohara, D.W,, Cera, E.D. Molecular mechanisms of enzyme activation by monovalent cations, J. Biol. Chem 291 (2016) 20840-20848.
99. Hanai. T, Quantitative in silico analysis of mammalian serine racemase activity, Int. J. Chem. Math. Phy. (IJCMP) 2 (2018) 53-58.
100. Katsnelson, A. What do we know about the novel Coronavirus's 29 proteins? C&EN (2020)
101. European Centre for Disease and Control, SARS-CoV-2 variants of concern as of June 3 (2021).
102. Lan, J,, Ge, J,, Yu, J, et al. Structure of the SARS-CoV-2 spile receptor-binding domain bound to the ACE2 receptor, Nature 581 (2000) 215-220,
103. Scudellari, M. How the coronavirus infects our cells, Nature 595 (2021) 640-644,
104. Ortega, J.T., Serrano, M.L, Pujol, F.H, et al. Role of changes in SARS-CoV-2 spike protein in the Interaction with the human ACE2 receptor: an in-silico analysis, EXCLI Journal 19 (2020) 410-417.
105. Haseltine, W.A. Birth of the omicron family: BA.1, BA.2, BA.3. each as different as alpha is from Delta. Coronavirus 26 (2022).
106. Haseltine, W.A. Whither the omicron family: BA.a, BA.1.1, BA.2, BA.2.H78Y, BA.3? Coronavirus 23 2022.
107. Chen, J,, Wang, R,, Wang, M, et al. Mutations strengthened SARS-CoV-2 infectivity, J. Mol Bio 432 (2020) 5212-5226.
108. Hanai, T. SARS-CoV-2 transmissibility and the protein structures, HYAKUMANBEN TUSHIN,181, (July 2021) pp. 4-12, (in Japanese), & Hanai, T. Covid-19 transmissibility and food habitude, HYAKUMANBEN TUSHIN 182 (2021): 5-7.Hanai T. Quantitative analysis of SARS-CoV-2 variants transmissibility, & S-RBD and ACE-2 docking inhibitors in: Hanai T. (ed.) Quantitative in silico analytical chemistry (2021) 153-159.
109. Zhu, X,, Mannar, D,, Srivastava, S.S, et al. Cryo-electron microscopy structures of the N501Y SARA-CoV-2 spike protein in complex with ACE2 and 2 potent neutralizing antibodies, PloS Biol 19 (2021) e3001237.
110. UniProtKB-Q9BYF1(ACE2- HUMAN) 4a ACE angiotensin-converting enzyme 2 [Homo sapiens (human)], Gene 59272 (2021).
111. Hanai, T. Introduction of silico chromatography J. Chromatogr. Sep. Tech 7 (2016) 1-8.
112. Pascarella, S,, Ciccozzi, M,, Bianchi, M, et al. The electrostatic potential of the omicron variant spike is higher than in delta and delta-plus variants: a hint to higher trensmissibility? J. Med. Virology 94 (2021) 1277-1280,
113. Rath, S.L., Padhi, A.K., Mandal, N. Scanning the RBD-ACE2 molecular interactions in omicron variant,Biom. Biophys. Res. Commun 592 (2022) 18-23.
114. Mandal, N,, Padhi, A.K,, Rath, S.L. Molecular insights into the differential dynamics of SARS-CoV-2 variants of concern, BioRxiv 2021.
115. Goher, S.S,, Ali, F,, Amin, M. The Delta variant mutations in the receptor-binding domain of SARS-CoV-2 show enhanced electrostatic interactions with the ACE2, Med. Drug Discov13 (2022) 100114.
116. Hanai, T. Quantitative in silico analysis of mammalian serine racemase activity, J. Chem. Math. Phy. (IJCMP) 2 (2018) 53-58.
117. Koley, T,, Kumar, M,, Goswami, A, et al. Biophys. Res. Commun 592 (2021) 51-53.

118. Majumdar, S,, Sarkar, R. Mutational and phylogenetic analyses of the two lineages of the Omicron variant, Med. Virology, Dec 29 (2021).
119. Pierros, V,, Kontopodis, E,, Stravopodis, D.J, et al. GT Prediction of SARS-SoV-2 omicron variant immunogenicity, immune escape and pathogenicity, through analysis of spiked protein-specific core unique peptides, MedRxiv preprint 29 (2021) 10.
120. Kumar, S,, Thambiraja, T.S,, Kanruppanan, K, et al. Omicron and delta variant fo SARS-CoV-2: A comparative computational study of spike protein, J. Med. Virology 94 (2021) 1641-1649.
121. Kumar, S,, Thambiraja, T.S,, Kanruppanan, K, et al. Omicron and Delta variant of SARS-CoV-2: A comparative computational study of spike protein, BioRxiv preprint 3 (2021).
122. Han, P,, Li, L,, Liu, S, et al. Receptor binding and complex structures of human ACE2 to spike RBD from omicron and delta SARS-CoV-2, Cell 185 (2022) 630-640.
123. Reardon, S. How well can Omicron evade immunity from covid vaccines? News 2 (2022).
124. Bose, P. Similarities and dissimilarities in immune responses and metabolism in SARS-CoV-2 and HIV-1 infections, 2022
125. Rath, S.L., Padhi, A.K., Mandal, N. Scanning the RBD-ACE2 molecular interactions in Omicron variant, Biochem. Biophys. Res. Commun 592 (2002) 18-23.
126. Ledford, H. Nature, 2022. 601, 307- & Nature 590 (2021) 374-375
127. Swargiary, A,, Mahmud, S,, Saleh, A. Screening of phytochemicals as a potent inhibitor of 3-chymotrypsin and papain-like proteases of SARS-CoV-2: an in-silico approach to combat Covid-19, J. Biomol. Struc.Dynamics, (2020) 1-15.
128. El-Hoshoudy, A.N. Investigating the potential antiviral activity drugs against SARS-CoV-2 by molecular docking simulation, L. Mol. Liq 318 (2020) 113968.
129. Dong, J,, Zost, S.J,, Greaney, A.J. et al. Genetic and structural basis for SARS-CoV-2 variant neutralization by a two-antibody cocktail, Nature Microbiology Letter 6 (2021) 1233-1244.
130. Saleh, M,, Gabriels, J,, Chang, D, et al. Effect of chloroquine, hydroxychloroquine, and Azithromycin on the corrected Q.T. interval in patients with SARS-CoV-2 infection, Circ. Arhythm. Electrophysiol 13 (2020) 496-504.
131. Boopathi, S,, Poma, A.B,, Kolandaivel, P. Novel 2019 coronavirus structure, mechanism of action, antiviral drug promises and rule out against its treatment, J. Biomol. Struc. Dyn (2020) 1-10.
132. Basha, S.H. Coronavirus drugs – a brief overview of past, present and future, J. PeerScoentist 2 (2020) e1000013.
133. Shah, M,, Woo, H.G. Omicron A heavily mutated SARS-CoV-2 variant exhibits stronger binding to ACE2 and potently escapes approved COVID-19 therapeutic antibodies, BioTxiv 2021.
134. Assadiasl, S,, Fatanhi, Y,, Moshamovahed, B, et al. Baricitinib: From rheumatoid arthritis to Covid-19, J. Clin. Pharmacol 12 (2021)1-17.
135. Oristrell, J,, Oliva, J.C,, Subirana, I, et al. Association of calcitriol supplementation with reduced Covid-19 mortality in patients with chronic kidney disease: a population-based study (2021) 1-17.
136. Boerner, L.K. Rethinking the role of blood pressure drugs in Covid-19, Once thought to boot levels of ACE2, the novel coronavirus's doorway into human cells, these widely used medicines are now contenders to treat the disease, C&EN 25 (2020) 28-33.
137. Indu, P,, Rameshkumar, M.R,, Arunagirinathan, N, et al, and Etravirine against main protease and RNA-dependent R.N.A. polymerase of SARS-CoV-2: A molecular docking and drug repurposing approach, J. Inf. Pub. Health 13 (2020) 1856-186.
138. Wu, C-R,, Yin, W.-C,, Jiang, Y, et al. Structure genomics of SARS-CoV-2 and its omicron variant: drug design templates for Dovid-19, Acta Pharm. Sinica 2022.
139. Douangamath, A,, Fearon, D,, Gehrtz P, et al. Crystallographic and electrophilic fragment screening of the SARS-Cov-2 main protease, Nature Communications (2020) 1-11.
140. Prajapati, J,, Patel, R,, Rao, P, et al. Perceiving SARS-CoV2 Mpro and Plpro dual inhibitors from pool of recognized antiviral compounds of endophytic microbes: an in-silico simulation study, Res. Square (2021) 1-47.
141. Jimenez-Avalos, G,, VargasoRuiz, A.P, Delgado-Pease, et al. 1115452 (2021) 1-18.
142. Bryant, A,, Lawrie, T.A,, Dowswell, T, et al. Ivermectin for prevention and treatment of Covid-19 infection: A systematic review. meta-analysis, and trial sequential analysis to inform clinical guidelines, Am. J. Ther 28 (2021) 434-460.

143. Cubuk, H,, Ozbil, M. Comparison of clinically approved molecules on SARS-CoV-2 drug target proteins: a molecular docking study, Turk. J. Chem 45 (2021) 35-41.
144. Wang, Z,, Yang, L. Turning the tide natural products and natural-product-inspired chemicals as potential counters to SARS-Cov-2 infection, Front. in Pharmacol 11 (2020) 1-12.
145. Watashi, K,, Mefloquine, a potent anti-severe acute respiratory syndrome-related coronavirus 2 (SARS-CoV-2) drug as an entry inhibitor in vitro, Frontiers in Microbiology, 2021
146. VA(http://www.va.gov/) > Health Care (http://www.va.gov/health) ? Public Health (/index.asp) > Military Exposures (/PUBLICHEALTH/exposures/indec.asp) > Mefloquine (Lariam@)
147. Satyanarayana, M. Two Covid-19 antiviral pills advance to late-stage trials, C&EN 13 (2021).
148. Yang, J,, Zhang, Z,, Yang, F, et al. Computational design and modeling of nanobodies toward SARS-C0V-2 receptor binding domain, Chem Biol. Drug Design 98 (2021) 1-18.
149. Manzanares-Meza, L.D,, Medina-Contreras, O. SARS-Cov-2 and influenza: a comparative overview and treatment implications, Bol. Med. Hosp. Infant Mex 77 (2020) 262-273.
150. Hall, Jr. D.C,, Ji, H-F. A search for medications to treat COVID-9 via in silico molecular docking models of the SARS-CoV-2 spike glycoprotein and 3CL protease, Travel med. Inf. Disease 35 (2020) 101646.
151. Qiao, Z,, Zhang, H,, Ji, H.F, et al. Computational view toward the inhibition of SARS-CoV-2 spike glycoprotein and the 3CL protease, Communication 8 (2020) 53-61.
152. Mourani, J. Sotrovimab monoclonal antibody treatment effective at reducing severe disease from Omicron Covid-19 variant, 2022.
153. Peplow, M. AI finds alternative routes to CONID-19 drug candidates, C&E News 10 (2020) 9.
154. Darazam, I.A,, Shokouhi, S,, Mardanai, et al. Umifenovir in hospitalized moderate to severe Covid-19 patients; A randomized Chlinical trial, Int. Immunophaarmacol (2021)107969.
155. RCSB Protein Data Bank, 7TLL.
156. Cheriyedath, S. Understanding immune responses to Sars-Cov-2 infections in childrenUnderstanding-immune-responses-to-SARS-CoV-2-infections-inchildren.aspx
157. Mallapaty, S. Kids and Covid: Why young immune systems are still on top, Nature 597 (2021) 166-168.
158. Mallapaty, S. Kids show mysteriously low levels of Covid antibodies, Nature, News 2022.
159. Breire, J.J, Favier J. Gimenez-Roqueple, A-P. Rustin, P. Tricarboxylic acid cycle dysfunction as a cause of human diseases and tumor formation, Am. J. Physiol. Cell Physiol 291 (2006) C1114-C1120.
160. Smith, K. Healthy eating, Nature News et al. Hirvonen, C.K. et al. Lancet Glob. Health Lancet 393 (2019) 447-492.